Three-Dimensional Finite Element Analysis of Impact Damage and Erosion of Metallic Targets

Thesis by

Jean-François R. Molinari

Mechanical Engineer, Université de Technologie de Compiègne,

France, 1997

MSc Aeronautics, California Institute of Technology, USA, 1997

In Partial Fulfillment of the Requirements

for the Degree of

Doctor of Philosophy

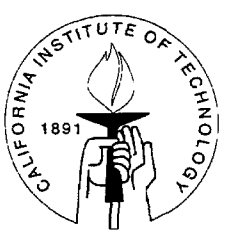

California Institute of Technology

Pasadena, California

2001

(Submitted September 7, 2000)

Acknowledgements

My greatest acknowledgements and admiration go to my advisor, Professor Michael Ortiz. As a unique person of great insight, he has provided me with comments and advice that were always valuable. He showed patience and constant enthusiasm during the ups and downs of my Ph.D.; Michael gave me high standards, and I wish to follow his model. Also, I am indebted to Professor Guruswaminaidu Ravichandran. I am grateful for his willingness to give me advice and answer the many questions I had. My admiration and thanks also go to Professor Ares J. Rosakis. He gave me precious advice, and his love for teaching is apparent and contagious. I want to thank Professor Yizhao Thomas Hou and Professor James L. Beck for reviewing my thesis. I am grateful for the financial support provided by the US Army Research Office under grant DAAH04-96-1-0056, and by the US Department of Energy through Caltech's Asci/ASAP Center for the Simulation of the Dynamic Behavior of Materials.

The Computational Mechanics laboratory in which I worked is a place where cooperation and assistance are promoted. I would like to thank all my colleagues. I am deeply indebted and grateful to my friend Dr. Eduardo Repetto who was always there for me, even during my worst moments. Dr. Raul Radovitzky was also a very helpful friend, and I am grateful for his support. I wish to thank as well Chengxiang Yu, my everyday colleague, for all the collaborations we had. I also acknowledge Pururav Thoutireddy and Olivier Nguyen who are just one year below me in the program. They are great to work with.

Finally, I would have never achieved anything without the unconditional support of my parents and my wife, Sandra, with whom I am going through life.

My love and gratitude go to my wife Sandra and my parents for their constant support.

Abstract

This dissertation is concerned with the development of a robust three-dimensional finite-element framework for the simulation of complex problems in mechanics and physics of solids. This approach is intended to shine light on impact and erosion mechanisms among other multiscale, multiphysics problems. The components of the computational framework are a contact algorithm including friction, wear, finite deformation plasticity, heat generation, heat transfer, and adaptive meshing coupled with error estimation. The adaptive meshing is a key development that enhances the efficiency and robustness of the method. We demonstrate the ability of the methodology to simulate diverse problems such as shear banding, impact, and wear.

Contents

List of Figures

List of Tables

Chapter 1 Introduction

This thesis is concerned with the development of a robust three-dimensional finite-element framework for the simulation of impact and erosion of metallic targets. The strategy adopted was to systematically validate the obtained numerical results with experimental data. Once verified, the finite-element methodology was used to determine the key physical mechanisms in impact and erosion phenomena.

Impact and surface-erosion mechanisms are of interest over a wide range of application areas. The most obvious domain of application is the military, where there is a need to understand the limiting factors of ballistic penetration. For example, one could try to reduce the development of instabilities such as shear bands in projectile materials. As shear bands are preferred sites of material failure, reducing or delaying them will reduce the fragmentation of the projectile and therefore increase its kinetic energy at impact. Other research efforts aim at designing better weapons. As an example, shaped-charge technology has been shown to be widely successful. A shaped charge is an ogive where a hollow cavity is left in front of a conical metal liner. Upon detonation the metal liner will flow plastically to form a high-velocity jet. This approach similarly has the consequence of producing a higher kinetic energy at impact than simple brute force designs. Any increase in kinetic energy will produce deeper cavities in the target.

When concerned with defense, there is also the inverse yet equally compelling need to understand impact and erosion mechanics in order to minimize the damage to armors. A strategy that is commonly chosen is to make use of layered composite materials. For instance, a graphite layer is sometimes introduced within an armor to deflect a projectile from its intended trajectory.

Understanding impact and erosion mechanics is also of great interest in civilian applications. A few examples that are being investigated are micro-meteorite damage to spacecraft structures, design of lightweight body armors, generation of cavities for

mining and gas exploration, the safety of nuclear-reactor containment vessels, erosion by abrasive particles in dusty environments, damage of car structures due to impact of gravel, and erosion as a method of cleaning and shaping engineering components.

An excellent overview of impact dynamics and erosion mechanisms, including experimental, numerical, and analytical models, is given by Zukas in his book on high-velocity impact dynamics [113]. Numerous excellent reviews can be found in the published literature. Johnson *et al.* [52] give an overview of high-velocity oblique impact and ricochet of long rod projectiles. A complete survey of the mechanics of penetration of projectiles into targets is given by Backman and Goldsmith [7]. Brown [11] discusses the development of target/missile formulas together with experimental programs and numerical methods in the context of energy release-rate protection for pressurized systems. He divides the numerical research efforts into two categories: the finite-difference method, which enjoyed a long history of success, and the finite-element method, which proves increasingly advantageous for its ability to handle complex geometries. Spatial discretization can be carried out in Eulerian or Lagrangian frameworks. In the Lagrangian approach, a grid is embedded in the material and distorts together with it. In the Eulerian scheme, the grid is fixed in space and mass flows through it. In the present work, we adopt a Lagrangian framework since as the grid deforms following the material, time histories for each material point are trivially obtained. Another advantage is that the material interfaces are easy to track.

Despite a large set of numerical techniques and the recent advances in hardware and software, most of the work in the area of impact dynamics is still experimental. Hutchings [49] impacted steel plates with steel spherical projectiles. Magness [65] commented on penetration efficiency of high-density materials in ballistic penetration experiments. He described the mushrooming upon impact of the penetrator tip as a limiting factor for penetration, since more volume of armor has to be displaced as the volume of the projectile increases. Roisman *et al.* [93] presented experimental results on the oblique penetration of a rigid projectile into a thick plastic target. Forrestal [31] carried out experiments on penetration of metallic targets and discussed the deflection

angles of the projectile. Eichelberger *et al.* [28] carried out a series of plate-impact experiments and commented on the effects of meteoroid impact on space vehicles.

Since impact-dynamics problems define very complex multiphysics systems, it is often difficult to track experimentally the influence of an isolated parameter. The high cost of experiments is also an impediment to extensive experimental research. However, the keen interest shown by both military and commercial research laboratories to understand the physics of impact and erosion calls for developing reliable numerical codes which are validated by experiments.

To successfully carry out impact dynamics simulations, we will first be concerned with developing a general framework for adaptive mesh refinement and coarsening in three-dimensional finite-deformation dynamic-elasto-plastic problems. Impact problems are amenable to a fully Lagrangian finite-element treatment provided that the deformation-induced distortion, which inevitably accompanies unconstrained plastic flows, is eliminated by continuous remeshing (e.g., [76, 69, 14, 15, 81]). In addition, the solutions of interest often develop fine structure due to shock formation, microstructural evolution, singularities (crack front), material instabilities, and other physical phenomena. Under these conditions, mesh adaption provides an effective tool for explicitly resolving multiple length scales in the solution. When combined with error estimation, mesh adaption additionally provides a means of minimizing the solution error, or, equivalently, of maximizing its accuracy, for a given computational cost.

We begin in Chapter 2 by outlining a variational formulation of the incremental problem of finite-deformation dynamic elasto-plasticity (see, [82, 79]) which provides a mathematical basis for *a posteriori* error estimation and mesh adaption. The error indicators which result are purely local, i.e., can be computed element by element, and rigorously *a posteriori*, i.e., follow directly from the finite-element solution [82]. This is in contrast to other error indicators whose evaluation requires smoothing steps involving patches of elements (e.g., [26, 25, 112, 21]). Based on these error estimates, the optimal mesh size distribution may be determined as the solution proceeds. We include in Chapter 2 the description of the contact algorithm, as well as discuss the

issues of heat transfer and heat generation, both of which are key components in our dynamic calculations.

One component of our finite-element methodology is left for detailed discussion in Chapter 3: the three-dimensional adaptive meshing capability. This innovative development consists of successive subdivision and edge-collapse operations. The particular mesh refinement strategy which we adopt is an extension of Rivara's two-dimensional longest-edge propagation path (LEPP) bisection algorithm [91, 89, 90]. One appealing property of this method is that it guarantees that the aspect ratio of the elements remains above a certain lower bound regardless of the number of applications of the algorithm. Other desirable attributes are its low cost and simplicity, and its guaranteed termination after a finite, typically small, number of element subdivisions. This is in contrast to other three-dimensional meshing techniques, such as constrained-Delaunay (see, for instance, [2]) and the advancing front method, which sometimes fail to terminate or produce ill-conditioned elements. In addition, local remeshing algorithms such as subdivision tend to minimize the so-called projection errors incurred when the state variables are transferred to the new mesh. In this regard, it should be noted the LEPP algorithm is strictly local, as all the nodes that are added are introduced in pre-existing elements. Numerical diffusion is particularly critical in problems of strain localization (such as the ones that will be discussed in Chapter 4), in which excessive numerical diffusion may inhibit or completely suppress the shear bands. Our strategy for mesh coarsening, or unrefinement, is based on the elimination of elements by edge collapse. This technique has been discussed extensively in the computer-graphics literature (see, [96, 45, 55, 57]). However, the applications therein are for the most part confined to the treatment of surfaces. Extensions to three dimensions and applications to finite-element analysis have not received nearly as much attention. In addition to coarsening, edge collapse may be used for eliminating from the mesh poor-quality elements, such as slivers. In this guise, edge collapse provides an effective means of controlling the quality of the evolving mesh.

The remainder of the thesis is concerned with applications of the proposed computational methodology. Chapter 4 covers the application of adiabatic shear band-

ing and serves to validate the general framework for adaptive meshing in the finite-deformation dynamic-plasticity range. Shear banding furnishes a prime example of the class of problems to which the framework outlined in the foregoing is intended to apply. The presented calculations are motivated by the cylinder implosion tests of Nesterenko *et al.* [75]. In these tests, a metallic hollow cylinder is subjected to explosive loading by the detonation of a charge surrounding the cylinder. The deformation field of the collapsing cylinder involves two families of spiraling shear bands [75]. Our calculations are designed so as to roughly replicate the nominal conditions experienced by an individual shear band. The material considered is tantalum.

Chapter 5 covers a finite-element analysis of impact erosion. We validate our numerical results with Hutchings's experiments [49] of hard-steel spherical projectiles impacting steel plates at a wide range of impact velocities and angles. We comment on the shape and dimensions of the impact area on the plates. More than purely a validation of a method, the obtained numerical results shine light on the necessity to carefully account for friction and the plastic behavior of the projectile in the calculations.

Finally, in Chapter 6, we conclude the thesis by showing how the contact algorithm can be coupled to an erosion law. For that purpose, we introduced the Archard law of wear to study the dry sliding wear regimes between a brass/steel metallic pair. We compare our results to the experiments of Lancaster [56]. It is shown that the selected method is successful in capturing the transition between severe and mild wear at a given sliding velocity. All three different applications — shear banding, plate impact, wear — demonstrate that our method is successful in capturing fine features of the solution. The published experimental data surveyed also constitute a sound validation test of our three-dimensional finite-element numerical solutions.

Chapter 2 Finite-element methodology

2.1 Introduction

This chapter covers the main mechanical components of the finite element methodology. Within the context of the Lagrangian framework we begin in Section 2.2 by expressing in variational form the problem of an elastic-plastic solid undergoing dynamic large deformations. The aspects of field and constitutive equations, time discretization and a minimum principle for the incremental problem are covered. Section 2.3 provides a suitable framework for error estimation and mesh adaption. Section 2.4 covers heat transfer and the main sources of heat. Finally, Section 2.5 describes a robust and efficient contact algorithm. The last component of the methodology, mesh adaption, is left apart; it is the subject of Chapter 3. Throughout the calculations, we are using ten-node quadratic tetrahedral elements.

2.2 Variational formulation of the incremental problem

We begin by expressing the problem of an elastic-plastic solid undergoing dynamic large deformations in variational. More precisely, the aim is to characterize the motion of the solid as the solution to a sequence of *minimization* problems. As in the work of Dolzmann and Friesecke [33], Kinderlehrer and Otto [53], Ortiz and Repetto [78], and Kane *et al.* [54], the variational principles envisioned here are based on time-discretization and pertain to the time-discretized incremental problem. Another critical step in the derivation of the incremental minimum principle is the formulation of variational constitutive updates for elastic-plastic solids [82, 79]. The combination of time discretization and variational constitutive updates delivers a minimum prin-

ciple which characterizes the solutions of the incremental problem. This minimum principle in turn furnishes a powerful mathematical basis for error estimation and mesh adaption.

2.2.1 Field and constitutive equations

In this thesis we shall be concerned with the motions of elastic-plastic materials. We select the initial configuration $B_0 \subset \mathbb{R}^d$ of the body at time t_0 as the reference configuration; see Figure 2.1.

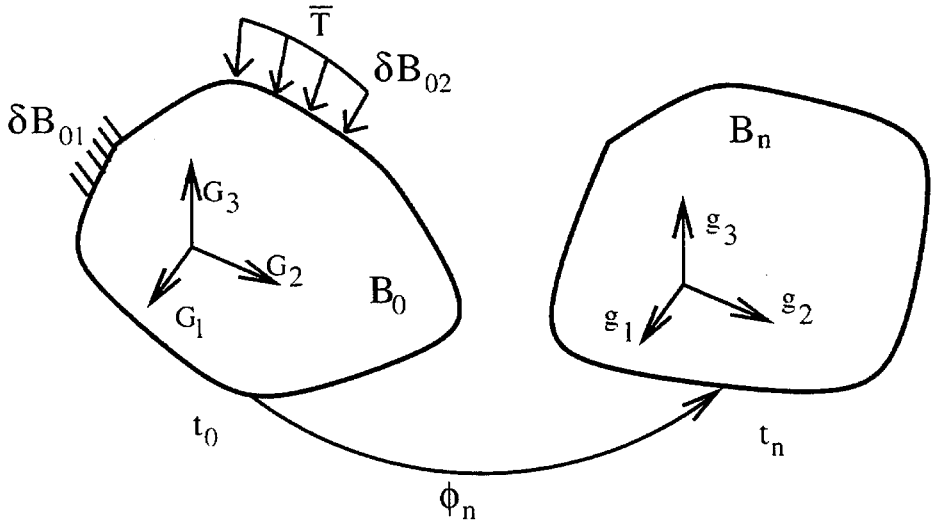

Figure 2.1: Initial configuration with boundary conditions

The motion of the body is described by a time-dependent deformation mapping $\boldsymbol{\varphi}$: $B_0 \times [t_0, \infty) \to \mathbb{R}^d$. The local deformation of infinitesimal material neighborhoods is described by the deformation gradient

$$\boldsymbol{F} = \nabla_0 \boldsymbol{\varphi}, \qquad \text{in } B_0 \tag{2.1}$$

where, here and subsequently, ∇_0 denotes the material gradient over B_0. The motions of the body obey the equation of motion (*cf.* [68])

$$\nabla_0 \cdot \boldsymbol{P} + \rho_0 \boldsymbol{B} = \rho_0 \ddot{\boldsymbol{\varphi}}, \qquad \text{in } B_0 \tag{2.2}$$

where ρ_0 is the mass density over B_0, $\boldsymbol{B}$ are the body forces per unit mass, $\boldsymbol{P}$ is the first Piola-Kirchhoff stress tensor, and $\ddot{\boldsymbol{\varphi}}$ is the material acceleration field. For purposes of formulating boundary conditions, we partition the boundary ∂B_0 of B_0 into a Dirichlet or displacement boundary ∂B_{01} and a Neumann or traction boundary ∂B_{02}. The displacement boundary conditions then take the form:

$$\boldsymbol{\varphi} = \bar{\boldsymbol{\varphi}}, \qquad \text{on } \partial B_{01} \tag{2.3}$$

where $\bar{\boldsymbol{\varphi}}(\boldsymbol{X}, t)$ is the prescribed deformation mapping on ∂B_{01}. The traction boundary conditions then take the form:

$$\boldsymbol{P} \cdot \boldsymbol{N} = \bar{\boldsymbol{T}}, \qquad \text{on } \partial B_{02} \tag{2.4}$$

where $\boldsymbol{N}$ is the unit outward normal to ∂B_{02} and $\bar{\boldsymbol{T}}(\boldsymbol{X}, t)$ are the prescribed tractions applied to ∂B_{02}. In addition, the formulation of the problem requires the initial deformation mapping and material velocity field, $\boldsymbol{\varphi}$ and $\dot{\boldsymbol{\varphi}}$, respectively, to be supplied.

We assume a multiplicative decomposition of the deformation gradient $\boldsymbol{F}$ of the form (see, [58, 101, 4, 40, 41, 66, 87])

$$\boldsymbol{F} = \boldsymbol{F}^e \boldsymbol{F}^p \tag{2.5}$$

into an elastic part $\boldsymbol{F}^e$ and a plastic part $\boldsymbol{F}^p$. We further assume that the elasticity and the specific heat of the material are structure insensitive, i.e., independent of the internal processes. This leads to a free energy of the form [79]:

$$A(\boldsymbol{F}, \boldsymbol{F}^p, T, \mathbf{q}) = W^e(\boldsymbol{F}^e, T) + W^p(T, \mathbf{q}, \boldsymbol{F}^p) \tag{2.6}$$

where W^e is the elastic strain-energy density, W^p is the stored energy of cold work, T is absolute temperature, and $\mathbf{q}$ is some appropriate set of internal variables (see, e.g., [63, 64]). If, for simplicity, we restrict attention to isotropic hardening, then ε^p may conveniently be identified as the sole internal variable of the material, and the free energy simplifies to:

$$A(\boldsymbol{F}, \boldsymbol{F}^p, T, \varepsilon^p) = W^e(\boldsymbol{C}^e, T) + W^p(T, \varepsilon^p) \tag{2.7}$$

The flow rule which governs the evolution of $\boldsymbol{F}^p$ is assumed to be of the form:

$$\dot{\boldsymbol{F}}^p \boldsymbol{F}^{p-1} = \dot{\varepsilon}^p \boldsymbol{M} \tag{2.8}$$

where ε^p is the effective plastic strain and $\boldsymbol{M}$ is a tensor which defines the direction of plastic flow. Within the present variational framework [79], the defining characteristic of J_2-flow theory of plasticity is that $\boldsymbol{M}$ can be any symmetric tensor satisfying the kinematic constraints:

$$\operatorname{tr}(\boldsymbol{M}) = 0 \tag{2.9}$$

$$\frac{2}{3}\boldsymbol{M} \cdot \boldsymbol{M} = 1 \tag{2.10}$$

Thus, the direction of plastic flow must be volume preserving, but it is otherwise unrestricted by the kinematics of plastic deformation.

Finally, we require a suitable kinetic equation, or rate-sensitivity law, governing the evolution of the effective plastic strain ε^p. For the constitutive relations and updates to possess a variational structure, the kinetic relations must have a certain potential form [79]. In the present context of isotropic plasticity, we begin by introducing the thermodynamic driving force conjugate to ε^p as

$$Y = -\frac{\partial A}{\partial \varepsilon^p} \tag{2.11}$$

Using (2.7), this relation evaluates to:

$$Y = \sigma - \sigma_0 \tag{2.12}$$

where

$$\sigma = -\frac{\partial W^e}{\partial \varepsilon^p} \tag{2.13}$$

is the effective Mises stress, and

$$\sigma_0 = \frac{\partial W^p}{\partial \varepsilon^p} \tag{2.14}$$

is the quasistatic flow stress. It follows from (2.12) that the driving force Y coincides with the effective overstress. We now postulate the existence of a $\psi(Y,T)$ which acts as a kinetic potential for the rate-sensitivity law, i.e., such that

$$\dot{\varepsilon}^p = \frac{\partial \psi}{\partial Y}(Y,T) \tag{2.15}$$

For purposes of defining variational constitutive updates, we additionally introduce the dual kinetic potential

$$\psi^*(\dot{\varepsilon}^p,T) = \min_Y \{\psi(Y,T), -Y\dot{\varepsilon}^p\} \tag{2.16}$$

The dual kinetic potential has the property that

$$Y = \frac{\partial \psi^*}{\partial \dot{\varepsilon}^p}(\dot{\varepsilon}^p,T) \tag{2.17}$$

i.e., it furnishes a potential for the inverse rate-sensitivity law.

The preceding formulation, and the corresponding constitutive updates discussed subsequently, may be extended to account for viscosity [82], but this extension will not be pursued here for simplicity.

2.2.2 Time discretization

Next we envision a process of incremental deformation and seek to determine the solution at discrete times $t_0, \ldots, t_{n+1} = t_n + \Delta t, \ldots$. We begin by discretizing the equations of motion (2.2) in time. Thus, we invert the usual sequence of spatial and temporal discretization and discretize the governing equations in time prior to the introduction of a spatial discretization. For definiteness, we restrict our attention to the Newmark scheme [48, 9]:

$$\boldsymbol{\varphi}_{n+1} = \boldsymbol{\varphi}_n + \Delta t \mathbf{v}_n + \Delta t^2[(1/2 - \beta)\mathbf{a}_n + \beta \mathbf{a}_{n+1}] \tag{2.18}$$

$$\mathbf{v}_{n+1} = \mathbf{v}_n + \Delta t[(1-\gamma)\mathbf{a}_n + \gamma \mathbf{a}_{n+1}] \tag{2.19}$$

$$\rho_0 \mathbf{a}_{n+1} = \nabla_0 \cdot \boldsymbol{P}_{n+1} + \rho_0 \boldsymbol{B}_{n+1} \tag{2.20}$$

where $\mathbf{v}$ and $\mathbf{a}$ denote the material velocity and acceleration fields, and $\beta \in [0, 1/2]$ and $\gamma \in [0, 1]$ are the Newmark's parameters. This defines a non linear system of equations that can be solved using a Newton-Raphson iteration procedure. For the dynamic simulations that are presented in the following chapters, the explicit version of the previous system of equations is used. The second order accurate explicit scheme we used is obtained defining $\beta = 0$ and $\gamma = 1/2$ (see, [48, 9])

$$\boldsymbol{\varphi}_{n+1} = \boldsymbol{\varphi}_n + \Delta t \mathbf{v}_n + \frac{1}{2}\Delta t^2 \mathbf{a}_n \tag{2.21}$$

$$\mathbf{a}_{n+1} = \boldsymbol{M}^{-1}(\boldsymbol{R}^{ext}_{n+1} - \boldsymbol{R}^{int}_{n+1}) \tag{2.22}$$

$$\mathbf{v}_{n+1} = \mathbf{v}_n + \frac{1}{2}\Delta t(\mathbf{a}_{n+1} + \mathbf{a}_n) \tag{2.23}$$

The presented scheme is stable under the condition that the time step is below a critical time step. Typically, one would like to capture numerically dilatational waves (the fastest) propagation on any element of the mesh. The stable time step that is used in the calculations is

$$\Delta t_{\text{stable}} = C(\min_{\text{mesh}} \frac{h^e}{\sqrt{\frac{\lambda+2\mu}{\rho}}}) \tag{2.24}$$

where C is a security coefficient (of the order of 0.1), h^e is the dimension of element e, λ and μ are the Lamé coefficients. The stable time step is computed at regular intervals during the calculations and after every remeshing to take into account the changes in the mesh.

Next we turn to the computation of the updated stresses $\boldsymbol{P}_{n+1}$. For the class of elastic-plastic materials under consideration, this computation requires the integration of the constitutive equations in time. Additionally, for a minimum principle to be in operation the constitutive update must itself have a variational structure.

Let the state of the material be fully known at time t_n and let the deformation $\boldsymbol{F}_{n+1}$ and the temperature T_{n+1} at time t_{n+1} be given. The problem is to determine the state of the material at time t_{n+1} from this information. We begin by discretizing in time the flow rule (2.8) as:

$$\boldsymbol{F}^p_{n+1} = \exp(\triangle\varepsilon^p \boldsymbol{M})\boldsymbol{F}^p_n \tag{2.25}$$

where exp is the exponential mapping. Next, following Stainer and Ortiz [79] we formulate an incremental work-of-deformation function of the form:

$$\begin{gathered} f_n(\boldsymbol{F}_{n+1}, T_{n+1}; \varepsilon^p_{n+1}, \boldsymbol{M}) = \\ W^e(\boldsymbol{F}^e_{n+1}, T_{n+1}) + W^p(T_{n+1}, \varepsilon^p_{n+1}) + \triangle t \psi^*(\triangle\varepsilon^p/\triangle t, T_{n+1}) \end{gathered} \tag{2.26}$$

and define an effective work-of-deformation density $W_n(\boldsymbol{F}_{n+1}, T_{n+1})$ by minimization of f_n with respect to the effective plastic strain ε^p_{n+1} and the direction of plastic flow $\boldsymbol{M}$, i.e.,

$$W_n(\boldsymbol{F}_{n+1}, T_{n+1}) = \min_{\varepsilon^p_{n+1}, \boldsymbol{M}} f_n(\boldsymbol{F}_{n+1}, T_{n+1}; \varepsilon^p_{n+1}, \boldsymbol{M}) \tag{2.27}$$

subject to constraints (2.9) and (2.10) and the plastic irreversibility constraint

$$\triangle\varepsilon^p = \varepsilon^p_{n+1} - \varepsilon^p_n \geq 0 \tag{2.28}$$

Here and subsequently, we append a label n to the effective work-of-deformation density function W_n to signify the fact that it is strictly incremental and depends parametrically on the values of the state variables at time t_n. It bears emphasis that, in the present variational formulation, the incremental effective plastic strain and the direction of plastic flow are determined by the condition that they minimize the incremental work of deformation.

The key property of the effective work-of-deformation density is that $W_n(\boldsymbol{F}_{n+1}, T_{n+1})$ acts as a potential for the first Piola-Kirchhoff stress tensor $\boldsymbol{P}_{n+1}$ at time t_{n+1} [79], i.e.,

$$\boldsymbol{P}_{n+1} = \frac{\partial W_n}{\partial \boldsymbol{F}_{n+1}}(\boldsymbol{F}_{n+1}, T_{n+1}) \tag{2.29}$$

The consistent tangent moduli follow by linearization of (2.29) in the form:

$$D\boldsymbol{P}_{n+1} = \frac{\partial^2 W_n}{\partial \boldsymbol{F}_{n+1} \partial \boldsymbol{F}_{n+1}}(\boldsymbol{F}_{n+1}, T_{n+1}) \tag{2.30}$$

Evidently, the tangent moduli are symmetric owing to the potential character of the incremental stress-strain relations. An efficient implementation based on the use of logarithmic elastic strains has been given by Ortiz and Stainier [79]. The computation of the exponential and logarithmic mapping and their first and second linearization has been discussed at length by Ortiz *et al.* [77].

2.2.3 A minimum principle for the incremental problem

The incremental displacement problem for the deformation mapping $\boldsymbol{\varphi}_{n+1}$ at time t_{n+1} is now obtained by inserting the relation

$$\boldsymbol{F}_{n+1} = \nabla_0 \boldsymbol{\varphi}_{n+1} \tag{2.31}$$

which follows by evaluating (2.1) at time t_{n+1}, into the variational update (2.29), and substituting the result into the time-discretized equation of motion (2.20). The crucial observation is that the resulting problem follows by requiring the stationarity

of the incremental potential energy functional:

$$\Phi_n[\boldsymbol{\varphi}_{n+1}] = \int_{B_0} \frac{\rho_0}{2\beta} \left| \frac{\boldsymbol{\varphi}_{n+1} - \boldsymbol{\varphi}_{n+1}^{\text{pre}}}{\triangle t} \right|^2 dV_0 +$$

$$\int_{B_0} [W_n(\nabla_0 \boldsymbol{\varphi}_{n+1}) - \rho_0 \boldsymbol{B}_{n+1} \cdot \boldsymbol{\varphi}_{n-1}] dV_0 - \int_{\partial B_{02}} \boldsymbol{T}_{n-1} \cdot \boldsymbol{\varphi}_{n+1} dS_0 \tag{2.32}$$

where

$$\boldsymbol{\varphi}_{n+1}^{\text{pre}} = \boldsymbol{\varphi}_n + \triangle t \mathbf{v}_n + (1/2 - \beta) \triangle t^2 \mathbf{a}_n \tag{2.33}$$

is the Newmark predictor for the deformation mapping.

We make the additional physical assumption that, among all stationary points of Φ_n, the stable equilibrium configurations of the solid are the minimizers of Φ_n. This finally leads to the *minimum* principle:

$$\Phi_n[\boldsymbol{\varphi}_{n+1}] = \inf_{\boldsymbol{\eta} \in V} \Phi_n[\boldsymbol{\eta}] \tag{2.34}$$

where V is some suitable space of deformation mappings satisfying the essential boundary conditions (2.3).

Consider now a pair of incremental displacements $\mathbf{u}$ and $\mathbf{v}$ applied to the deformed configuration B_{n+1} satisfying homogeneous essential boundary conditions over ∂B_{01}. We then define the Dirichlet form of the problem as the second variation of the potential energy Φ_n at $\boldsymbol{\varphi}_{n+1}$, i.e.,

$$a_n[\boldsymbol{\varphi}_{n+1}](\mathbf{u}, \mathbf{v}) = \delta^2 \Phi_n[\boldsymbol{\varphi}_{n+1}](\mathbf{u}, \mathbf{v}) =$$

$$\int_{B_0} \left[\frac{\rho_0}{\beta \triangle t^2} \mathbf{u} \cdot \mathbf{v} + \{W_n\}_{,\boldsymbol{F}_{n+1}\boldsymbol{F}_{n+1}} (\nabla_0 \boldsymbol{\varphi}_{n+1}) \cdot (\nabla_0 \mathbf{u} \otimes \nabla_0 \mathbf{v}) \right] dV_0 \tag{2.35}$$

which, evidently, is symmetric. Thus, the variational structure of the problem ensures the existence of a symmetric Dirichlet form. We further recall from the classical

calculus of variations that if W_n is C^2 and $\varphi_{n+1} \in C^1(B_0; \mathbb{R}^d)$ is a solution of the Euler-Lagrange equations of Φ_n, then a sufficient condition for φ_{n+1} to be a weak relative minimum of Φ_n is that (coercivity condition)

$$a_n[\varphi_{n+1}](\mathbf{u}, \mathbf{u}) \geq C_1 \|\mathbf{u}\|_1^2 \tag{2.36}$$

for some constant C_1 and all $\mathbf{u} \in W^{1,2}(B_0; \mathbb{R}^d)$ satisfying homogeneous essential boundary conditions over ∂B_{01} [103, 8]. In the sequel, we shall confine our attention to solutions φ_{n+1} for which (2.36) holds.

2.3 Asymptotic *a-posteriori* error bounds

The preceding developments provide a suitable framework for error estimation and mesh adaption. We adopt a 'fine-mesh' viewpoint and confine our efforts to optimizing fine meshes leading to high-quality finite-element approximations. Mathematically, this focus gives us license to investigate the behavior of the finite element solutions *asymptotically* as the mesh size $h \to 0$. Throughout this section, we concern ourselves with the finite element solution at a fixed time, e.g., time t_{n+1}, and we shall omit the corresponding label $n+1$ for clarity. For simplicity of notation, we also omit the label n from the potential energy Φ_n, the Dirichlet form a_n, and the effective incremental strain-energy density W_n, which we have used to emphasize that these functions are incremental and depend on the initial conditions for the time step.

2.3.1 A local projection method of error estimation

The Euler-Lagrange equations corresponding to the variational problem (2.34) take the form

$$\langle D\Phi[\varphi], \mathbf{v} \rangle \equiv \left\{ \frac{d}{d\epsilon} \Phi[\varphi + \epsilon \mathbf{v}] \right\}_{\epsilon=0^+} = 0 \tag{2.37}$$

for all $\mathbf{v} \in V$ satisfying homogeneous boundary conditions on ∂B_{01}. Similarly the finite-element solution satisfies the stationarity condition

$$\langle D\Phi[\boldsymbol{\varphi}_h], \mathbf{v}_h \rangle = 0 \tag{2.38}$$

for all $\mathbf{v}_h \in V_h$ satisfying homogeneous boundary conditions on ∂B_{01}. Choosing $\mathbf{v} = \mathbf{v}_h$ in (2.37) and subtracting gives

$$\langle D\Phi[\boldsymbol{\varphi}_h] - D\Phi[\boldsymbol{\varphi}], \mathbf{v}_h \rangle = 0 \tag{2.39}$$

But, in the asymptotic regime of interest, $\boldsymbol{\varphi}_h$ may be expected to be close to $\boldsymbol{\varphi}$, and, to leading order as $h \to 0$, (2.39) becomes

$$a[\boldsymbol{\varphi}](\boldsymbol{\varphi}_h - \boldsymbol{\varphi}, \mathbf{v}_h) = 0 \tag{2.40}$$

where a is the Dirichlet form (2.35). Identity (2.40) expresses the orthogonality of the error function $\boldsymbol{\varphi}_h - \boldsymbol{\varphi}$ and V_h in the Dirichlet form at $\boldsymbol{\varphi}$ asymptotically as $h \to 0$. It also shows that the finite-element solution $\boldsymbol{\varphi}_h$ possesses the 'best-approximation' property, namely,

$$\|\boldsymbol{\varphi}_h - \boldsymbol{\varphi}\|_E = \min_{\boldsymbol{\eta}_h \in V_h} \|\boldsymbol{\eta}_h - \boldsymbol{\varphi}\|_E \tag{2.41}$$

where

$$\|\mathbf{u}\|_E = \sqrt{a[\boldsymbol{\varphi}](\mathbf{u}, \mathbf{u})} \tag{2.42}$$

is the energy norm at $\boldsymbol{\varphi}$. As it is well-known, the best-approximation property (2.41) and the coercivity assumption (2.36) give the error bound (*cf.* [19])

$$\|\boldsymbol{\varphi}_h - \boldsymbol{\varphi}\|_1 \leq C \sum_{e=1}^{E} (h^e)^k |\boldsymbol{\varphi}^e|_{k+1} \tag{2.43}$$

where k is the order of polynomial interpolation, $|\cdot|_{k+1}$ is the Sobolev H^{k+1}-seminorm, φ^e is the restriction of φ to the domain Ω_0^e of finite element e, h^e is the size of element e and we assume a lower bound for the aspect ratio of all elements.

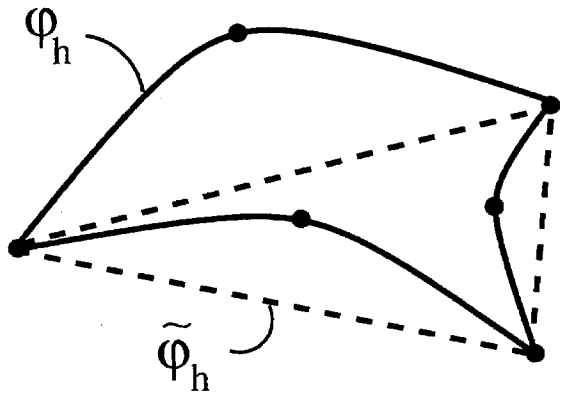

Figure 2.2: $(k-1)$ interpolant of φ_h

Instead of using the standard error bound (2.43) directly for purposes of mesh adaption, following Radovitzky and Ortiz [82], we formulate a purely local adaption strategy as follows. Assume that $k \geq 2$ and $\tilde{\varphi}_h$ be the $(k-1)$-interpolant of φ_h, Figure 2.2. For instance, if $k = 2$, i.e., if quadratic elements are used, then $\tilde{\varphi}_h$ is a piecewise linear deformation mapping which interpolates the positions of the corner nodes of the elements. The strategy consists of estimating–and optimizing the mesh so as to minimize–the error in $\tilde{\varphi}_h$, as opposed to the error in the finite-element solution φ_h itself. Begin by noting that, by the triangular inequality,

$$\|\tilde{\varphi}_h - \varphi\|_1 = \|(\tilde{\varphi}_h - \varphi_h) + (\varphi_h - \varphi)\|_1 \leq \|\tilde{\varphi}_h - \varphi_h\|_1 + \|\varphi_h - \varphi\|_1 \qquad (2.44)$$

But, asymptotically as $h \to 0$, the first term in the right-hand side is of order $O(h^{k-1})$, whereas the second term is of order $O(h^k)$ by virtue of the bound (2.43). Consequently, the first term dominates asymptotically with the result that

$$\|\tilde{\varphi}_h - \varphi\|_1 \leq C\|\tilde{\varphi}_h - \varphi_h\|_1 \qquad (2.45)$$

for some constant C, asymptotically as $h \to 0$. An application of the standard

interpolation error bounds (*cf.* [19]) to the right-hand side of (2.45) then gives

$$\|\tilde{\varphi}_h - \varphi\|_1 \leq C \sum_{e=1}^{E} (h^e)^{k-1} |\varphi_h^e|_k \tag{2.46}$$

asymptotically as $h \to 0$.

A careful examination of (2.46) reveals the following: i) the bound in (2.46) is expressed directly in terms of the finite-element solution φ_h, which makes the method *a posteriori*; and ii) the bound involves derivatives of order k of φ_h^e, which are well defined and readily computed at the element level. The problem of mesh adaption may now be identified with that of minimizing the bound (2.46), e.g., for a fixed number of elements E. A straightforward derivation (see, e.g., [82]) gives

$$h(\boldsymbol{X}) = A \left(\sum_{|\alpha|=k} |D^\alpha \varphi_h(\boldsymbol{X})|^2 \right)^{-1/(2(k-1)+d)} \tag{2.47}$$

and

$$A = \left[\frac{1}{E} \int_{B_0} \left(\sum_{|\alpha|=k} |D^\alpha \varphi_h(\boldsymbol{X})|^2 \right)^{d/(2(k-1)+d)} dV_0 \right]^{1/d} \tag{2.48}$$

Again we emphasize that the target mesh size distribution (2.47) is now defined in terms of purely local element-wise indicators requiring only the evaluation of the k^{th}-order derivatives of the local finite-element solution, which greatly facilitates the application of the method.

It should be noted that there are other research areas which deal with finding the exact value of the constant C used in Equation 2.46. In those cases, adaptive mesh generation is based on posteriori error estimates which are derived via duality arguments yielding bounds for functionals of the error. Rannacher (see [85, 84]), a leading investigator in this field, succeeded to derive accurate error estimates from the solutions of linearized dual problems in the case of perfect plasticity. Previously, the duality arguments were mainly applied to linear problems. However, in the case

of rate dependent large deformation plasticity, using those same methods is still an open question.

2.4 Heat generation and transfer

Impact and erosion mechanisms involve a number of strongly interacting mechanical and thermal processes. In the calculations, we would like to account for thermo-mechanical coupling and the interaction between friction, temperature and plasticity. The relevant balance law that needs to be considered in this case is the heat equation

$$\int_{B_t} \rho c \dot{T} \eta dV + \int_{\partial B_{tq}} h \eta dS = \int_{B_t} \mathbf{q} \cdot \nabla \eta dV + \int_{B_t} s \eta dV \tag{2.49}$$

where ρ is the mass density, c is the mass capacity, T is the temperature, h and s are source terms of heat, $\mathbf{q}$ is a heat flux and η is a virtual temperature field. The heat produced by friction and plastic work acts as a source for the thermal problem. The corresponding thermal softening influences in turn the mechanical problem.

The details of the numerical approach used to account for thermo-mechanical coupling may be found elsewhere [69, 15]. Here we restrict ourselves to noting the main sources of heat accounted for in the calculations. During the deformation of the bodies, a substantial amount of heat may be generated as a result of plastic working. The corresponding rate of heat supply per unit volume may be written in the form:

$$s = \beta \dot{W}^p \tag{2.50}$$

where $\dot{W}^p$ is the plastic power per unit deformed volume, and β is the fraction of plastic work converted into heat. The coefficient β is known to be a strong function of deformation for some materials [70]. Here, however, we treat β as a constant for the sake of simplicity. In addition, the rate at which heat is generated per unit area as a result of friction is

$$h = -\boldsymbol{t} \cdot [\![\boldsymbol{v}]\!] \tag{2.51}$$

where $\boldsymbol{t}$ is the contact traction vector and $[\![\boldsymbol{v}]\!]$ denotes the velocity jump across the contact surface. If, in addition, we assume Coulomb friction, (2.51) becomes:

$$h = \mu p v \tag{2.52}$$

where μ is the friction coefficient, p the applied pressure, and v the sliding velocity. The heat h is apportioned to the bodies in contact in accordance with the following equations [36]:

$$h_1 = \alpha_1 \mu p v \tag{2.53}$$

$$h_2 = (1 - \alpha_1) \mu p v \tag{2.54}$$

where the labels 1 and 2 refer to the bodies in contact and

$$\alpha_1 = \frac{1}{1 + \sqrt{k_2 c_2 \rho_2 / k_1 c_1 \rho_1}} \tag{2.55}$$

is the fraction of the work of friction which is transferred to body 1. In (2.55), $\{\rho_1, \rho_2\}$ are the mass densities, $\{c_1, c_2\}$ are the heat capacities, and $\{k_1, k_2\}$ are the thermal conductivities of the bodies in contact.

The mechanical and thermal field equations are coupled in two different ways. The mechanical response feeds into the thermal equations through the heat generation mechanisms expressed in (2.50) and (2.51). The reverse coupling comes from the softening effect of the temperature on the yield stress. A staggered procedure is adopted in order to account for this two-way coupling (e.g., [80, 61, 69, 15]). An isothermal explicit-dynamic step is first taken, based on the current distribution of temperatures, leading to an update of all mechanical variables. Since the temperatures are held constant throughout this step, they enter the constitutive relations as a parameter. The heat generated is computed from (2.50) and (2.51) and used to compute the heat source array energy-balance equation. A rigid-conductor forward-Euler step is then taken at constant mechanical state, leading to a new temperature distribution. In the applications of interest here, the mechanical equations always set

the critical time step for stability (e.g., [47, 48, 9]).

The Thermo-Mechanical coupling is summarized in the following steps:

- 1) Initialization of T_1, n=0
- 2) Isothermal mechanical step: $\boldsymbol{\varphi}_n, \mathbf{v}_n, \mathbf{a}_n, T_{n+1} \rightarrow \boldsymbol{\varphi}_{n+1}, \mathbf{v}_{n+1}, \mathbf{a}_{n+1}, T_{n+1}$
- 3) Heat generation (bulk + contact)
- 4) Rigid conductor step: $\boldsymbol{\varphi}_{n+1}, \mathbf{v}_{n+1}, \mathbf{a}_{n+1}, T_{n+1} \rightarrow \boldsymbol{\varphi}_{n+1}, \mathbf{v}_{n+1}, \mathbf{a}_{n+1}, T_{n+2}$
- 5) $n \rightarrow n+1$, go to 2)

2.5 Contact algorithm

Contact and friction must carefully be accounted for in impact simulation. The contact/friction algorithm enforces the impenetrability constraint, and determines the frictional forces and the extent of frictional dissipation, which is in turn fed into the energy equation as heat. Owing to the simple contact geometries considered here, we adopt a conventional master/slave approach with a predictor/corrector split within the Newmark time-stepping algorithm. A more general algorithm, which is applicable to complex nonsmooth contact situations, may be found elsewhere [54].

The predictor part of the Newmark algorithm neglects the contact constraints and, therefore, consists of an unconstrained step, with the result:

$$\boldsymbol{\varphi}_{n+1}^{pred} = \boldsymbol{\varphi}_n + \Delta t \mathbf{v}_n + \frac{\Delta t^2}{2} \mathbf{a}_n \tag{2.56}$$

$$\mathbf{v}_{n+1}^{pred} = \mathbf{v}_n + \frac{\Delta t}{2} (\mathbf{a}_n + \mathbf{a}_{n+1}) \tag{2.57}$$

This predictor solution needs to be corrected in order to comply with the impenetrability constraints. The net result of imposing these constraints is a set of self-equilibrated contact forces that modify the predictor positions and velocities. Since the contact surfaces are presumed smooth, normals are well-defined and the surfaces

can be unambiguously classified as master and slave. The final corrector configuration is, therefore:

$$\varphi^S_{n+1} = \varphi^{S,pred}_{n+1} - \frac{\Delta t^2}{2}\frac{\mathbf{N}^S_{n+1} + F^S_{n+1}}{M^S} \tag{2.58}$$

$$\mathbf{v}^S_{n+1} = \mathbf{v}^{S,pred}_{n+1} - \Delta t\frac{\mathbf{N}^S_{n+1} + F^S_{n+1}}{M^S} \tag{2.59}$$

$$\mathbf{v}^M_{n+1} = \mathbf{v}^{M,pred}_{n+1} + \Delta t\frac{\mathbf{N}^M_{n+1} + F^M_{n+1}}{M^M} \tag{2.60}$$

Here $M^{()}$ denotes the nodal mass and the superscripts $()^M$ and $()^S$ designate the nodes which belong respectively to the master and slave surfaces. It bears emphasis that the master and slave nodal subsets are strictly disjoint. Finally, the vectors $\mathbf{N}$ and $\mathbf{F}$ are respectively the normal and frictional forces.

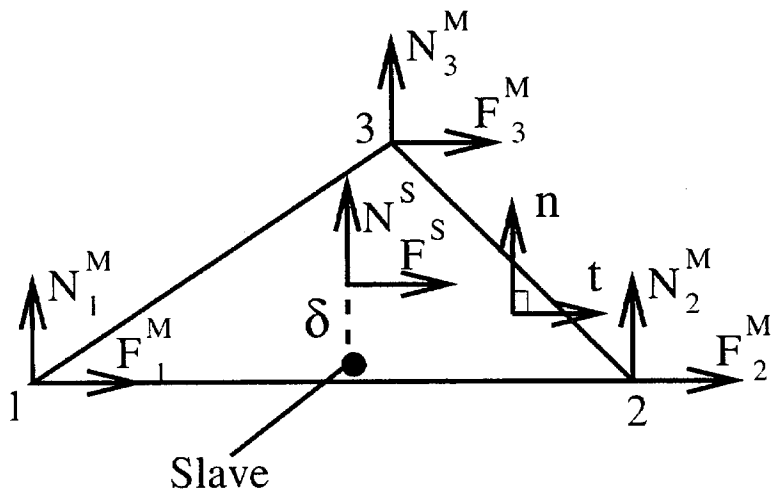

Figure 2.3: Slave node penetrating a master surface triangle

The centerpiece of the algorithm is the formulation of an appropriate system of normal and frictional forces. To this end, consider the configuration shown in Figure 2.3, in which a master surface triangle is penetrated by several slave nodes. For each of the penetrating slave nodes, let δ be the normal depth of penetration to be corrected by the contact forces. Each slave node additionally defines a relative velocity v_r with respect to the penetration point. This relative velocity is used to compute the frictional forces. The contact/friction constraints determine a local problem with the normal and frictional slave and master forces as the unknowns. The normal slave

force is obtained from conservation of linear momentum as a direct function of the penetration δ and the master normal, $\mathbf{n}$. The frictional slave force is assumed to lie on the master plane in the direction of the relative velocity, and its magnitude is given by the frictional law as a function, e.g., of the pressure, relative sliding velocity and temperature. These assumptions lead to the expressions:

$$\mathbf{N}^S_{n+1} = M^S \frac{2\delta}{\Delta t^2} \mathbf{n}^M_{n+1} \tag{2.61}$$

$$\mathbf{F}^S_{n+1} = f(p, v_r, T)\mathbf{t}_{n+1} \tag{2.62}$$

The master forces are given by carefully enforcing conservation of linear and angular momentum, which results in a system of equations per master triangle of the form:

$$\mathbf{N}^S_{n+1} = \sum_{nodes} \mathbf{N}^M_{n+1} \tag{2.63}$$

$$\mathbf{F}^S_{n+1} = \sum_{nodes} \mathbf{F}^M_{n+1} \tag{2.64}$$

$$\mathbf{0} = (\mathbf{N}^S_{n+1} \times \boldsymbol{\varphi}^S_{n+1} - \sum_{nodes} \mathbf{N}^M_{n+1} \times \boldsymbol{\varphi}^M_{n+1}) \times \mathbf{n}_{n+1} \tag{2.65}$$

$$0 = (\mathbf{F}^S_{n+1} \times \boldsymbol{\varphi}^S_{n+1} - \sum_{nodes} \mathbf{F}^M_{n+1} \times \boldsymbol{\varphi}^M_{n+1}) \cdot \mathbf{n}_{n+1} \tag{2.66}$$

It bears emphasis that the approach, which has been described, improves upon other master/slave predictor/corrector contact/friction algorithms, which do not exactly conserve linear and angular momenta. The contact algorithm developed by Taylor and Flanagan [99, 100] for the PRONTO2D and PRONTO3D explicit dynamic codes, which was used by Camacho [13] is therefore improved. It should also be pointed out that, due to the explicit treatment of the dynamics and the master/slave approach adopted, each slave node defines a simple local problem, which can be solved independently of the rest. This property renders the algorithm ideally suited for parallel processing.

Chapter 3 Adaptive meshing

3.1 Introduction

In the preceding chapter, we have discussed a general framework for mesh adaptivity in strongly nonlinear problems together with thermal aspects and the contact algorithm. This chapter is devoted entirely to one component of the finite-element methodology: adaptive meshing. Adaptive meshing is essential to the realization of the calculations in this thesis to eliminate deformation-induced distortion which inevitably accompanies unconstrained plastic flows. Adaptive meshing coupled with error estimation is also used to solve fine features in the solution such as shock fronts, microstructural evolution, singularities and material instabilities (shear bands). The chapter is organized as follows. Section 3.2 describes the adaption strategy, i.e., the coupling between the error estimates and the refinement and coarsening algorithms. We discuss transfer issues in Section 3.3. We will emphasize the problem of diffusion and the coupling of remeshing with our contact algorithm. Section 3.4 explains in detail the refinement algorithm whereas Section 3.5 describes our coarsening strategy. Section 3.6 is concerned with reference updating. This will emphasize that remeshing should be done on the deformed configuration to obtain good quality meshes. Finally, we illustrate the methodology (Section 3.7) with static convergence tests on a cracked solid.

3.2 Adaption strategy

A complete remeshing strategy based directly on the optimal mesh size distribution (2.47) has been discussed by Radovitzky and Ortiz [82]. In this approach, the mesh is regenerated in its entirety at regular intervals and reconstructed by a combination of nodal insertion in regular face-centered-cubic arrangements followed by a constrained-

Delaunay triangulation. The advantage of this method is that it affords a very high degree of control over the elements aspect ratio. However, while sufficient conditions for the existence of a constrained-Delaunay volume triangulation consistent with a given surface triangulation are known (e.g., [1]), in practice those conditions may not be attained for geometries with very small local feature sizes. An additional difficulty in the approaches based on complete remeshing is that the transfer of state variables may be too diffusive in problems with sharp deformation gradients, e.g., in problems involving shear bands. By contrast, local operations such as subdivision and edge collapse are not generally afflicted by closure problems and tend to minimize the extent of diffusion incurred during the transfer of state variables.

In the calculations presented in this thesis, remeshing is driven by the error bounds discussed in the foregoing. The connection between the two is as follows. We take each element contribution

$$I_r^e = (h^e)^{k-1} |\varphi_h^e|_k \tag{3.1}$$

to the error bound (2.46) as a *refinement indicator*. We slate an element for subdivision when

$$I_r^e \geq TOL_r \tag{3.2}$$

In addition, we assign to each edge e in the mesh a *coarsening indicator* I_c^e equal to the maximum of the error indicators I_r^e in the elements belonging to the 1-ring incident to edge e. We then target an edge e for collapse when

$$I_c^e \leq TOL_c \tag{3.3}$$

Evidently, if $TOL_c \ll TOL_r$, at any given stage of the solution there may be a sizeable fraction of elements which does not qualify for refinement or coarsening and, therefore, remain unchanged during remeshing. As discussed in Section 3.5, we append to Equation 3.3 additional conditions to ensure that the collapse operation does not

compromise the quality of the mesh or results in unacceptable volume changes due to the coarsening of the boundary description. We also resort to edge collapse in order to remove slivers from the mesh.

3.3 Mesh-to-mesh transfer operator

One critical aspect which sets history-dependent materials apart from elastic materials within the context of adaptive meshing is the need to transfer or 'remap' history state variables from the old mesh to the new mesh. Indeed, the incremental energy function $W_n(\boldsymbol{F}_{n+1})$ which serves as the potential function for the incremental stress-strain relations (2.29) and for the computation of the tangent moduli (2.30) depends parametrically on the state $\{\boldsymbol{F}_n^p, \mathbf{q}_n\}$ at the beginning of the time step. If the triangulations $\mathcal{T}_n$ and $\mathcal{T}_{n+1}$ at times t_n and t_{n+1}, respectively, are different due to remeshing, the initial state variables $\{\boldsymbol{F}_n^p, \mathbf{q}_n\}$ are interpolated on $\mathcal{T}_n$, whereas the updated state variables, nodal coordinates, velocities and accelerations are interpolated on the new mesh $\mathcal{T}_{n+1}$.

Ortiz and Quigley [76], for static problems, and Radovitzky and Ortiz [82], for dynamic problems, have shown how the variational principle (2.34) in fact supplies the requisite transfer operators. Conceptually, the situation is, simply, that the various fields at times t_{n-1}, t_n and t_{n+1} which enter into the computation of the incremental potential energy (2.32) are interpolated on different meshes. The variational transfer operator for displacements, velocities and accelerations turns out to be a mass-weighted L^2-projection from $\mathcal{T}_n$ to $\mathcal{T}_{n+1}$ [76]. However, by recourse to mass lumping, the mesh-to-mesh transfer operator for nodal fields may simply be reduced to a direct evaluation of the fields, as interpolated on the old mesh $\mathcal{T}_n$, at the nodes in the new mesh $\mathcal{T}_{n+1}$. Because of the local nature of the bisection and edge-collapse operations described subsequently, the transfer operator can be applied locally at the elements level within $\mathcal{T}_n$. To facilitate re-interpolation of nodal variables, the new nodes are placed by way of the isoparametric mapping evaluated at pre-determined natural coordinates (see, e.g., Figure 3.11).

In order for the variational principle to dictate the state-transfer operator, a precise form of the state-variable interpolation must be explicated. The representation adopted here is based on the Voronoi tessellation associated with the set of all quadrature points in the mesh. We choose to represent the state variable fields as constant over each of the Voronoi cells in the tessellation. Evidently, the value of the state variables over each cell equals their value at the corresponding quadrature point. For this representation, the variational approach of Ortiz and Quigley [76] reduces to simply assigning to each quadrature point on the new mesh the full set of state variables of the *closest* quadrature point in the old mesh. Here again, owing to the local nature of bisection and edge collapse, the state-variable transfer can be effected locally at the element level.

The overriding advantage of piecewise constant representation for the state variables, and the resulting transfer operator, is that whole collections of attendant state variables are transferred from quadrature point to quadrature point as blocks, thus preserving all internal constraints and the compatibility between the various state variables. These requirements may be violated by transfer operators which involve extrapolation from several quadrature points. Thus, for instance, in the context of isochoric plasticity, i.e., volume preserving, the plastic part of the deformation gradient $\boldsymbol{F}^p$ must have a determinant of 1. This nonlinear constraint is preserved by the piecewise constant transfer operator, but is violated upon extrapolation in general. Likewise, in the context of ideal plasticity, stresses transferred in accordance with the piecewise constant transfer operator, unlike extrapolated stresses, are guaranteed to satisfy the yield conditions.

Next, we comment on two critical issues for the transfer operator: diffusion and the coupling of transfer with our contact algorithm.

Diffusion Many adaptive meshing methods have as a significant drawback the production of diffusion. For instance, the advancing front method [17, 29, 83] presents the disadvantage of proposing no guarantees regarding the preservation of the demarcations of singularities. A schematic representation of diffusion is given in Figure 3.1.

A one-dimensional mesh (black points) is represented together with its interpolated field. There exists a zone, delimited by points A and B, where the values of the interpolated field are higher. The remeshing method replaces the old nodes by new nodes (in red in the figure). The boundary of the previous zone has now changed (A' and B') with its thickness being larger and the high intensity peak at C disappearing. This adaptive meshing scheme is clearly diffusive.

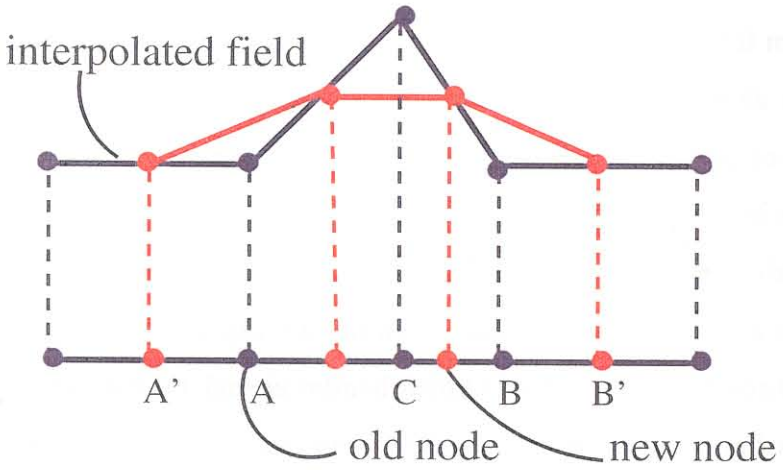

Figure 3.1: A diffusive remeshing scheme

Our strategy for adaptive meshing preserves the mechanical fields in an optimum way during the transfer operation from the old mesh to the new mesh. The subdivision method is not diffusive as all the new nodes are introduced within the already existing elements. Refinement does not change the boundary of shear bands and plastic or thermal boundary layers. The edge-collapse algorithm, which removes nodes, is on the other hand diffusive. However, its effect is delimited to regions where the error estimates are low. Therefore, its diffusive effect has no negative impact on the numerical results in the "mechanically interesting" regions.

Coupling remeshing/contact The first approach chosen for the nodal transfer was to interpolate the nodal values at every new point using the shape functions and the nodal values of the previous mesh. As the shape functions are quadratic,

this method of interpolation is inconsistent with the contact algorithm. Indeed, the contact algorithm searches penetration assuming that every facet is plane (linear interpolation). The negative impact of this implementation is that prior to remeshing, assuming the contact algorithm was successful, there is no penetration. However, after remeshing, some of the new nodes are either inside the contacting body and the contact needs to be restored, or away from the contact face and thus are not instantaneously accelerated due to contact forces. This source of mechanical fluctuations is illustrated in the following example. Figure 3.2 represents the initial mesh of a cube. One face is held fixed whereas the opposite face is in contact with a larger cube, which is not represented in Figure 3.2. The larger cube is moving to the right at a constant velocity and compresses the small cube. The contact face of the small cube is defined as a slave face in the contact algorithm. The non penetrability condition of the algorithm leads to a displacement at a velocity V of the face in the positive Y-axis direction. The contact face is refined using the subdivision algorithm at regular intervals of time. Figure 3.3 illustrates the negative effect of a quadratic remeshing transfer algorithm coupled with the contact algorithm. As can be observed from the fluctuations on the contact face instabilities have developed. The contact surface is non smooth which is totally unphysical and based solely on numerical error.

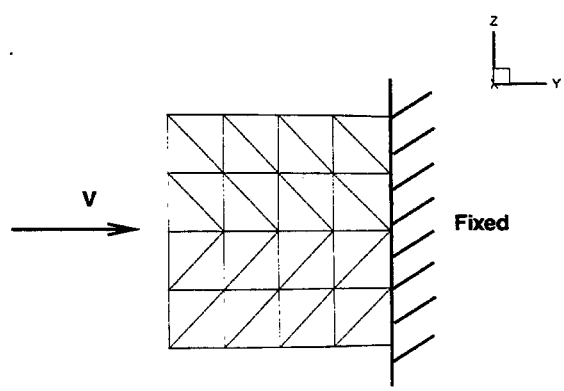

Figure 3.2: Initial configuration

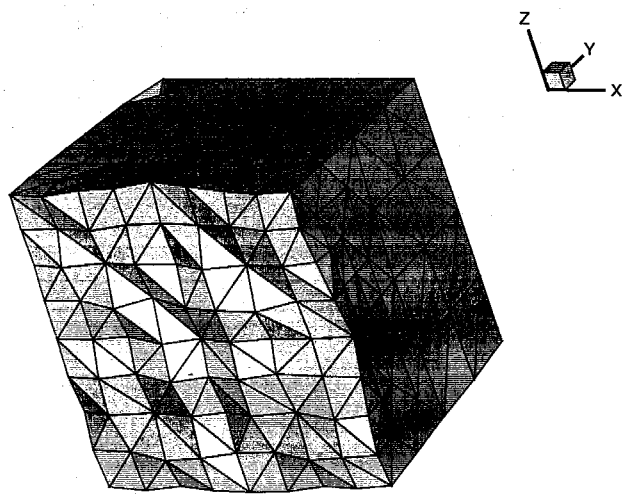

Figure 3.3: Illustration of the instabilities generated by the contact algorithm on a contact face

When dealing with contact surfaces, another approach for the nodal transfer should be taken to be consistent with the contact algorithm. The mechanical fields at the new nodes are obtained by linear interpolation of the old fields. Figure 3.4 illustrates the method when a quadratic tetrahedron is refined along an edge. The value at the four new nodes are computed using the values of nodes 1 and 5 for node 11, 5 and 2 for node 12, 6 and 7 for node 14 and 8 and 9 for node 13. This approach proved to be the most efficient. The effect on our model of the corrected transfer algorithm is shown in Figure 3.5. The contact face is perfectly smooth.

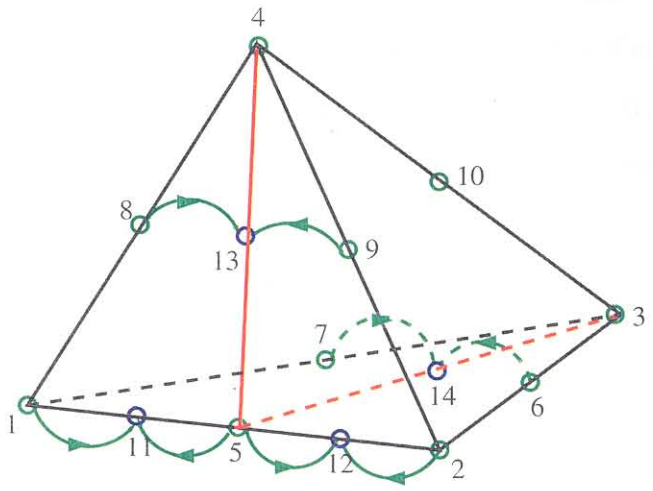

Figure 3.4: Illustration of the nodal transfer when subdividing a tetrahedron on a contact face

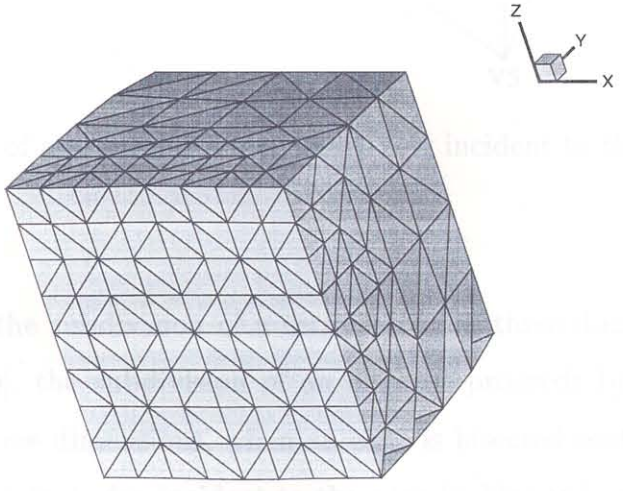

Figure 3.5: Successful nodal transfer algorithm

3.4 Subdivision algorithm

The first component of the adaptive meshing capability consists of the subdivision algorithm for mesh refinement. Our particular implementation of subdivision is based on Rivara's longest-edge propagation path (LEPP) algorithm [91, 89, 90]. Whereas the idea of a longest-edge propagation path is clear in two dimensions, describing the algorithm in three dimensions is less obvious. In three dimensions, we will prefer the use of the term longest-edge propagation graph (later called LEPG) to the term longest-edge propagation path. The reason why we deliberately choose the term graph will become clear in the following and it arises from an attempt to extend the description of the method of Rivara to three dimensions.

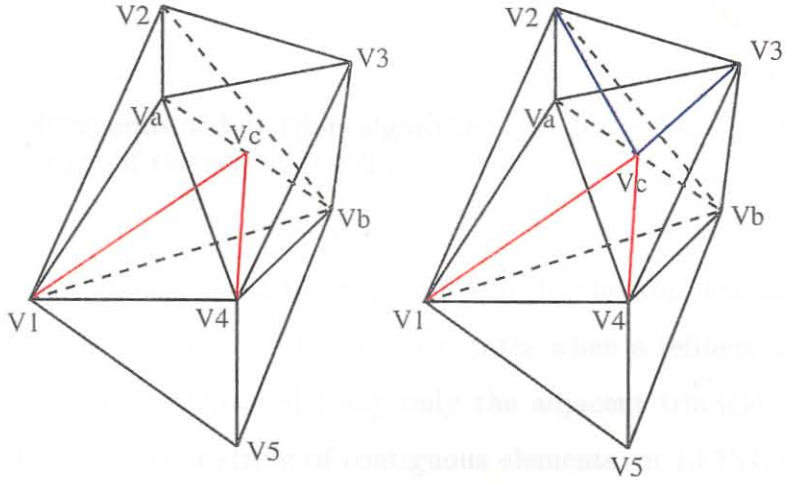

Figure 3.6: Bisection of a tetrahedron and the 1-ring incident to the bisected edge

Figure 3.6 illustrates the subdivision of a tetrahedron in three dimensions. Following Rivara [91, 89, 90], the subdivision of an element proceeds by bisection along its longest edge. In three dimensions, when an edge is bisected conformity demands that the entire ring of tetrahedra incident to the edge be bisected concurrently. This operation is illustrated in Figure 3.6, which depicts the bisection of edge $e = \{V_a, V_b\}$ of tetrahedron $\{V_1, V_4, V_b, V_a\}$, resulting in the insertion of vertex V_c. The remaining tetrahedra in the ring corresponding to edge e, namely, $\{V_a, V_4, V_b, V_3\}$, $\{V_1, V_a, V_b, V_2\}$

and $\{V_a, V_b, V_3, V_2\}$, must be bisected as well, resulting in the addition of four tetrahedra to the mesh. Evidently, the number of tetrahedra in the ring of an edge is arbitrary and varies widely in typical meshes.

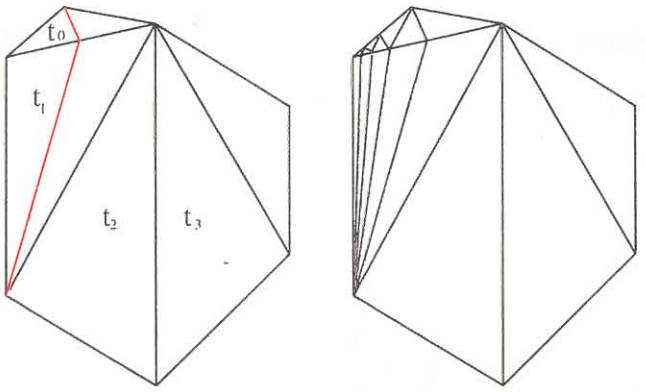

(a) (b)

Figure 3.7: A degenerate subdivision algorithm: (a) initial mesh, t0 is subdivided (red) (b) degeneracy of the mesh after 6 iterations

Simple longest-edge bisection alone may result in degenerate elements. Figure 3.7 illustrates how a two-dimensional mesh degenerates when a refinement operation of the upper left triangle is repeated using only the adjacent triangle. We overcome this difficulty by bisecting a string of contiguous elements, or LEPG, starting at the target element. Figure 3.8 illustrates a three-dimensional LEPG. Each vertex in the directed graph represents an element of the mesh. The vertex are linked to each other by directed edges which are the longest edges of the elements from which they emanate. In the case of Figure 3.8, we start from tetrahedron K_1 which is adjacent by its longest edge e_1 to five other tetrahedra: K_2, K_3, K_4, K_5 and K_6. We will explain in detail the construction of the LEPG in the direction of K_2 as it is the most interesting case in the figure. Indeed, K_2 has an edge e_2 which is larger than e_1. This edge is adjacent to two other tetrahedra, K_7 and K_8. The longest edge of K_7 is also e_2 and thus is a terminal vertex of the graph. Therefore, the edge joining the vertices K_2 and K_7 proceeds in both directions; it is in fact a cycle. K_7 is our first

candidate for subdivision. K_8, on the other hand, has a larger edge e_3 which brings the algorithm to the terminal tetrahedron K_9. The vertex K_2 has another interesting property: it has an edge e_4, shorter than e_2 but larger than e_1. Therefore, the element K_{10}, which is adjacent to K_2 along e_4 is a new member of the LEPG. K_{10} has another longest edge e_5, which belongs to K_7, a vertex that was previously encountered in the graph. In two dimensions, the term longest edge propagation path is clearly valid as the algorithm is sufficiently described by a tree. However, in three dimensions, the obtained configurations are graphs.

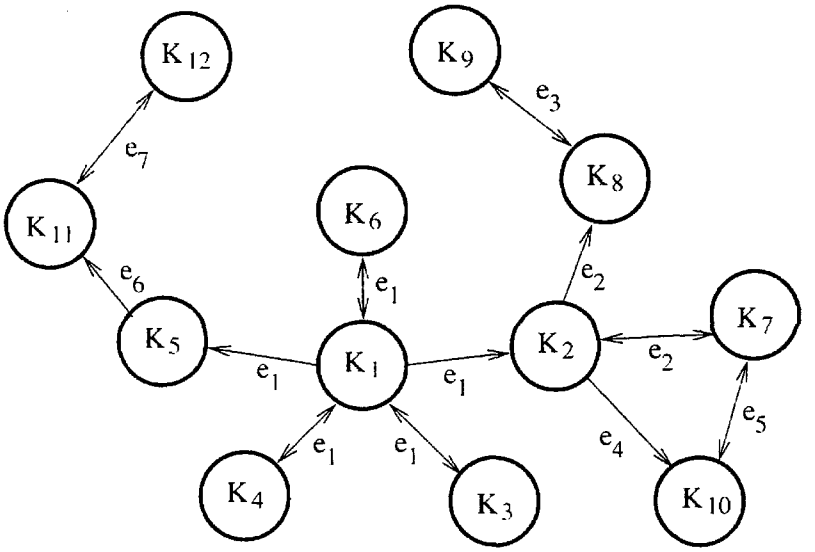

Figure 3.8: Longest-edge propagation graph of K_1

In practice the graph does not need to be constructed in full. In fact, obtaining the graph beforehand is a difficult task. It is easier to bisect the terminal tetrahedra as soon as they are encountered. Suppose that the tetrahedron K_1, as in Figure 3.8, is to be refined. Then the LEPG is generated recursively by the addition of new tetrahedra at the end of the path in accordance with the following rules:

1. Initialization: LEPG $= \{K_1\}$.

2. Let LEPG $= \{K_1, K_2, \ldots, K_{k+1}\}$ after k iterations of the algorithm. Then, the algorithm terminates if K_{k+1} is a terminal tetrahedron, i.e., if the following condition is satisfied:

   - The longest edge of K_{k+1} is shared with K_k.

3. If LEPG $= \{K_1, K_2, \ldots, K_{k+1}\}$ and K_{k+1} is not a terminal tetrahedron, then the new path is LEPG $= \{K_1, K_2, \ldots, K_{k+1}, K_{k+2}\}$, where K_{k+2} is the tetrahedron incident to K_{k+1} along its longest edge.

4. If LEPG $= \{K_1, K_2, \ldots, K_{k+1}\}$ and K_{k+1} is a terminal tetrahedron, then K_{k+1} is bisected along its longest edge and the new path is LEPG $= \{K_1, K_2, \ldots, K_k\}$. This step results in the addition of new nodes to the mesh.

5. The previous rules are repeated until K_1 is bisected.

Figure 3.9 describes the order in which the vertices of Figure 3.8 are visited. Each line corresponds to a bisection of a tetrahedron. For instance, the first line signifies that the LEPG $= \{K_1, K_2, K_8, K_9\}$ and K_9 is bisected which brings back the LEPG to K_8. Targeting initially K_1 for refinement leads to the bisection of 13 elements of the mesh (K_7 is counted twice).

Figure 3.10 illustrates the propagation of the refinement in two dimensions. Triangle T1 is targeted for refinement. Its longest edge is adjacent to T2 which in turn has another longest edge adjacent to T3. The longest edge of T3 is on the boundary and thus T3 is refined. At the next step, as T2 and T'3 share the same longest edge, we refine both triangles and introduce node 2. Node 3 and 4 are added in the same way. The algorithm terminates when triangle T0 is refined.

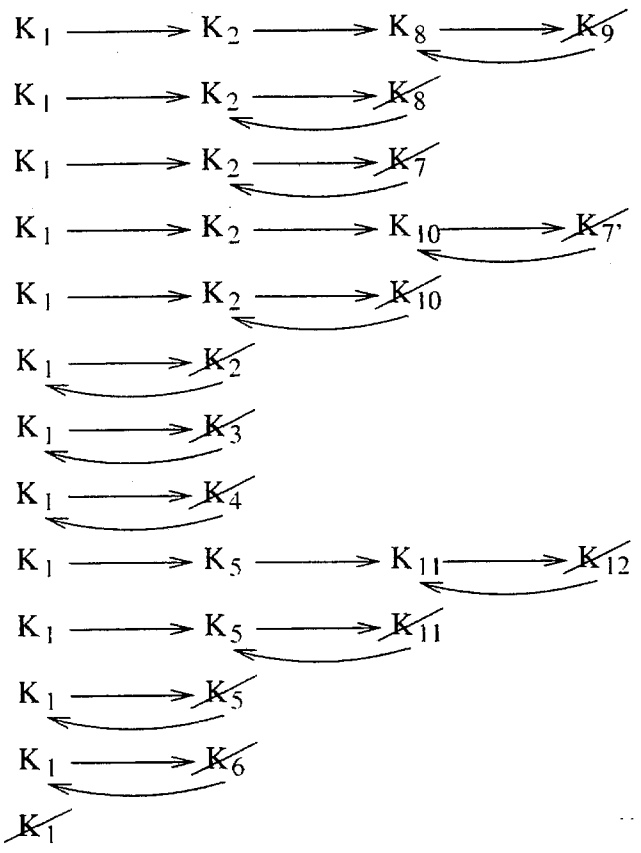

Figure 3.9: Order in which the tetrahedra are bisected during the LEPG of K_1

When higher-order elements are used, the additional off-vertex nodes may be added after the base simplicial complex has been refined. Figure 3.11 illustrates this operation for 10-node quadratic tetrahedra. It may be noted that the bisection of one quadratic tetrahedron results in the insertion of at most four new nodes V_a, V_b, V_c and V_d, Figure 3.11. Indeed, some of these nodes could have already been created at an earlier time in the LPEG if an adjacent element had been bisected. As the bisection of an initial element leads to the refinement of a whole graph (LEPG), an element could even be visited twice (or more) for refinement, Figure 3.8. Furthermore, this could happen at possibly two different edges and two far apart times. It is therefore important to have suitable data structures to verify that the nodes introduced by bisection are new or simply repeated. Appendix A contains the C-language data structures used in the subdivision algorithm (and also in the edge-collapse algorithm

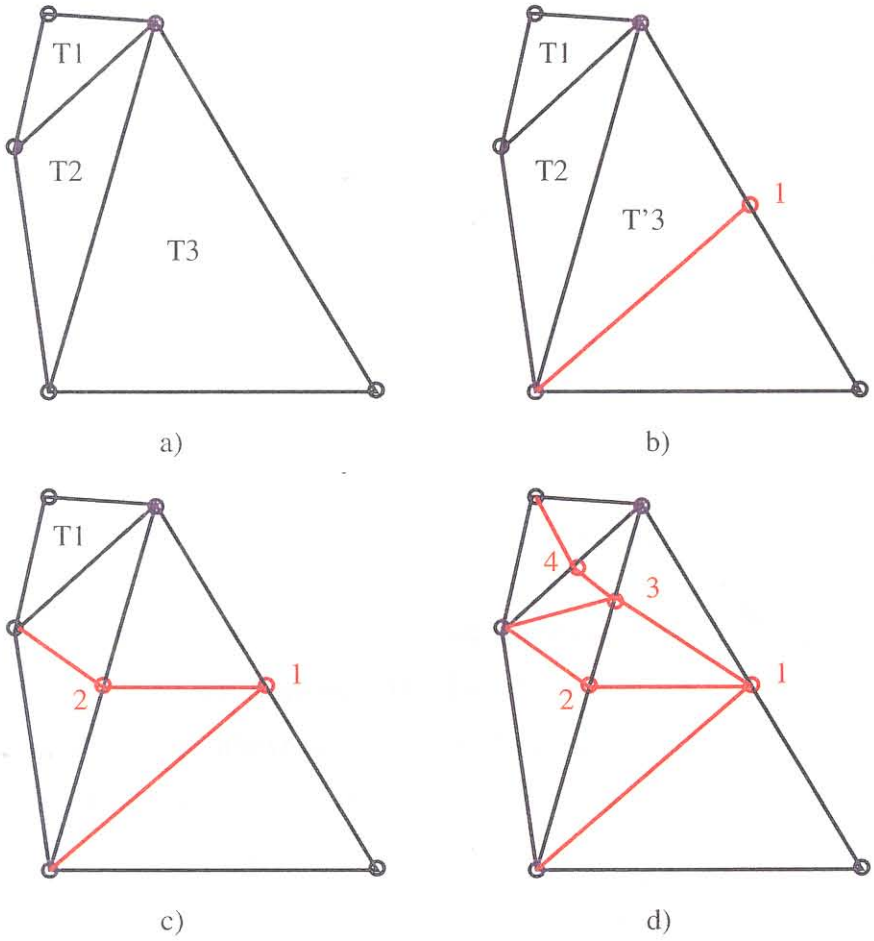

Figure 3.10: Longest-edge bisection of triangle t_0: (a) initial mesh; (b) first step in the process; (c) second step in the process; (d) final mesh

which will be explained in Section 3.5). We are using linked lists of nodes and tetrahedra to facilitate the dynamic memory allocation of new elements. It is important to emphasize that each element in the tetrahedra list is pointing to nodes via the connectivity array (ix) and the temporary storage space (xadd) for the nodes that have been created on adjacent tetrahedra. Also, each node is pointing to the tetrahedra to which it belongs (adj structure). These cross linkings clarify the algorithm and speed up the searches tremendously. The following data structures do not correspond to the classical data structures used in finite-element calculations. They are therefore created locally, in the remeshing algorithm, for the purpose of clarity and efficiency. At the end of the procedure their content is rewritten in the proper finite-element for-

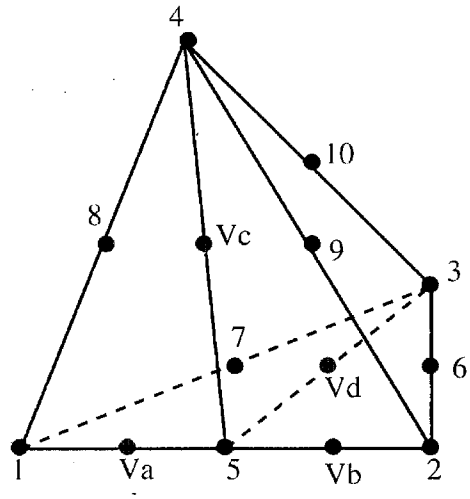

Figure 3.11: Bisection of a quadratic tetrahedron

mat and the structures are destroyed. Using the local data structures the algorithm is organized as follows (see Appendix B). For all the elements of the mesh, we check if their error estimate is above a user defined threshold (TOL_r). If so, we call the LongestEdgePath subroutine, which code is reproduced in Appendix B. The Conform subroutine searches the longest edge, shifts to one of the adjacent tetrahedron and checks if it reached a terminal tetrahedron, meaning one which shares the same longest edge as the previous one in the path (ListConform data structure). If this is verified the subroutine is exited, otherwise it calls LongestEdgePath recursively. Whenever SplitTetrahedron is called, the algorithm is pointing to the terminal tetrahedron of the ListConform data structure. This call has the effect of subdividing the element and conducting the local transfer of the nodal and element variables (Gauss points).

The algorithm was verified reproducing the results of Rivara [91]. Four tetrahedra of varying qualities were chosen and subdivided recursively using the 3-D LEPP. Following Rivara [91] and Sommerville [95] we measure the quality of the tetrahedra constructed. We associate to each vertex P of each tetrahedron T the value:

$$\phi_P = sin^{-1}(1 - cos^2\alpha_P - cos^2\,\beta_P\, - cos^2\,\gamma_P + 2\,cos\,\alpha_P\,cos\,\beta_P\,cos\,\gamma_P)^{1/2} \quad (3.4)$$

where α_P, β_P and γ_P are the three coterminous planar interior angles associated with vertex P. The square root of the term involving the angles is called the sine of the solid angle of the tetrahedron. The quality of a tetrahedron is then:

$$\phi_T = min_{(P \in T)}\ \phi_P \tag{3.5}$$

The results of Rivara were reproduced exactly up to a certain refinement level where the choice of the longest edge is not unique and bifurcations in the meshes are obtained. The LEPG algorithm always terminated after a finite number of steps and the quality of each mesh at high degrees of refinement had a lower bound.

3.5 Edge collapse

Next we turn to edge collapse as a mesh-coarsening method. In three dimensions, interior edges may be collapsed to their midpoint, which results in a net loss of one corner node and the elimination of the complete ring of tetrahedra incident to the edge. Figure 3.12 illustrates this basic collapse operation on a simple three-dimensional mesh. The initial mesh contains seven nodes and five tetrahedra: $t_1 = \{V_a, V_3, V_4, V_2\}$, $t_2 = \{V_1, V_a, V_4, V_2\}$, $t_3 = \{V_1, V_b, V_5, V_4\}$, $t_4 = \{V_1, V_b, V_4, V_a\}$ and $t_5 = \{V_a, V_b, V_4, V_3\}$. The collapse of edge $\{V_a, V_b\}$ onto the midpoint V_c eliminates the tetrahedra t_4 and t_5 and results in a coarser mesh consisting of six nodes and the three tetrahedra t_1', t_2' and t_3'. These tetrahedra are deformed from t_1, t_2 and t_3 by the dragging of V_a and V_b towards the midpoint V_c. Of particular concern as regards the implementation of the method is the treatment of boundaries and material interfaces (*cf.* [96, 45, 55, 57]). In two dimensions, we distinguished four cases depending on the position of the nodes of the edge to be collapsed. A node can either be inside the domain (interior node) or on the boundary of the domain. In that case it can be on an edge or at the intersection of two edges (corner node). The following cases are represented in Figure 3.13:

- the two nodes are inside the domain (Figure 3.13(a))

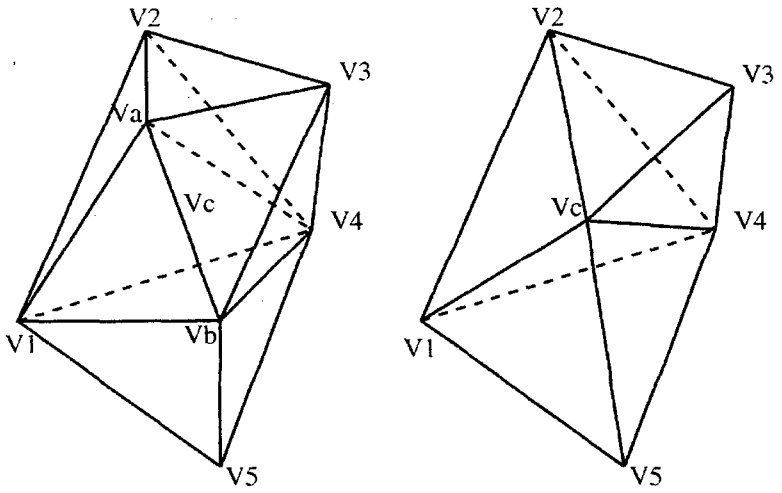

Figure 3.12: Basic edge-collapse operation in three dimensions

- one node is inside the domain, whereas the other is on the boundary (Figure 3.13(b))
- the two nodes are on the boundary, but there are no corner nodes (Figure 3.13(c))
- the two nodes are on the boundary and one is a corner node (Figure 3.13(d))

The cases where the two nodes belong to two different global edges, or are both corner nodes, are forbidden. Allowing them would change drastically the boundary representation of the solid.

In three dimensions the number of possible situations is larger. A complete enumeration of these cases is collected in Table 3.1. The operations listed in the table are designed so as to preserve the topology of the domain and sharp geometrical features of the boundary such as global edges and vertices. It should be carefully noted, however, that the identification of global edges and vertices depends on the choice of tolerance. In our calculations, the edges are determined keeping in memory the initial boundary representation of the solids. A boundary edge could also be identified as a global edge when the dihedral angle subtended by the boundary at the edge is under (sharp edge) or exceeds (groove) a given tolerance. Finally, a boundary vertex is identified as a global vertex if it is at the intersection of two global edges.

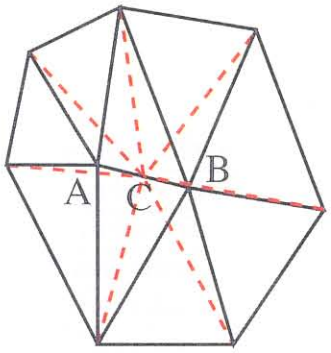

(a) 2 nodes inside the domain, projection on C

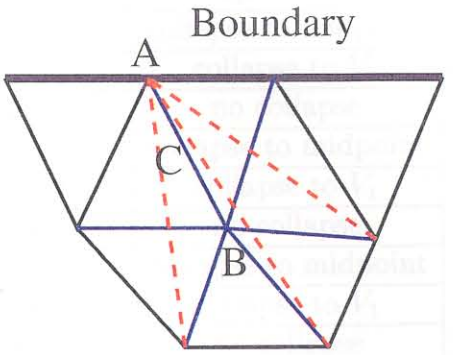

(b) 1 node on the boundary, the other inside the domain, projection on A

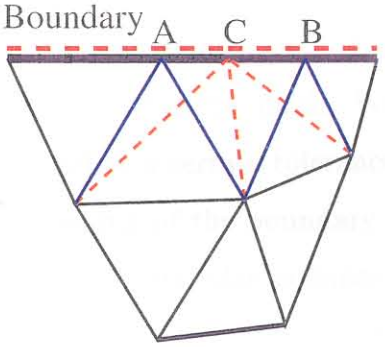

(c) 2 nodes on the boundary, no corner nodes, projection on C

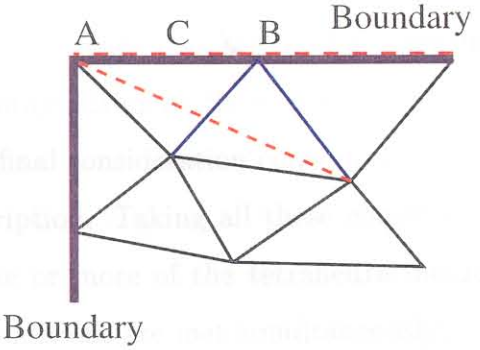

(d) 2 nodes on the boundary, one corner node, projection on A

Figure 3.13: Collapse operations in 2-D, the old mesh is represented in black, the blue lines disappear and the dashed red lines are new edges

In some cases, the edge-collapse operation worsens the aspect ratio of the elements. This is not particularly critical from an accuracy standpoint since, by the nature of coarsening criterion, edge collapse tends to occur in regions where the deformation gradients are small and the elements are nearly uniformly deformed. Even so, we append to the coarsening criterion additional criteria in order to prevent an unacceptable deterioration of the mesh quality. Following Rivara [91] (Equations 3.4 and 3.5), we adopt as the measure of the quality of a tetrahedron the minimum of the solid angles at its four vertices. This measure ranges from 0, corresponding to a

edge	V_1	V_2	operation
interior	interior	interior	collapse to midpoint
interior	boundary	interior	collapse to V_1
interior	boundary	boundary	no collapse
boundary face	face interior	face interior	collapse to midpoint
boundary face	face boundary	face interior	collapse to V_1
boundary face	face boundary	face boundary	no collapse
global edge	edge interior	edge interior	collapse to midpoint
global edge	edge boundary	edge interior	collapse to V_1
global edge	edge boundary	edge boundary	no collapse

Table 3.1: Possible configurations for the edge collapse in three dimensions

sliver, to 45° for a regular tetrahedron.

As already mentioned, we additionally use edge collapse to eliminate such slivers as may be present in the mesh. We identify slivers as those elements whose quality measure is below a certain tolerance. A final consideration concerns loss of mass due to the coarsening of the boundary description. Taking all these considerations into account, we perform edge collapse if one or more of the tetrahedra incident on an edge are slivers, or if all the following conditions are met simultaneously:

1. The edge error indicator I_c^e falls below the threshold TOL_c.

2. Edge collapse is geometrically possible, Table 3.1.

3. The average quality of the product tetrahedra exceeds the average quality of the original tetrahedra.

4. The quality of the worst product tetrahedron exceeds the quality of the worst original tetrahedron.

5. The total volume of the product tetrahedra is close to the total volume of the original tetrahedra.

   In our experience these criteria provide an effective means of mesh-quality control during coarsening.

3.6 Reference updating

In impact and shear band calculations where large plastic deformations occur, the mesh may get heavily distorted. Adaptive meshing is a tool that has been developed in order to overcome this difficulty. However, when the displacements are large, adaptive meshing alone is not sufficient. It has to be coupled with reference updating. Changing periodically the reference configuration allows us to remesh on the deformed configuration. As a consequence, a better mesh will be produced to continue with the calculations. We update the reference configuration by adding the displacements to the coordinates of the reference configuration, with the result

$$\varphi = \varphi_{ref} + \mathbf{d} \tag{3.6}$$

Figure 3.14 represents the change from the initial reference configuration, B_0 to the new one B_{ref}. $F_{0\to ref}$ maps B_0 to B_{ref}. $F_{ref\to n}$ maps B_{ref} to the configuration B_n at time t_n. $F_{n\to n+1}$ maps B_n to the configuration B_{n+1} at time t_{n+1}. Those deformation mappings can be related to each other via composition of functions; see Equations 3.7-3.10. Even though the reference configuration is updated, one always computes the deformation gradient with respect to B_0 to preserve the whole history of deformation; see Equations 3.9, 3.10.

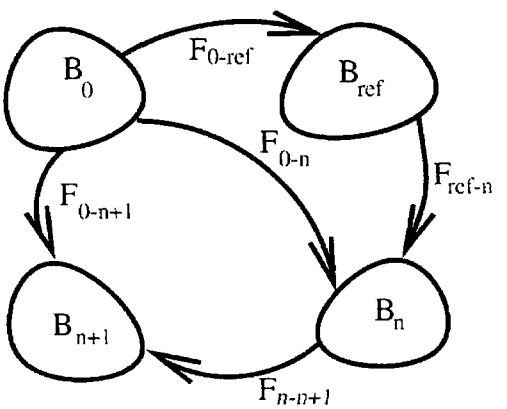

Figure 3.14: Changes of configurations

$$\boldsymbol{F}_{0\to n+1} = \boldsymbol{F}_{n\to n+1}\boldsymbol{F}_{ref\to n}\boldsymbol{F}_{0\to ref} \tag{3.7}$$

with

$$\boldsymbol{F}_{0\to n-1} = \nabla_0 \boldsymbol{\varphi}^{n+1} \tag{3.8}$$

$$\boldsymbol{F}_{0\to ref} = \nabla_0 \boldsymbol{\varphi}^{ref} \tag{3.9}$$

$$\boldsymbol{F}_{n\to n+1} = \boldsymbol{F}_{0\to n+1}\boldsymbol{F}^{-1}_{0\to n} \tag{3.10}$$

When the reference configuration is updated during remeshing, the shape functions and their derivatives will be computed from then on with respect to the reference configuration. To obtain the deformation gradient with respect to B_0 it is necessary to modify the shape functions using the current value of the deformation gradient.

3.7 Static convergence tests

In this section we test the performance of the method of mesh adaption in the presence of strong elastic singularities. We will analyze the convergence properties as well as the quality of the meshes which are produced by subdivision and edge collapse. To this end we consider the standard problem of a mathematically sharp crack in a linear elastic solid, Figure 3.15. The precise dimensions used in calculations are $H/L = \frac{1}{2}$, $W/L = \frac{1}{8}$ and $a/L = \frac{1}{2}$, and the Poisson's ratio of the solid is $\nu = 0.3$. In order for the problem to possess an exact solution, we subject the boundary of the domain of

analysis to the plane strain mode-I displacement K-field (e.g., [86]):

$$u_1 = 0 \tag{3.11}$$

$$u_2 = \frac{K_I}{2\mu}\sqrt{\frac{r}{2\pi}}\cos\frac{\theta}{2}\left[3-4\nu-1+2\sin^2\frac{\theta}{2}\right] \tag{3.12}$$

$$u_3 = \frac{K_I}{2\mu}\sqrt{\frac{r}{2\pi}}\sin\frac{\theta}{2}\left[3-4\nu+1-2\cos^2\frac{\theta}{2}\right] \tag{3.13}$$

Here (r,θ) denotes a system of polar coordinates defined within planes perpendicular to the crack front, with the polar angle θ measured from the plane of the crack. The symmetry of the solution about the plane of the crack permits restricting the analysis to the halfspace $X_3 \geq 0$, Figure 3.15. The initial coarse mesh used as the starting point of the calculations is of uniform size and contains 576 elements, Figure 3.16, and was generated using the advancing-front Delaunay method of Radovitzky and Ortiz [83]. The loading parameter K_I is increased from zero to a maximum value $K_I/E\sqrt{a} = 0.6$, where E is the Young's modulus of the material and a is the crack length, and subsequently decreased to zero again. All calculations are performed using ten-node quadratic tetrahedral elements.

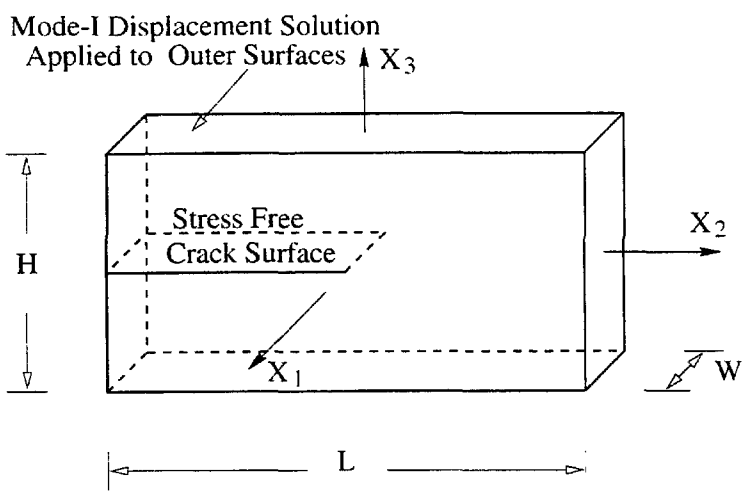

Figure 3.15: Initial geometry

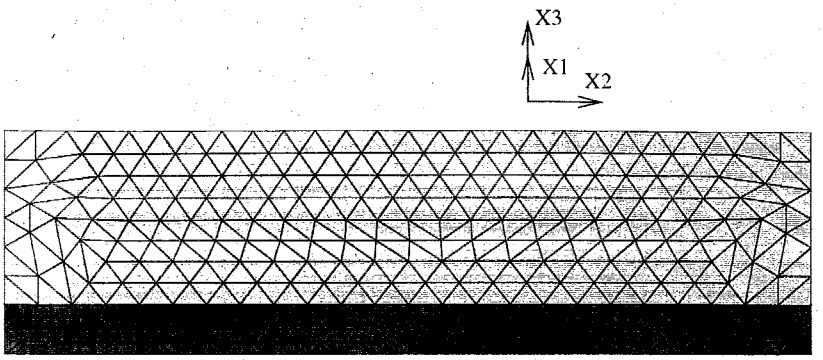

Figure 3.16: Initial coarse mesh used in convergence tests

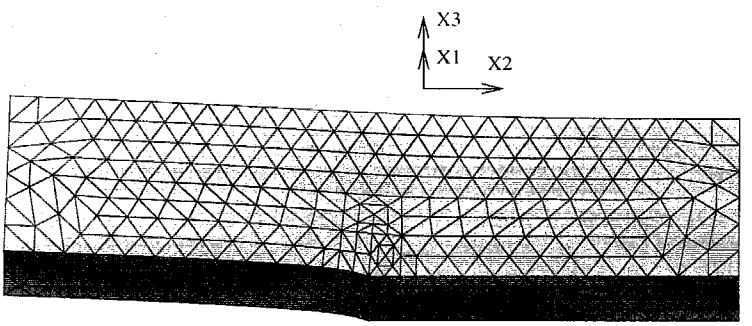

(a)

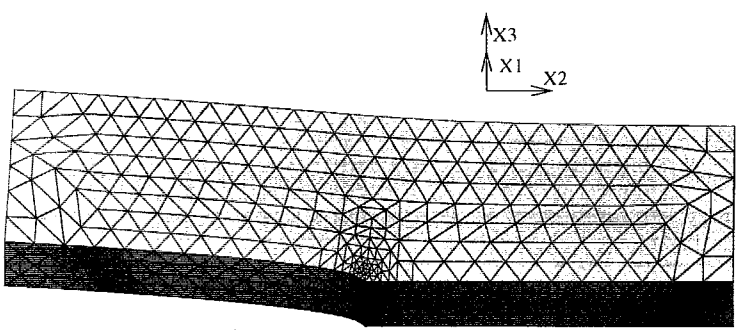

(b)

Figure 3.17: Evolution of the mesh in the cracked solid test: a) Intermediate mesh with 8 levels of subdivision, 265 elements; b) Final mesh at peak load with 13 levels of subdivision, 3807 elements

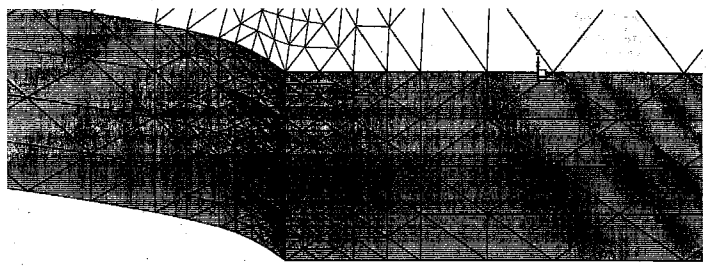

(a)

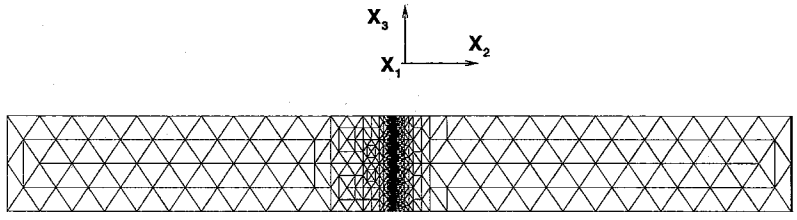

(b)

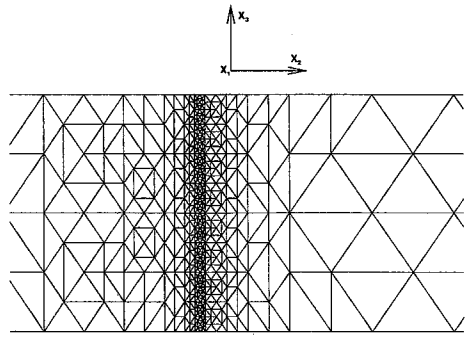

(c)

Figure 3.18: Cracked solid test: Detail of the near-tip region of the final mesh at peak load; a) Overall view; b) Full view from below of the mesh on the plane of the crack; c) Detail of the near-tip region

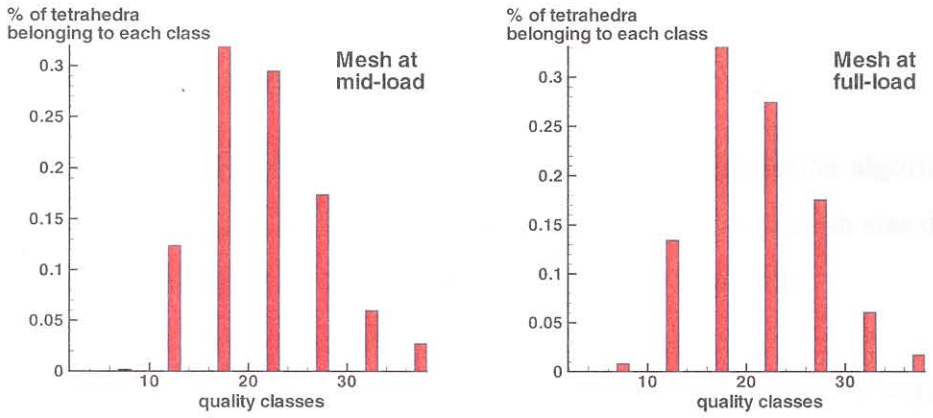

(a) (b)

Figure 3.19: Histograms of element quality at two stages of loading: a) Intermediate mesh with 8 levels of subdivision, 1127 elements; b) Final mesh at peak load with 13 levels of subdivision, 3807 elements

The evolution of the mesh during the loading phase is shown in Figures 3.17-3.18. The tolerance used in the subdivision criterion (3.2) is $TOL_r = 0.3$. It is evident from the figures that the mesh undergoes increasing refinement near the tip as the loading parameter K_I is increased. Mesh quality histograms at two stages of deformation are shown in Figure 3.19. As before, the quality of a tetrahedron is identified with the sum of the solid angles at its four vertices [95, 91], Equations 3.4 and 3.5. We classify the elements into eight groups depending on their respective quality:

- quality from 0 to 5 (very bad quality)
- quality from 5 to 10 (poor quality)
- quality from 10 to 15 (below average quality)
- quality from 15 to 20 (average quality)
- quality from 20 to 25 (above average quality)
- quality from 25 to 30 (good quality)

- quality from 30 to 35 (very good quality)
- quality from 35 to 40 (highest possible quality)

The good quality of the elements generated by the LEPG bisection algorithm, which for the most part remains above 15, is noteworthy. The optimal mesh size distribution for the displacement field (3.13) predicted by (2.47) is (see [82]):

$$h(r,\theta) = A\left(\frac{2^7\pi\mu^2}{K_I^2}\right)^{1/4} r^{3/4}\Big[\big(33-56\nu+32\nu^2+3(-7+8\nu)\cos(2\theta)-4\cos(3\theta)\big)^2 + \big(21-40\nu+32\nu^2+3(5-8\nu)\cos(2\theta)+4\cos(3\theta)\big)^2\Big]^{\frac{1}{8}} \tag{3.14}$$

where the constant A follows from (2.48). Thus, the optimal mesh consists of elements whose size decreases to zero as $r^{3/4}$ as the crack tip is approached. As may be seen from Figure 3.17, the refinement strategy outlined in Section 3.4 effectively results in an optimal element-size distribution.

The convergence curves for the error $\|\varphi_h - \varphi_{exact}\|_1$ and $\|\tilde{\varphi}_h - \varphi_{exact}\|_1$, predicted by the method, are also shown in Figures 3.20-3.21. The convergence curves clearly exhibit the optimal convergence rates, $O(N^{-2/3})$ for φ_h and $O(N^{-1/3})$ for $\tilde{\varphi}_h$, despite the presence of a strong elastic singularity. By contrast, the convergence rate is sub-optimal in the case of uniform refinement, as expected from the presence of singularities in the solution.

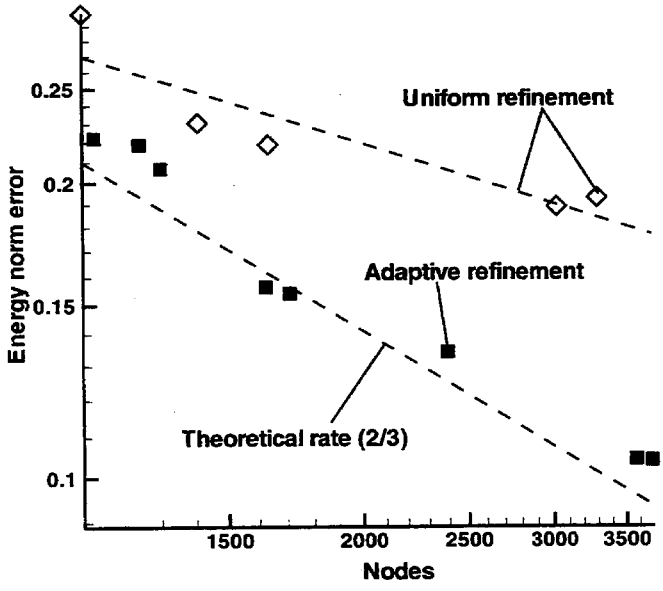

Figure 3.20: Energy norm error of φ

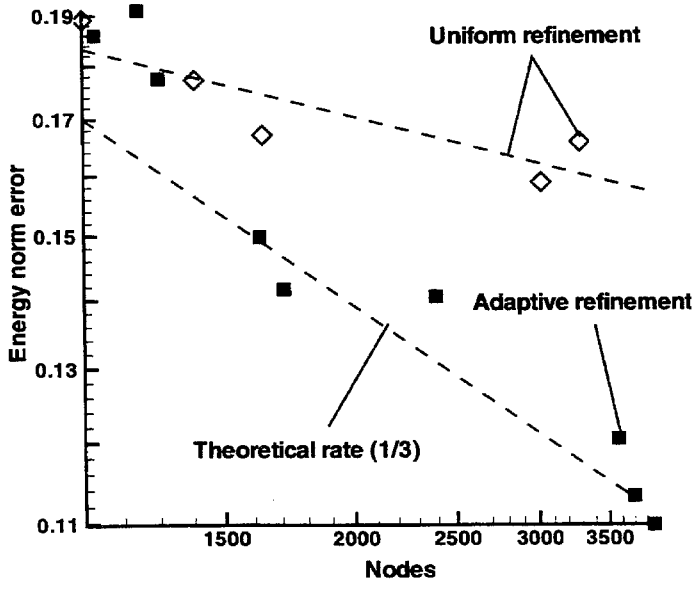

Figure 3.21: Energy norm error of $\tilde{\varphi}$

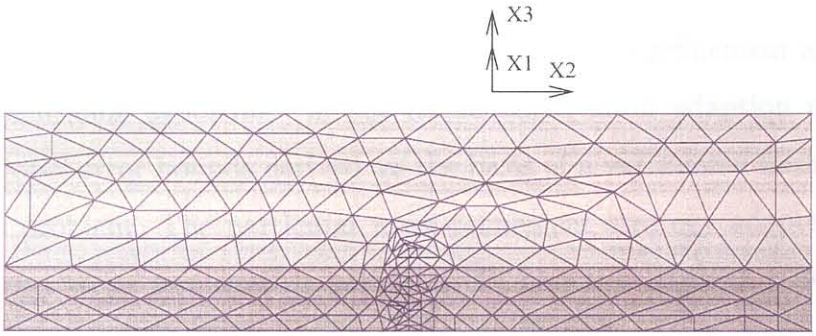

(a)

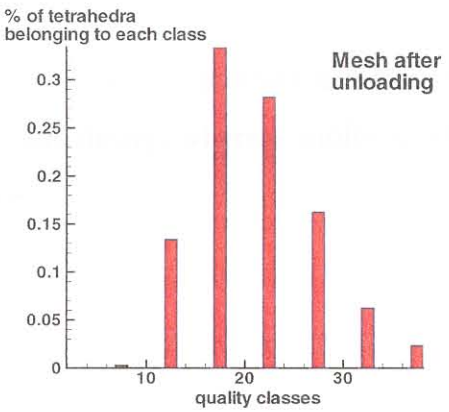

(b)

Figure 3.22: Illustration of the edge-collapse algorithm: a) Unrefined mesh after unloading; b) Element quality histogram

The final unrefined mesh after unloading is shown in Figure 3.22a. As is evident from this figure, the coarsening algorithm eliminates most of the fine mesh introduced by subdivision, as expected. A number of residual elements smaller than the initial element size is left in the final unrefined mesh due to the aspect-ratio constraints imposed on the edge-collapse operation (*cf.* Section 3.5). Thus, we see that these constraints inhibit coarsening to some extent. A histogram of element qualities for the final unrefined mesh is shown in Figure 3.22. This histogram suggests that the edge-collapse algorithm does effectively preserve the quality of the mesh.

3.8 Conclusions

We have presented a general framework for adaptive mesh refinement and coarsening in three-dimensional problems. In our formulation, mesh adaption is driven by *a posteriori* global error bounds derived on the basis of a variational formulation of the incremental problem. The particular mesh-refinement strategy adopted is based on Rivara's longest-edge propagation path (LEPP) bisection algorithm [91, 89, 90] and has been extended to three dimensions. Our strategy for mesh coarsening, or unrefinement, is based on the elimination of elements by edge collapse. The edge-collapse algorithm is also used to remove elements with low aspect ratio. The convergence characteristics of the method in the presence of strong elastic singularities have been tested numerically. We find that the method exhibits the optimal convergence rate predicted by approximation theory, whereas uniform refinement suffers from a sub-optimal convergence rate.

Chapter 4 Application to adiabatic shear banding

4.1 Introduction

Solids deforming at high rates often develop narrow layers of intense shearing [5, 22, 12, 97, 6, 106, 92]. Outstanding features of dynamic shear bands are their thinness, with typical widths of 10-100 μm [60], high local shear strains, which can reach values of up to 100 [106, 92, 102], ultra-high local shear strain rates, often in excess of 10^6 s^{-1} [106, 92, 102], local temperature rises of several hundred degrees [20, 38, 39, 67, 18, 70], and high propagation speeds, sometimes in excess of 1000 m/s [70, 110, 111, 108, 34]. In addition, cracks, whether the result of brittle fracture [6, 27], or of microvoid growth and coalescence [51, 46, 35, 109, 70], often form along shear bands.

Shear banding furnishes a prime example of the class of problems to which the framework outlined in the foregoing is intended to apply. In particular, we note that the underlying constitutive behavior loses stability and, correspondingly, the equilibrium equations lose ellipticity following the onset of shear banding (e.g., [88, 71, 32, 72]). In a time-discretized setting, shear banding coincides with the loss of rank-one convexity of the incremental potential energy. Evidently, in the presence of such strong material instabilities the static equilibrium problem is massively ill-posed. However, inertia and rate-sensitivity have a strong stabilizing effect and, in some cases, may render the incremental problem well-posed (see, [33, 73]) and the solution unique up to finite time, at least in the presence of imperfections. In particular, one may hope that when inertia and rate-sensitivity are accounted for, the coercivity condition (2.36) is satisfied for a sufficiently small time step.

The calculations presented here are motivated by the cylinder implosion tests of Nesterenko *et al.* [75]. In these tests, a metallic cylinder is subjected to explosive

loading by the detonation of a charge surrounding the cylinder. The deformation field of the collapsing cylinder involves two families of spiraling shear bands [75]. Our calculations are designed so as to roughly replicate the nominal conditions experienced by an individual shear band. The material considered is tantalum.

4.2 Numerical model

The specific model used in calculations is as follows. We assume the elastic strain energy to be quadratic and isotropic in the logarithmic elastic strains:

$$\boldsymbol{\epsilon}^e = \frac{1}{2}\log(\boldsymbol{C}^e) \tag{4.1}$$

where

$$\boldsymbol{C}^e = \boldsymbol{F}^{eT}\boldsymbol{F}^e \tag{4.2}$$

is the elastic right Cauchy-Green deformation tensor. The elastic strain energy is, therefore,

$$W^e = \frac{K}{2}(\theta^e)^2 + \mu|\mathbf{e}^e|^2 \tag{4.3}$$

where K is the bulk modulus, μ is the shear modulus,

$$\theta^e = \mathrm{trace}(\boldsymbol{\epsilon}^e) = \log(J^e) \tag{4.4}$$

is the volumetric elastic strain, and

$$\mathbf{e}^e = \boldsymbol{\epsilon}^e - \frac{1}{3}\theta^e\boldsymbol{I} \tag{4.5}$$

is the deviatoric elastic strain. For simplicity we neglect thermal expansion and the temperature dependence of the elastic moduli. The computation of W^e and the corresponding stress-strain relations and tangent moduli requires the evaluation of

the exponential and logarithmic mappings and their first and second linearizations. Simple explicit formulae for the evaluation of these objects may be found elsewhere [77].

Following Ortiz *et al.* [79], we assume power-law hardening. The corresponding stored energy function is:

$$W^p = \frac{n\sigma_0(T)\varepsilon_0^p}{n+1}\left[1+\left(\frac{\varepsilon^p}{\varepsilon_0^p}\right)\right]^{(n+1)/n} \tag{4.6}$$

where n is the hardening exponent, ε_0^p is a reference plastic strain, and $\sigma_0(T)$ is the flow stress. In addition, we assume an exponential thermal-softening law of the form:

$$\sigma_0(T) = \sigma_y \mathrm{e}^{\gamma(-T/T_0)} \tag{4.7}$$

where σ_y is the yield stress at zero absolute temperature and T_0 is a characteristic temperature. Finally, we assume power-law rate-sensitivity. The corresponding dual kinetic potential is [79]:

$$\psi^*(\dot{\varepsilon}^p, T) = \frac{m\sigma_0(T)\dot{\varepsilon}_0^p}{m+1}\left[1+\left(\frac{\dot{\varepsilon}^p}{\dot{\varepsilon}_0^p}\right)\right]^{(m+1)/m} \tag{4.8}$$

where m is the rate-sensitivity exponent and $\dot{\varepsilon}_0^p$ is a reference plastic strain rate. For simplicity, we neglect heat conduction and assume adiabatic heating of the form:

$$\rho_0 c_v \dot{T} = \beta \dot{W}^p \tag{4.9}$$

where c_v is the specific heat per unit mass at constant volume and β is a constant which expresses the fraction of plastic work which is converted into heat (see [98, 70, 43, 94]).

The uniaxial true stress-true strain law defined by these relations at constant strain rate is:

$$\sigma = \sigma_y\left[1+\left(\frac{\varepsilon^p}{\varepsilon_0^p}\right)^{1/n}+\left(\frac{\dot{\varepsilon}^p}{\dot{\varepsilon}_0^p}\right)^{1/m}\right]\mathrm{e}^{-\gamma(T/T_0)} \tag{4.10}$$

This relation has been fitted to the experimental data of Hoge and Mukherjee (1977) [44], Nemat-Nasser and Isaacs [74], and Vecchio [104] for polycrystalline Ta. The resulting material constants are tabulated in Table 4.1.

ρ	16620 Kg/m^3
E	185 GPa
ν	0.33
σ_y	150 MPa
ε_0^p	0.9
n	5
$\dot{\varepsilon}_0^p$	0.025
m	12.5
γ	0.0046 K^{-1}
T_0	300 K
T_{ref}	298 K

Table 4.1: Material constants for polycrystalline tantalum

The calculations are concerned with a coupon of material of dimensions $1 \times 0.2 \times 8$ mm^3 embedded within the cylindrical specimens of Nesterenko *et al.* [75] at a location such that, in the course of the test, a shear band cuts through the mid-plane of the coupon. The domain of analysis is subjected to the nominal conditions experienced by the coupon during the test. We assume these to consist of a prescribed velocity V_0 at the ends of the coupon imparting the material a nominal shear-strain rate $\dot{\gamma} = 2.5 \times 10^4$ s^{-1}. The domain of analysis is also given an initial linear velocity field

$$V_1 = \dot{\gamma} X_3 \tag{4.11}$$

corresponding to a uniform shear-strain rate at the nominal prescribed value $\dot{\bar{\gamma}}$. In order to simulate periodic boundary conditions and alleviate the computational burden, we constrain the displacements in the X_2 (thickness direction, plane strain) and X_3 (transverse) direction throughout the calculations. Thus, the only unconstrained degrees of freedom are the displacements in the X_1 or shearing direction. By virtue of

these kinematic constraints, the calculations simulate a plate of infinite extent in the X_1 direction. In order to fix the nucleation site for the shear band, we additionally introduce a thickness imperfection about the plane $X_2 = 0$ such as shown in Figure 4.1b. The maximum nominal shear strain imparted to the specimen at the end of the calculations is $\gamma = 0.45$.

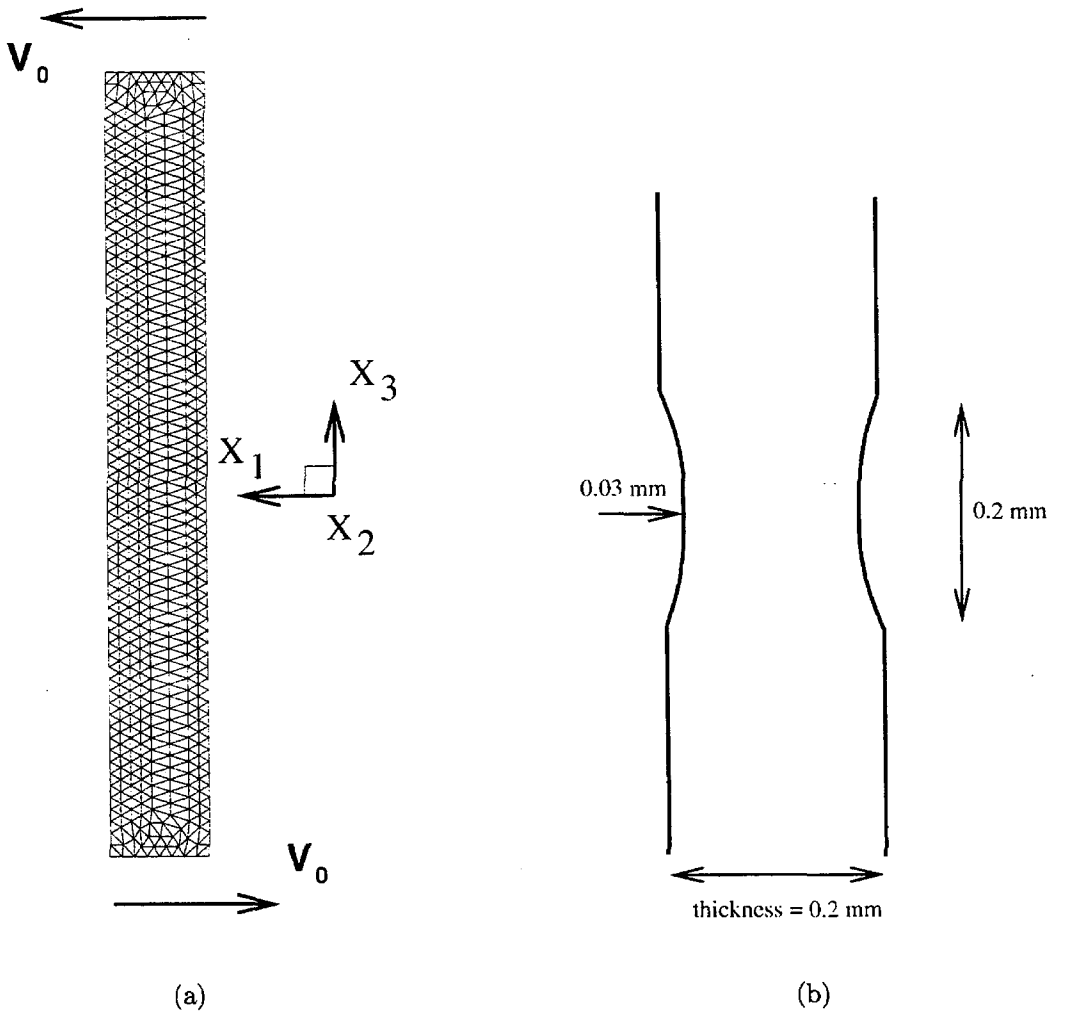

Figure 4.1: a) Geometry of the coupon analyzed in the shear banding simulation; all degrees of freedom other than the X_1-displacements are constrained; initial mesh containing 1574 elements; b) thickness imperfection

The domain of analysis and the coarse initial mesh are shown in Figur all degrees

of freedom other than the X_1-displacements are constrained;e 4.1a. This initial mesh was generated using the advancing-front Delaunay method of Radovitzky and Ortiz [83]. The initial mesh size on the mid-plane of the specimen is $h_{\min} = 0.14$ mm. The initial mesh contains 3439 nodes and 1574 elements. The method of solution is explicit dynamics. The time step is set to 10% of the elastic stable time step for explicit integration. The tolerance TOL_r for refinement is set to 0.1. Since the deformation gradients are monotonically increasing functions of time, no unrefinement is necessary during the calculations.

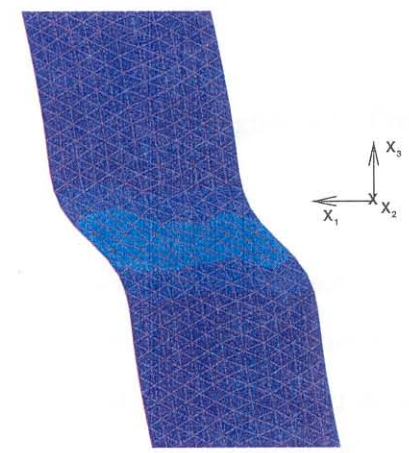

(a) t = 10.7μs

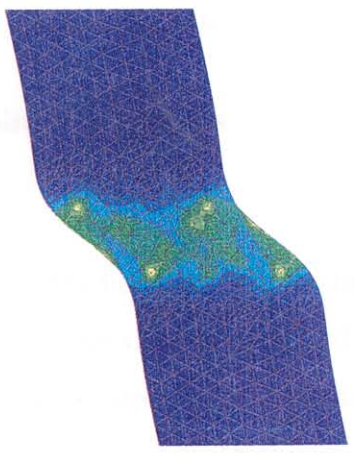

(b) t = 12.4μs

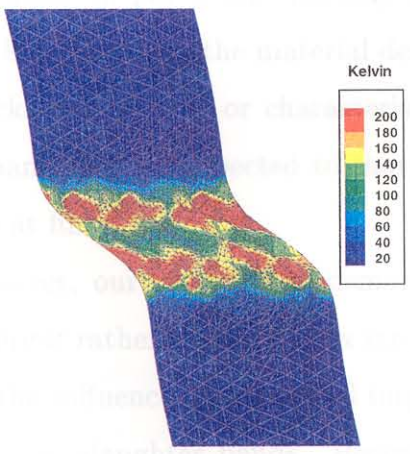

(c) t = 13.1μs

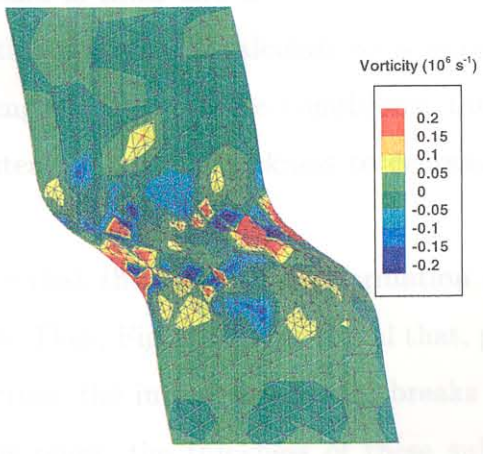

(d) Vorticity, t = 13.1μs

Figure 4.2: Temperature increase (a), (b), (c), and vorticity contour plots

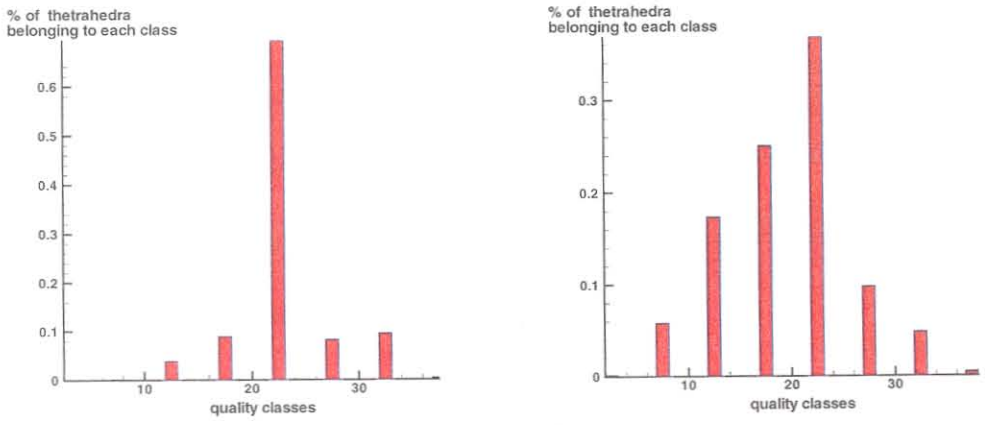

(a) Initial mesh

(b) Final mesh

Figure 4.3: Element qualities histograms

The evolution of the deformation and temperature fields, as well as the evolution of the computational mesh, are shown in Figure 4.2. The deformation and temperature fields remain ostensibly uniform up until the onset of instability. Beyond this point, deformations become increasingly localized. Evidently, the thickness imperfection has the effect of focusing the initial instability around the mid-section of the coupon, Figure 4.2a. In particular, initially the band is thick and fills the imperfection. It should be noted that the material description used in the calculations is purely local and lacks an intrinsic or characteristic length. Under these conditions, the initial shear band may be expected to sharpen steadily and its thickness to decrease down to zero at finite time.

However, our calculations demonstrate that the collapsing deformation pattern may exhibit rather more complex structure. Thus, Figures 4.2b-c reveal that, perhaps under the influence of the initial imperfection, the initial shear band breaks up and spawns two daughter bands. Beyond this point, the thickness of these sub-bands is independent of the imperfection thickness. It is also interesting to note that the nucleation of the sub-bands is not homogeneous, but rather starts at discrete sites, or 'hot spots', within the parent shear band. The intricate structure of the deformation

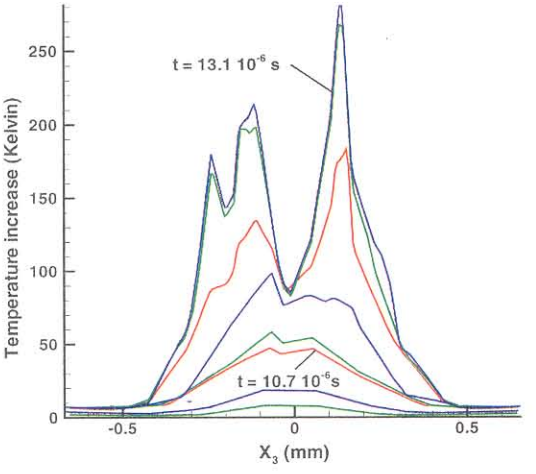

(a) Temperature evolution

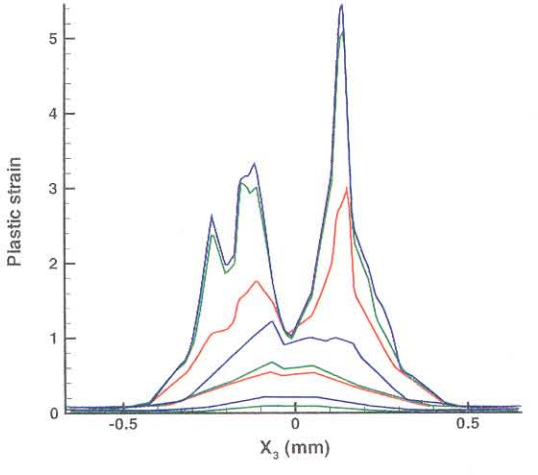

(b) Plastic strain evolution

Figure 4.4: Time evolution of temperature and plastic strain across the band thickness

fields that develop is further exemplified by the vorticity field shown in Figures 4.2d. The existence of multi-dimensional unstable deformation modes and vorticity patterns in competition with the homogeneous shear band mode has been pointed out by Leroy and Molinari [72, 62]. Recently, Guduru *et al.* [37] observed experimentally similar vortices in a shear band emanating from a crack tip.

The structure of the evolving temperature and deformation fields is further illustrated in Figure 4.4. The process of breakdown of the initial band into sub-bands is clear in this figure. The figure also suggests that the daughter sub-bands further break up into still finer sub-bands. It is tempting to speculate that this process of bifurcation of bands into sub-bands continues indefinitely, with the deformation and temperature fields acquiring increasing complex structure, possibly fractal in the limit.

The ability of the numerical solution to develop these fine structures is due entirely to adaptive mesh refinement. Figures 4.2a-c show how the mesh effectively adapts to the evolving solution. At maximum deformation, the element size at the center of the bands reduces to $h_{\min} = 0.015$ mm, and the number of elements increases to 10147. Also, histograms of tetrahedral quality, Figure 4.3, reveal that the mesh remains of good quality throughout the calculation. It bears emphasis that the method of adaption performs well under rather extreme conditions of geometric and material nonlinearity, including strong material instabilities such as shear banding.

4.3 Conclusions

The general framework for adaptive mesh refinement and coarsening has been tested in a three-dimensional finite-deformation dynamic-plasticity problem. The simulation consists of adiabatic shear banding in dynamically loaded tantalum. The results demonstrate the ability of the approach to adaptively resolve the increasingly fine structure of the shear band. They also suggest that, owing to the stabilizing effect of inertia and rate sensitivity, the error bounds remain applicable well after the equilibrium equations lose ellipticity.

We conclude by noting that, while methods of error estimation and mesh adaption for linear problems have attained a certain degree of maturity (e.g., [105]), specially in two dimensions, rigorous *a posteriori* error bounds and robust adaption strategies for strongly nonlinear three-dimensional dynamic problems are comparatively less developed (see, e.g., [76, 23, 59, 10], for some notable exceptions). It is, of course, possible

to study meshing and mesh adaptivity from a purely geometrical point of view. However, in the type of applications discussed above, mesh adaption is inextricably tied to the mechanics and physics of the problem, and is but one among a vast array of computational techniques required to carry out the calculations successfully. In addition, it bears emphasis that the mesh adaption strategy must make sense–and retain its robustness–in the face of finite deformations, history effects, dynamics, viscosity, and strong material instabilities such as adiabatic shear banding.

Chapter 5 Application to impact erosion

5.1 Introduction

This section is concerned with the analysis of impact damage. We apply the finite-element methodology described in Chapters 2 and 3. The calculations are carried out within the Lagrangian and explicit-dynamic frameworks. A new numerical difficulty is added by the coupling of the contact algorithm with adaptive meshing. We seek to determine the essential components of the adopted mechanical methodology and the range of validity of a rigid sphere model for impact erosion. The section is organized as follows. First, we describe our numerical model as well as some relevant numerical aspects in Sections 5.2 and 5.3. Then, we compare the obtained numerical results with the experimental data of Hutchings [49]. Hutchings [49] conducted a large number of experiments in which a mild-steel plate was impacted by 9.5 mm hard-steel spherical projectiles at various impact angles and speeds. The idea behind these experiments was to understand the erosion of metallic targets by the impact of abrasive particles, particularly when plowing instead of cutting deformation occurs. The large set of experimental data is used to validate the present finite element methodology. The comparison is presented in Section 5.4 which not only validates our numerical approach but also gives valuable insight into some aspects of the physics of impact mechanics and erosion. Finally, we carry out some parametric studies at higher impact speeds in Section 5.5.

5.2 Constitutive model

Upon impact, the bodies in contact are expected to undergo very large plastic deformations. In order to account for this effect, we adopt a standard formulation of finite-deformation plasticity based on a multiplicative decomposition of the deforma-

tion gradient into elastic and plastic components. We further assume J_2 plasticity and an isotropic hardening law of the form (e.g., [24, 69, 15]):

$$\frac{\dot{\epsilon^p}}{\dot{\epsilon_0^p}} = \left(\frac{\bar{\sigma}}{g(\epsilon^p, T)}\right)^m - 1 \tag{5.1}$$

$$g = \sigma_y \left[1 - \left(\frac{T - T_{ref}}{T_{melt} - T_{ref}}\right)^\alpha\right] \left(1 + \frac{\epsilon^p}{\epsilon_0^p}\right)^{\frac{1}{n}} \tag{5.2}$$

Here, $\bar{\sigma}$ is the effective Von Mises stress; ϵ^p is the effective plastic strain; $\dot{\epsilon^p}$ is the effective plastic strain rate; ϵ_0^p is the reference plastic strain; $\dot{\epsilon_0^p}$ is the reference plastic strain rate; m is the rate sensitivity exponent; n is the hardening exponent; g is the flow stress; σ_y is the initial yield stress; T_{ref} is the reference temperature; T_{melt} is the melting temperature; and α is the thermal softening exponent.

5.3 Numerical model

The material used in the simulation was a rectangular plate of mild steel. The material parameters for the mild-steel plate are given in Table 5.1. For the spherical projectile, the only material parameter that was changed was the yield stress: $\sigma_y = 1430MPa$. The initial mesh used in all the calculations is shown in Figure 5.1 and is nearly uniform. The plate is fixed in all directions in the bottom face, and is unconstrained in the remaining faces. The in-plane dimensions of the plate are 10 cm by 10 cm, and the plate is 2 cm thick. In Figure 5.1, the spherical projectile impacts the plate at a speed of 210 m/s. Figure 5.2 presents a typical final mesh of the plate, after the rebound of the impactor. Most of the calculations presented in the remainder of the section attained that degree of refinement. The error estimation captured successfully the impact zone. The mesh density is very high at the central part of the plate. The initial mesh contains approximately 1000 nodes and in some of the presented calculations the final meshes contain 20000 nodes. This degree of refinement allows us to resolve optimally the mechanical fields in the impact area which is the region

of interest, in the plate. Adaptive meshing was also extensively used to remove sliver elements that appeared at the impact area. The final mesh is not symmetric as the asymmetry of the intial mesh was aggravated by the adopted bisection method. Mesh refinement was not applied on the projectile as the quality of its elements remains high throughout the calculations. In its initial configuration, the impactor contains 42 elements of approximate volume of 10 mm^3.

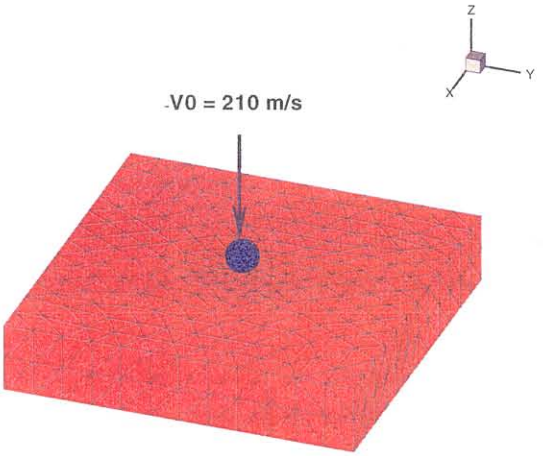

Figure 5.1: Initial mesh

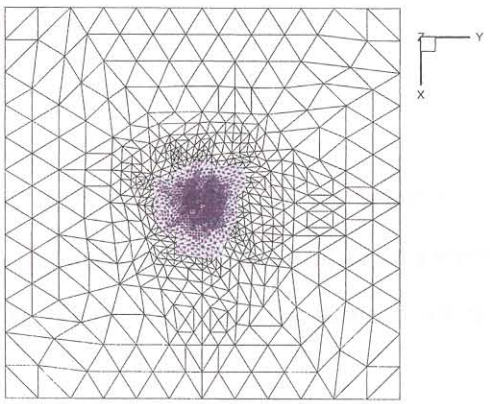

Figure 5.2: Top view of a final mesh

	SI
ρ, mass density	7800 kg/m^3
E, Young's modulus	202 GPa
ν, Poisson's ratio	0.3
σ_y, initial yield stress	600. MPa
ϵ_0^p, reference plastic strain	0.0001
$\dot{\epsilon}_0^p$, reference plastic strain rate	1 s^{-1}
m, rate sensitivity exponent	5
n, hardening exponent	10
c, heat capacity	477 J/kg K
k, conductivity	38 W/m K
T_{ref}	293. K
T_{melt}	1700. K
α, softening exponent	1.
μ, friction coefficient	0.01
β, Taylor-Quinney parameter	0.9

Table 5.1: Material parameters for mild-steel

A natural question that arises is the effect of adaptive meshing on the mechanical results. The first issue that needs to be addressed is mesh sensitivity. A test was carried out with the number of elements contained in the steel projectile ranging from 42 to 650. The impact speed of the projectile was 100 m/s. The average velocity vector of the projectile is computed so as to match its total linear momentum which leads to the expression

$$\boldsymbol{V} = \frac{\sum_{n=1}^{nodes} m_n \boldsymbol{V}_n}{\sum_{n=1}^{nodes} m_n} \tag{5.3}$$

where m_n is the mass of node n and $\boldsymbol{V}_n$ is its velocity. The rebound speeds of the spherical projectile as a function of the number of elements in the projectile are summarized in Figure 5.3. They vary slightly around 78 m/s and are clearly mesh independent.

A second issue which is worth addressing is the coupling of adaptive meshing with the contact algorithm in the presence of non-smooth surfaces. The condition of non penetrability of the contact could be respected before remeshing but violated momentarily when new nodes are introduced. The contact algorithm applies in that

case instantaneous accelerations to impose the non-penetrability condition. This has a slight effect on the numerical results which is most visible at high impact speeds as shown in Figure 5.4 in which the velocity response of the projectile is plotted as a function of time. The striking velocity of the impactor is 2000 m/s. In Fig 5.4, the horizontal components, V_x and V_y, of the velocity vector are negligible. The vertical component, V_z, experiences some jumps (dashed lines in the figure) and some oscillations (zone 1 in Fig 5.4). These jumps correspond to the introduction and removal of nodes via the remeshing procedure. The contact algorithm reinforces the non penetrability condition at those stages. Overall, these jumps have a limited impact on the finite-element solution. Up to $3\mu s$ the velocity of the projectile decays linearly. After that time, the decrease is asymptotic. It is also noteworthy that once a higher degree of refinement is achieved (beginning of zone 2 in Fig 5.4), the oscillations created by the contact stopped. Mesh adaption does not seem to be an issue regarding the validity of the numerical results.

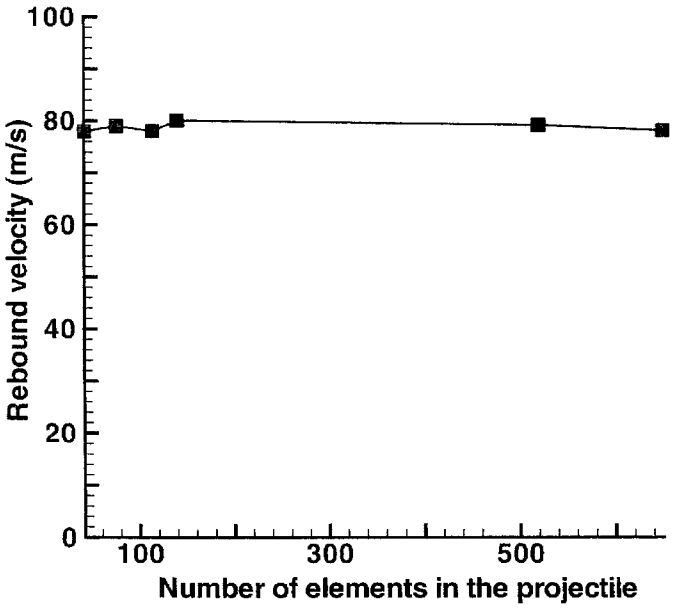

Figure 5.3: Mesh sensitivity study with an impact velocity of 100 m/s

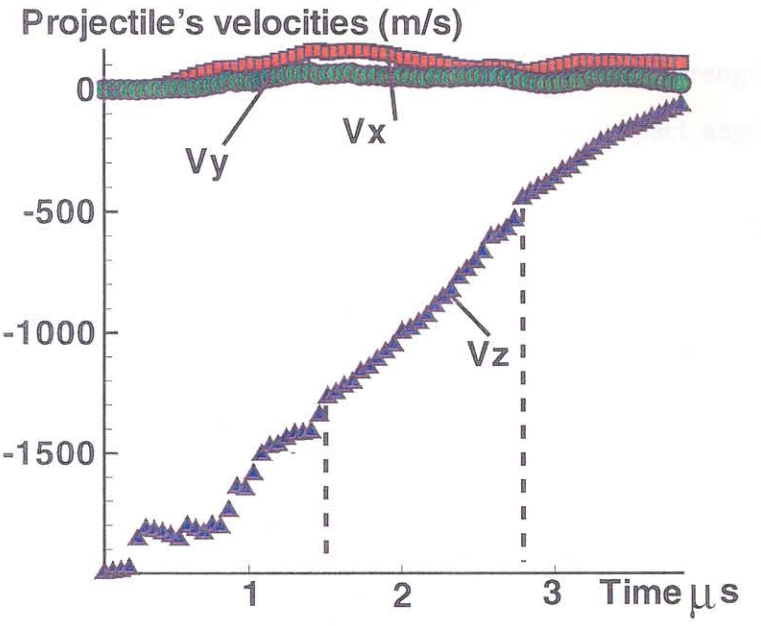

Figure 5.4: Velocity response of the projectile versus time

5.4 Comparison with Hutchings's experiments

Now that we explained and justified the methodology, we carry out parametric studies to get valuable insight into the mechanics of impact and erosion. Ultimately, the idea is to use our code as a tool to confirm or reject models. We will base our comparison on Hutchings's experiments [49]. In one specific series of experiments, Hutchings took photographs of 9.5 mm hard-steel spherical proojectiles hitting a mild-steel plate at speeds ranging from 0 to 310 m/s and impact angles from 0 to 90°. Hutchings analyzed the craters which had formed upon impact and the velocity profiles of the rebounding ball. We will focus our comparisons on these experiments.

Two sets of tests are carried out. In Section 5.4.1 we compare the obtained numerical results to the available experimental data at a given impact speed for a wide range of impact angles. In Section 5.4.2, comparisons are carried out at a fixed impact angle at varying impact speeds.

5.4.1 Variation of the impact angle

The first validation test consists of a 9.5 mm diameter high-strength steel ball impacting a mild-steel plate at a velocity of 210 m/s. The impact angle ranges from 0 to 90°.

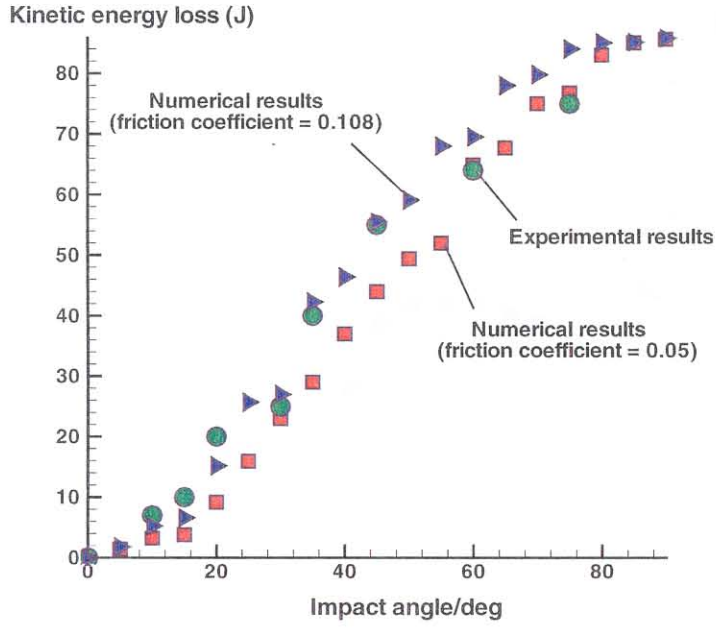

Figure 5.5: Kinetic energy loss versus impact angle

A comparison between the experimental results of Hutchings and our computational results is given in Figure 5.5. The kinetic energy loss in the projectile is given as a function of the impact angle. An impact angle of 0° implies that there is no penetration; therefore, the kinetic energy loss is 0. The kinetic energy loss is maximum at 90°, which is normal penetration. The right profile is captured by fitting the friction coefficient. Hutchings reports [49] an estimated friction coefficient of 0.05. The best fitted value used in the calculations is 0.108. This coefficient is fed into the Coulomb friction law. Using this value, the numerical results are in good agreement with the experimental data. At impact angles above 60°, the numerical results are slightly

higher than the experimental data. One feature that is captured by the simulation is the inflection point in the curve at 45°. A more relevant comment than simply noting that our estimation of the friction coefficient is higher than the experimental one, is that the friction coefficient has a clear effect on the mechanical response. If the friction coefficient is doubled, the kinetic energy loss increases at least 20% up to angles of 70°. At normal penetration, friction plays a very limited role. The loss of kinetic energy comes almost solely from plastic deformation. However, for impact angles away from normal penetration, developing numerical or analytical models without taking into account friction seems doubtful.

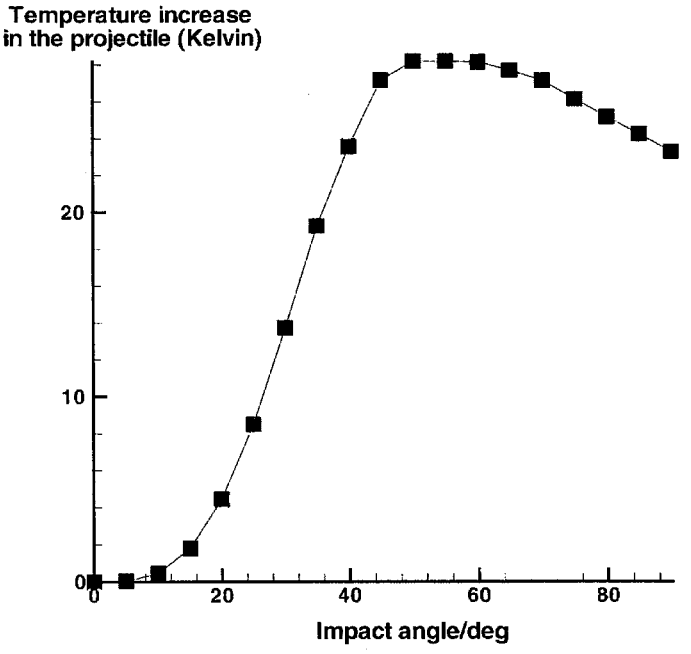

Figure 5.6: Temperature elevation versus impact angle

In Figure 5.6, we give the maximum temperature elevation in the projectile as a function of the impact angle. Interestingly enough, the maximum of the curve is not reached at normal incidence but at approximately 45°, which illustrates once more the importance of taking the friction coefficient into account in impact simulations. The calculations also revealed, in agreement with Hutchings [49], that the rotational

kinetic energy can be neglected. For the remainder of the calculations, we keep the material parameters and the fitted friction coefficient constant. There is no further fitting of the parameters.

5.4.2 Variation of the impact velocity

The second test consists of the same high-strength steel ball impacting a mild-steel plate. This time, however, the angle of attack is fixed at 30° and the impact velocity varies from 141 m/s to 310 m/s. The experimental photographs [49] are shown in Figure 5.7.

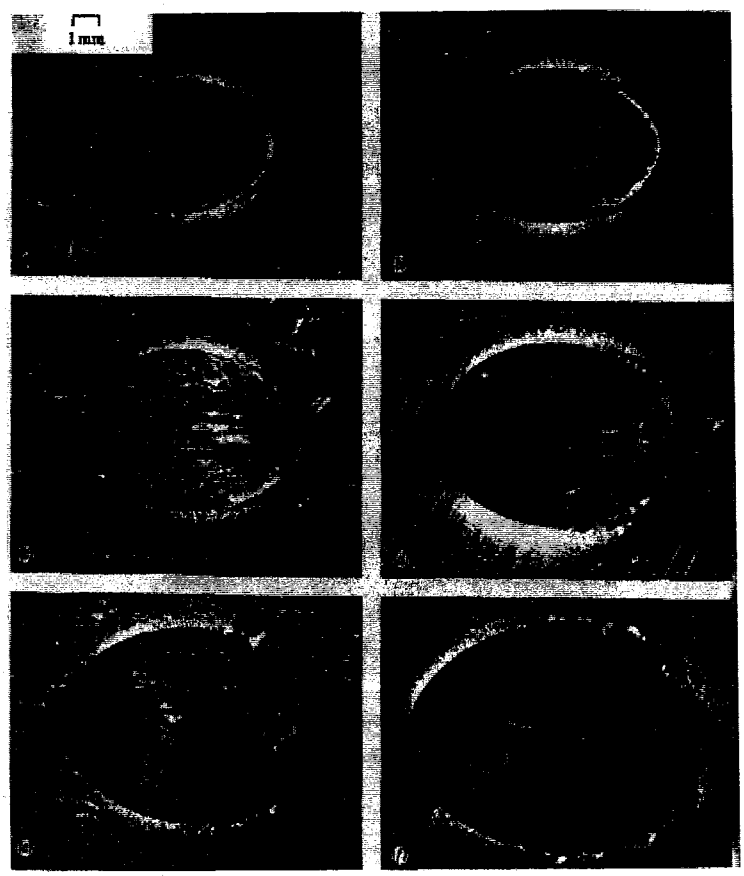

Figure 5.7: Hutchings's experimental results [49]; the angle of attack is 30° (left to right); the impact velocities are from left to right and top to bottom: 141 m/s, 174 m/s, 178 m/s, 218 m/s, 262 m/s, 310 m/s

The test aims at comparing the dimensions of the crater left after impact on the upper face of the plate. This crater is the product of irreversible plastic deformation. We delimited the numerical plastic zones using the contour plots of the effective plastic strain. In Figure 5.8 is shown the effective plastic strain contour plot of the impacted zone. We added on top of the figure the elliptical shape of the crater obtained experimentally. In Figure 5.9, we plot crater size versus impact speed. There is a very good agreement between experimental and numerical results. The high degree of refinement within the impacted zone enabled the correct computation of the elliptical shape of the damaged zone. Within the chosen range of impact velocities, crater size seems to increase linearly with the velocity at impact, as shown in Figure 5.9.

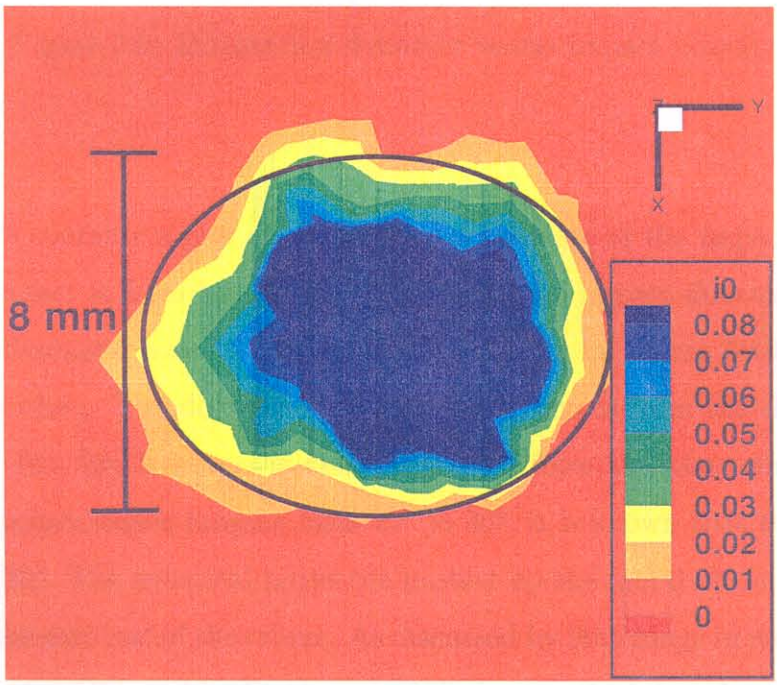

Figure 5.8: Effective plastic strain contour plot of the impacted zone; the impact velocity is 310 m/s; the ellipse represents the shape of the experimental crater

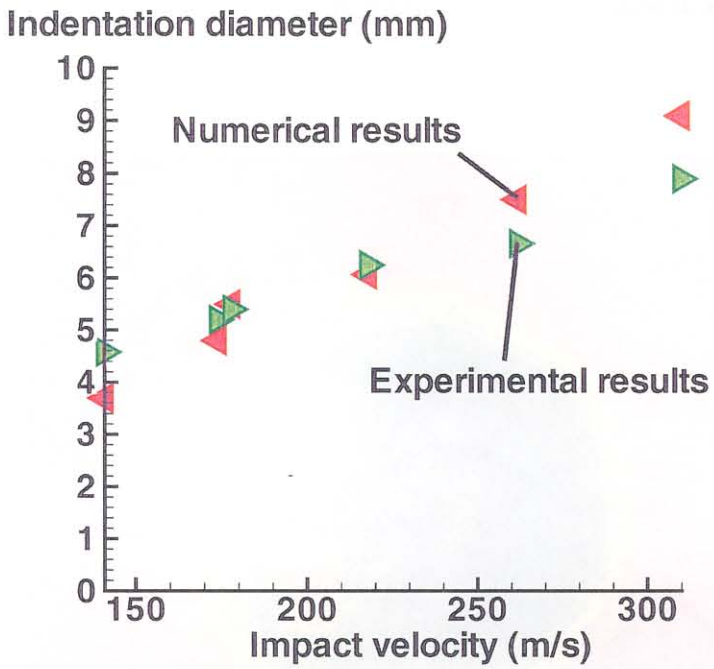

Figure 5.9: Indentation diameter versus impact velocity

Figure 5.10 contains a plot of the vertical coordinate of the impacted area. The direction of impact is from left to right. Following the impact direction, we observe the elliptical damaged zone, followed by a lip (in red in Figure 5.10) and again a depression (in blue). The depression behind the lip comes from the elastic response of the plate. The lip, however, is being extracted from the plate due to frictional contact. At impact angles ranging from 20° to 30°, it is known that the erosion rate is maximum [30]. The spherical projectile pushed up the metal above the surface to form a lip at the exit end of the crater. As discussed by Hutchings in its description of erosion by plowing [49], and by Field *et al.* [30], the lip, which is deforming plastically, may become detached at high enough velocities. The lip is a location where shear band instabilities develop. Field *et al.* [30], noted that adiabatic shear occurs if the sphere is sufficiently large and the impact speed is sufficiently high. Since the shear bands are preferred sites for material failure, they aid the detachment of the lip. The success of the adaptive meshing method in capturing fine features is noteworthy. Its

ability to predict the lips in front of the damaged zones makes it an excellent tool to obtain estimates on impact erosion.

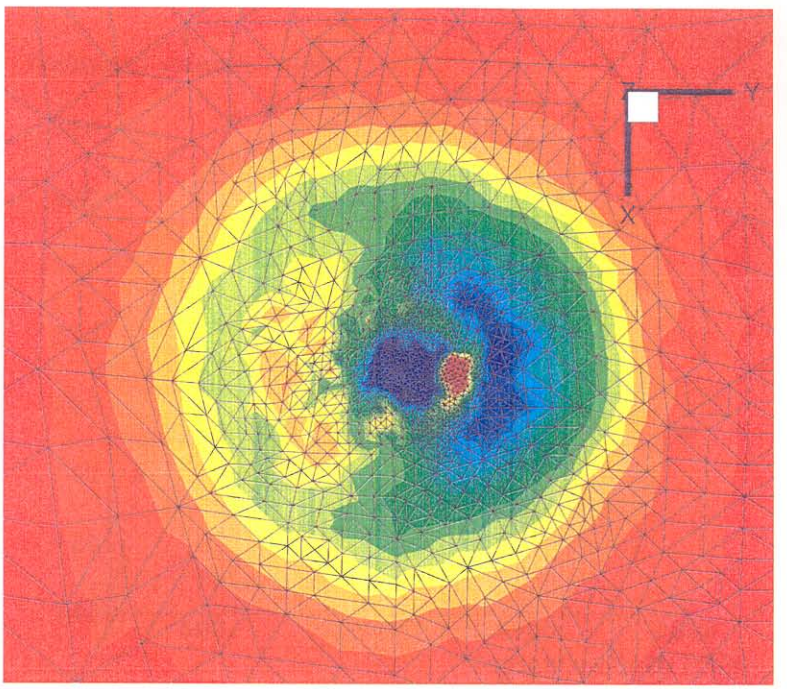

Figure 5.10: Vertical coordinate contour plot

5.5 High impact speeds

We now conduct further calculations to verify the validity of the proposed method at higher impact speeds. We are still using the same numerical model. We will restrict our calculations to normal impact. We seek to determine the range of impact velocities in which the plastic deformation of the projectile can be safely neglected. This in turn will serve in determining the domain of validity of a rigid sphere model for erosion by plowing. Field *et al.* [30] divided solid particle impacts into three different regimes corresponding to different damage numbers D, where

$$D = \rho V^2 / Y \tag{5.4}$$

Here, V is the impact velocity and ρ and Y are the density and the yield stress of the target material respectively.

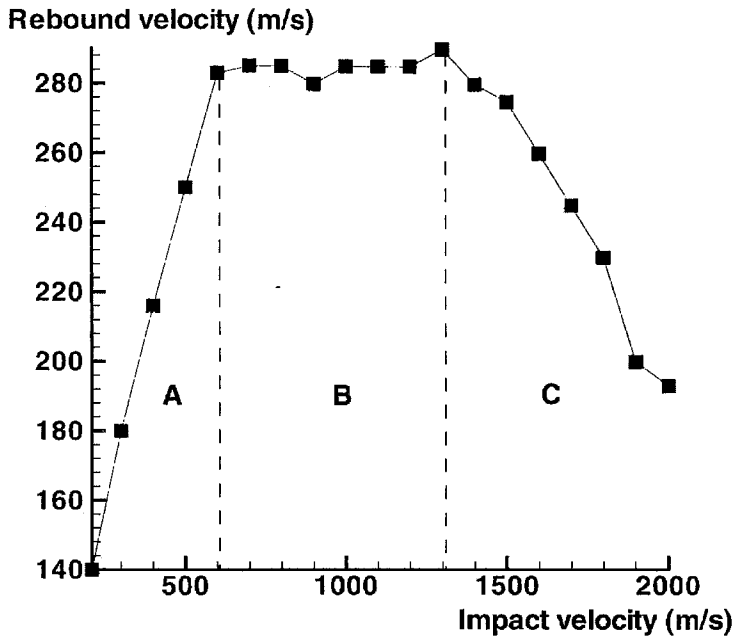

Figure 5.11: Rebound velocity versus impact velocity

For velocities less than 1 m/s on steels ($D < 10^{-5}$), there is a very limited plastic flow and the behavior of the target and projectile is mainly elastic. The second regime [30] corresponds to velocities on steel in the range 5 to 500 m/s ($D < 1$) and may be termed the sub-ordnance range. Impacts in this range result in plastic deformation of the target (see Figure 5.8). However, in our numerical model, the projectile behaves mainly elastically. The third regime is called the hypervelocity regime with velocities from 500 m/s to 3000 m/s. In our calculations within this regime, the projectile (together with the plate) experiences drastic plastic flow. In Figure 5.11, we are plotting the rebound velocity of the spherical projectile versus its impact velocity. Three distinct zones appear; they are denoted by A, B and C in the figure. In zone A, with impact velocities ranging from 210 to 600 m/s, the response of the impactor is primarily elastic. The rebound velocity increases monotonically. The end of this zone

at 600 m/s corresponds roughly to the limitation of sub-ordnance regime. In zone B, the rebound velocity reaches a plateau. The response of the projectile is now mainly plastic. In zone C, starting at impact velocities of 1300 m/s, the thermal softening plays a leading role and the rebound speed of the impactor decreases drastically. Another explanation to the sudden decrease at high impact velocities of the rebound velocity comes from the fact that at high speeds, a deeper crater is produced. Then, due to the frictional contact, the plate opposes the impactor a longer distance, as the projectile is rebounding elastically. It is clear that above speeds of 600 m/s the plastic behavior of the projectile should be taken into account. Considering only plastic deformation in the target and neglecting thermal softening results in invalid numerical or analytical models.

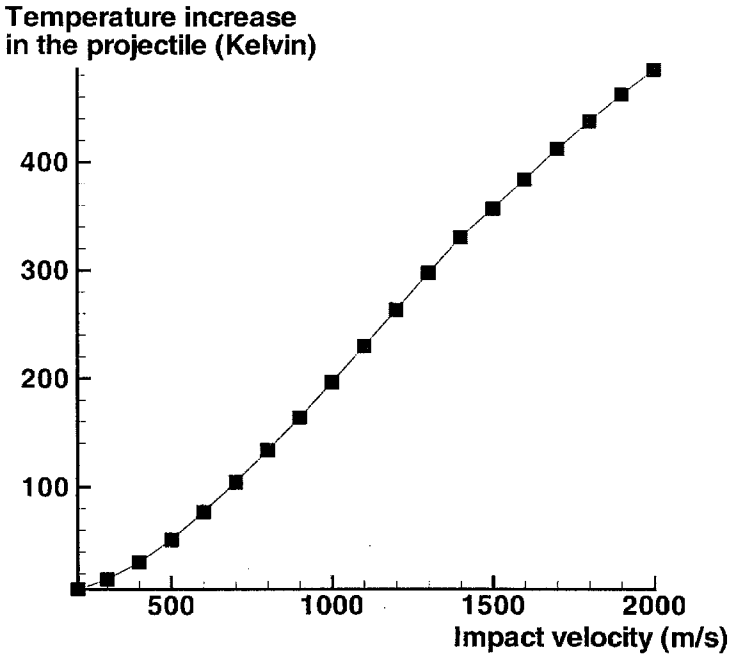

Figure 5.12: Temperature increase in the projectile versus impact velocity

The importance of thermal softening is highlighted in Figure 5.12 in which we plot the average temperature elevation in the sphere as a function of the impact speed. The melting temperature of our material is: $T_{melt} = 1700K$. Therefore, at

an impact speed of 2000 m/s, the average temperature reaches more than a third of this value and implies a reduction of the average yield stress to approximately 55% of its value without taking into account thermal effects (Equation 5.2). To further illustrate the importance of the irreversible plastic deformation in our model we plot, Figure 5.13, the deformed plate after a normal impact of 2000 m/s. We observe that the projectile left a 3 mm deep crater in the plate. Also, the spherical projectile before and after impact is represented in Figure 5.14. After impact the projectile remains in a "pancake shape". The maximum temperature increase is 1100 degrees Kelvin which implies considerable thermal softening (Figure 5.15). The thermal effects take place mainly at the impact zone and reduce the yield stress to 20% of the value it would reach with no thermal softening (Equation 5.2). At high velocities, considering a rigid sphere model for impact erosion will result in erroneous predictions. The deformed shape of the projectile has to be taken into account as it will affect the contact area and thus the degree of erosion in the plate.

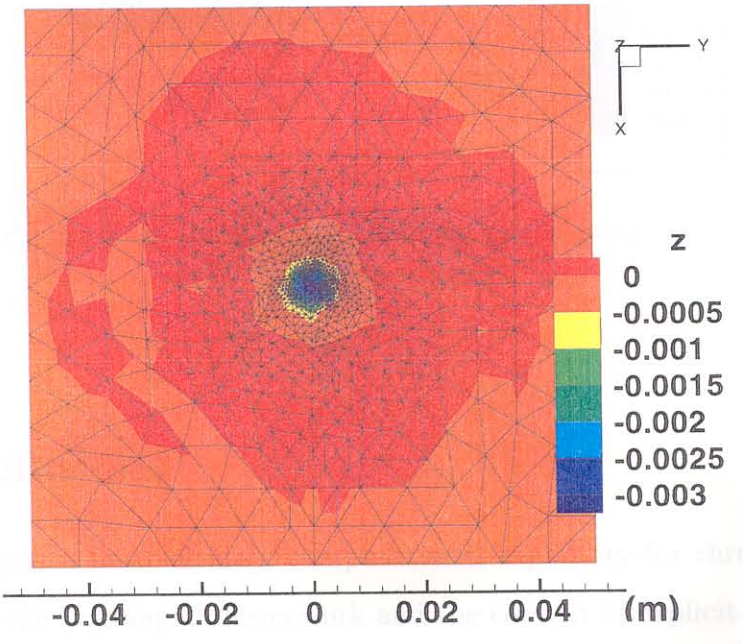

Figure 5.13: Contour plot of the vertical coordinate, impact velocity 2000 m/s

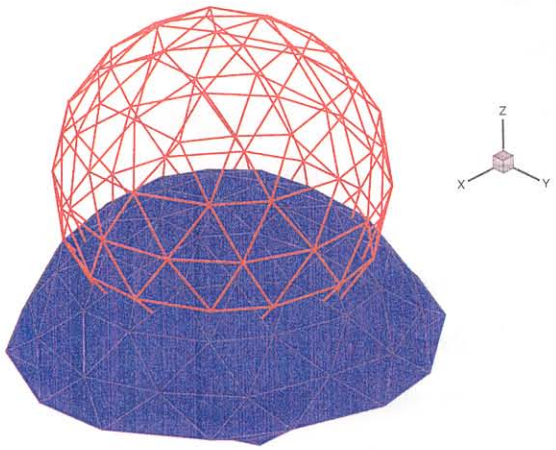

Figure 5.14: Projectile before and after impact

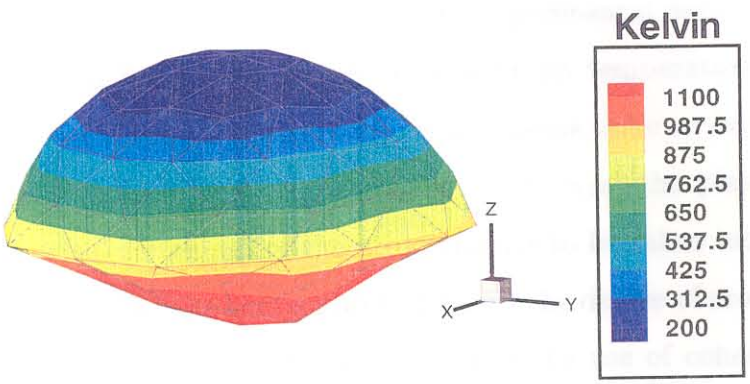

Figure 5.15: Temperature increase in the projectile

5.6 Conclusions

We have developed a finite-element computational capability for three-dimensional impact. Within the Lagrangian framework and the context of explicit dynamics, the components of the finite-element methodology are frictional contact, heat transfer, finite deformation plasticity and adaptive meshing. The success of the calculations is tightly linked to the use of three-dimensional adaptive meshing. Without this

key component, it would not have been possible to remove the distorted element at the impact zone. Adaptive meshing has been used extensively throughout the calculations and particularly at high impact speeds. The degree of refinement attained resolved fully the shear lip that appears when the projectile impacts the target at a low angle. At high speeds material erosion takes place mainly in the lip as shear bands are likely to develop in this location. The computational methodology was validated using Hutchings's experiment of hard steel spherical projectiles impacting steel plates. We compared the numerical loss of kinetic energy and crater sizes to experimental results. The agreement is good for a wide range of impact velocities and impact angles. More than a complete validation of the finite-element methodology, the calculations reveal that frictional contact has to be taken into account in every model (numerical or analytical), at all impact speeds and impact angles different from normal incidence. A better fitting with the experimental data would have been obtained by taking a friction coefficient dependent on temperature. Therefore, a constant friction coefficient throughout the impact seems to be an invalid hypothesis. We note also that at high impact speed (above 600 m/s) the plastic deformation (and possibly thermal softening) of the projectile has to be taken into account as its deformed shape will affect the contact area and thus the degree of erosion. A possible future development is to include within the model the use of cohesive elements to analyze the difference in behavior between ductile and brittle materials. The cohesive element model could be dependent on deformation.

Chapter 6 Application to wear

6.1 Introduction

The work presented in this chapter is concerned with the development, calibration and validation of a finite-element model of dry sliding wear in metals. We will, in that purpose, include within the already presented computational framework a surface evolution model. Sliding wear here refers to the type of wear generated by the sliding of one solid surface against another. Dry signifies that there is no lubrication.

We assume that the wear rate obeys Archard's law [3]. However, we generalize Archard's law by allowing the hardness of the soft material to be a function of temperature. This dependence provides a means of modeling the sharp transition in the wear rate which is observed to occur in some materials systems at a critical speed. Lancaster [56] speculated that this transition is linked to the level of oxidation of the metals in contact. At high speeds, which imply high temperatures, the oxidation rate increases and the protective oxide layer regenerates faster than it is removed by wear. Mixing of oxides with the primitive materials is also observed in the boundary layer. The proposed dependence of the hardness H on temperature T indirectly models the oxidation and other chemistry effects as well as the mixing which occurs in the softer material. In particular, the function $H(T)$ reflects the experimentally observed transition temperature T_c which separates the regimes of severe wear at low speeds to mild wear at high speeds.

The chapter is organized as follows. A brief description of the computational framework, with particular emphasis on surface effects and such mechanisms as strongly influence–or are influenced by–wear, is presented in Section 6.2. The model is then calibrated and validated against the experimental observations of Lancaster [42, 56]. Lancaster's experiments concern the wear of a 60-40 brass pin (C37700) set against a rotating high-strength steel disk. Lancaster reported the wear rate of the

brass pin for different speeds of rotation, along with a wealth of other observational evidence. The results of the validation tests are reported in Section 6.3. The ability of the full three-dimensional finite-element model to capture the transition from severe wear to mild wear beyond a critical speed, and to resolve fine three-dimensional features of the wear process such as leading-edge effects, is noteworthy.

6.2 Computational framework

6.2.1 Wear

We have chosen to use the conventional and well-established Archard's law of wear [3], which gives the wear rate w (height loss per unit time) through the relation:

$$w = \frac{K}{H} pv \tag{6.1}$$

where v is the sliding speed, p is the applied pressure, H is the hardness of the softer material (brass in the simulations reported subsequently), and K is the wear coefficient, a constant which ranges from 10^{-3} to 10^{-7} W/m K for typical materials systems.

The experimental observations of Lancaster (see [42, 56]) shed additional light on the variation of the various parameters in Archard's law (6.1). The experiments concern the wear of a brass pin set against a rotating steel cylinder. The experimental set up is shown in Figure 6.1, where C denotes the brass pin, B the steel cylinder and A is the rotating shaft. A pressure is applied at the top of the pin in order to press it against the rotating cylinder.

Of particular interest are the wear rates reported by Lancaster [42, 56] for different angular and sliding velocities. Thus, the four curves A, B, C, and D in Figure 6.2 refer to different values of applied pressure. It is evident from these curves that there is a marked transition in the wear rate at a sliding speed of approximately 8 m/s. Under 8 m/s a regime of severe wear is observed, whereas above 8 m/s the wear rate is considerably less. Lancaster further observed that the temperature at the

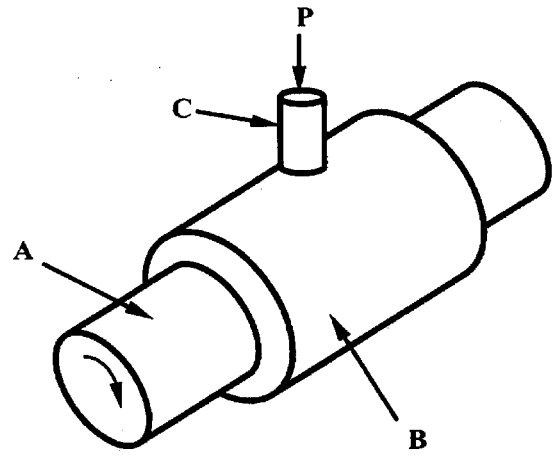

Figure 6.1: Schematic representation of the wear experiment of Lancaster ([42, 56])

interface for the four transition points (A, B, C, D) in Figure 6.2 was approximately 270°C. This suggests that the temperature at the transition is ostensibly constant and independent of the applied pressure and the sliding speed.

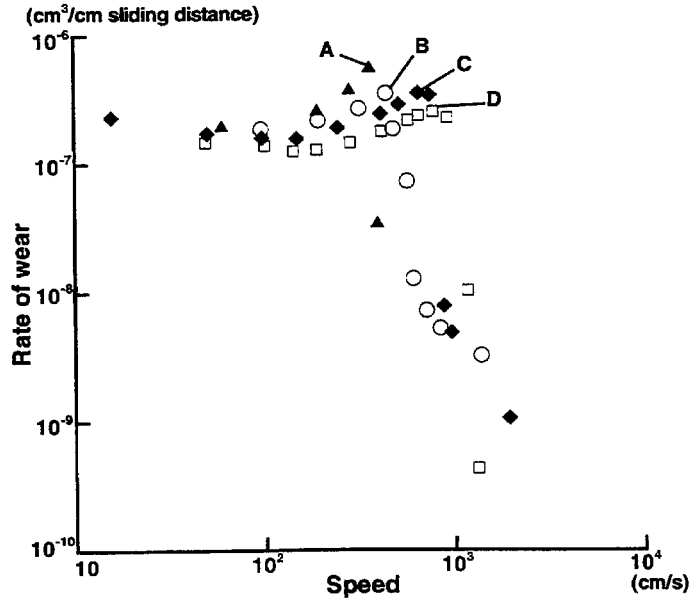

Figure 6.2: Wear rate versus speed ([42, 56])

Lancaster speculated that the transition from severe to mild wear is linked to the level of oxidation of the metals in contact. At high speeds, which imply high

temperatures, the oxidation rate increases. The protective oxide layer regenerates faster than it is removed by wear. Figure 6.3 (reproduced from [56]) illustrates the complexity of the chemistry involved in wear. The top figure shows a photograph of a tapered-section of the brass pin, and the graph below is a plot of the hardness of the brass against depth from the contact surface. As may be seen from this plot, the hardness decreases with depth. Close to the interface, the hardness is high and comparable in magnitude to the hardness of steel. The dashed lines separate the different observable layers of the brass. However, it should be carefully noted that these layers are not made of pure brass. Indeed, the layer immediately adjacent to the contact region is a complex mixture of oxides, steel, and brass.

Evidently, the transition from severe to mild wear is an important phenomenon which requires careful modeling. We propose to account for the chemistry and mixing attendant to wear by the simple device of letting the hardness H of the soft material in Archard's law, Equation 6.1, be a suitable function of temperature. The dependence of the hardness on temperature indirectly models the oxidation and other chemistry effects, as well as the mixing which occurs in the softer material. In particular, the function $H(T)$ should reflect the existence of a transition temperature T_c, the steady decrease in the hardness (increase in the wear rate) up to T_c, and the sudden and sharp increase in the hardness (decrease in the wear rate) for temperatures higher than T_c. The calibration of the function $H(T)$ for the brass/steel system tested by Lancaster is described in detail in Section 6.3.2.

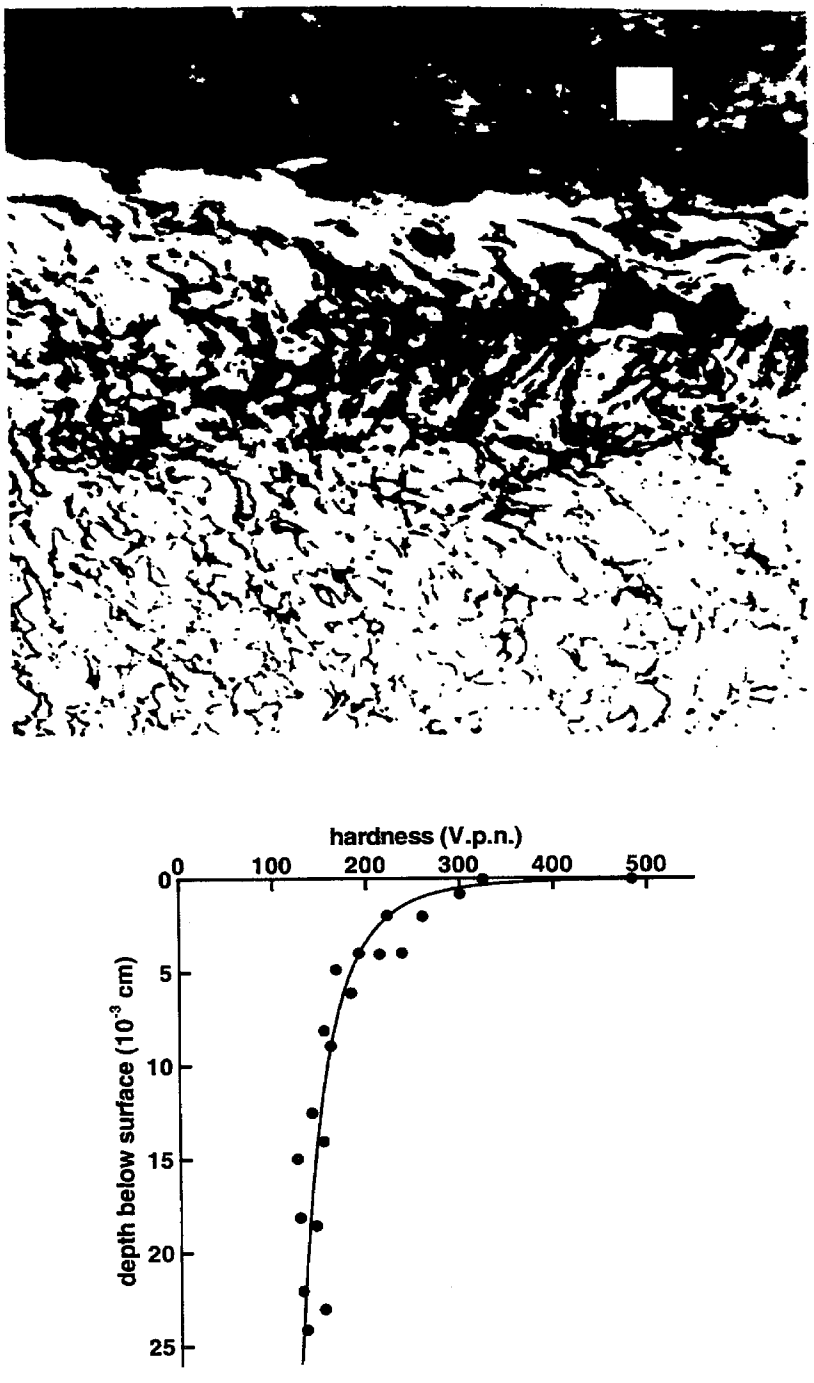

Figure 6.3: Hardness variation in the brass (from [56])

6.2.2 Contact and friction

Contact and friction must carefully be accounted for in a wear simulation. The contact/friction algorithm which was described in Chapter 2 enforces the impenetrability constraint, and determines the frictional forces and the extent of frictional dissipation, which is in turn fed into the energy equation as heat. An additional byproduct of the contact algorithm is the contact pressure required to evaluate Archard's law and to compute the wear rate. The contact pressure is computed simply node per node as N/A, where A in a tributary area of the node. This contact pressure is used to evaluate Archard's law (Equation 6.1). The heat generated by friction is also computed as the work done by the relative sliding velocities against the frictional forces over a time step.

6.2.3 Thermal effects

Wear involves a number of strongly interacting mechanical and thermal processes. In the calculations, we account for thermomechanical coupling and the interaction between wear, friction, temperature and plasticity. The heat produced by friction and plastic work acts as a source for the thermal problem. The constitutive model chosen is described in Section 5.2. The corresponding thermal softening and the mass loss due to wear in turn influence the mechanical problem. Finally, wear is a function of the sliding velocity, contact pressure, and hardness. Since, in addition, the hardness is a function of the temperature, wear rates are themselves tightly coupled to the mechanical and thermal fields.

The heat h is apportioned to the bodies in contact in accordance with the Equations 2.54 and 2.55 [36]; see Section 2.4 in Chapter 2 for more details. The heat flux q across the interface between the bodies in contact also needs to be carefully quantified. Following Wriggers and Miehe [107] we write:

$$q = h_c \left(\frac{p}{H}\right)^{\epsilon} (T_1 - T_2) \tag{6.2}$$

where H is the hardness of the softer material, h_c and ϵ are interfacial parameters,

and T_1 and T_2 are the temperatures of the bodies in contact. The term $(p/H)^{\epsilon}$ is an estimate of the true area of contact. Thus, an increase in p is assumed to result in a decrease in the number of air-filled gaps, which act as insulators, and, correspondingly, in an increase in the contact area, with the attendant increase in the thermal conductivity across the interface. Figure 6.4 summarizes the different heat exchange.

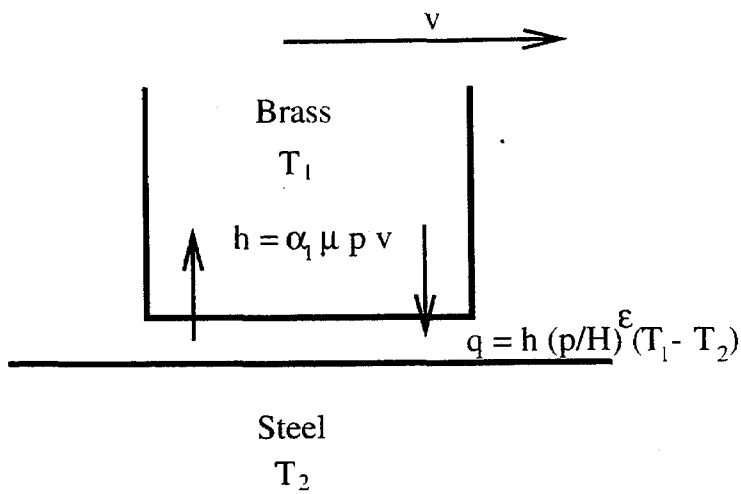

Figure 6.4: Interfacial thermal problem

The duration of a typical wear experiment is 40 minutes to an hour. The total sliding distance ranges from a few hundred meters to several kilometers. Due to these long durations, the initial short transient may be safely neglected, and steady-state conditions may be assumed to prevail throughout the calculation to a good approximation. Under steady-state conditions the heat supply to both bodies, h_1, h_2 and q is independent of time. The corresponding temperature profiles T_1 and T_2 in the bodies may be estimated by an application of Jaeger's formula (see [50]) for a moving line source on a semi-infinite body. Once determined, the steady-state temperature profiles are set as initial condition for the calculation.

6.3 Finite-element validation

The experimental observations of Lancaster [42, 56] provide a convenient basis for the calibration and validation of the finite-element wear model described in the foregoing. The experiments concern the wear of a 60-40 brass pin (C37700) set against a rotating high-strength steel disk.

6.3.1 Problem definition

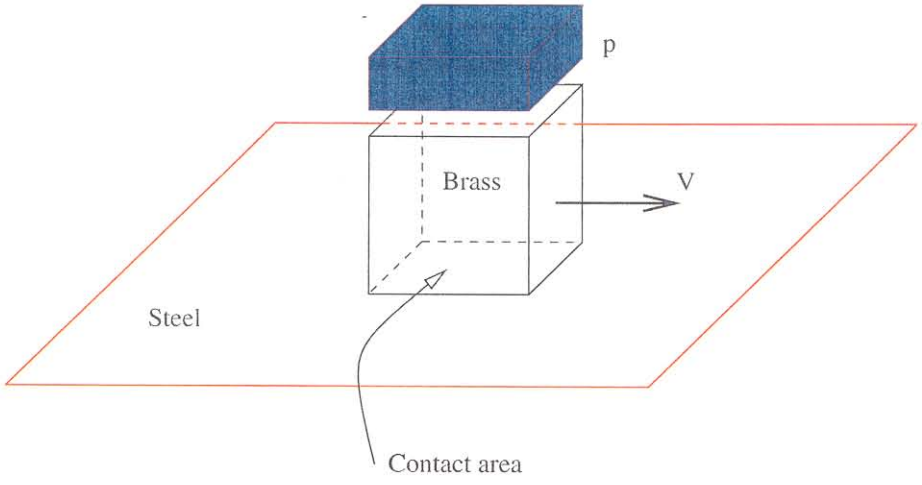

Figure 6.5: Geometry of finite-element model; the brass pin has a velocity V

The geometry of the finite-element model used in calculations is shown in Figure 6.5. For simplicity we assume a square cross section for the pin. The area of this cross section, which equals 1.6 mm^2, matches exactly the area of the cylindrical pin used by Lancaster in test C (see Figure 6.2). A small square coupon of the rotating cylinder is also considered in the analysis. The lateral dimensions and thickness of this coupon are four and two times the side of the pin, respectively. The steel plate is held stationary while the brass moves at a velocity V ranging from 0.2 to 20 m/s along the length of the plate. V is applied to the top surface of the pin, and, in addition an initial velocity of the same value is applied to the pin. When the pin reaches the boundary of the steel coupon, the speed of the coupon is reversed, with the result that the pin moves back and forth repeatedly over the plate surface. The applied

E	210 10^9 Pa
ν	0.3
k	20 W/m K
c	486 J/kg K
ρ	8670 kg/m^3

Table 1. H.S. Steel

E	105 10^9 Pa
ν	0.37
σ_y	1.4 10^8 Pa
ϵ_0^p	0.0005
$\dot{\epsilon}_0^p$	1.
m	100.
n	3.2
T_{ref}	293. K
T_{melt}	1168. K
α	1.
k	120 W/m K
c	380 J/kg K
ρ	8440 kg/m^3

Table 2. 60-40 Brass

contact pressure is $p = 1.82 \times 10^5$ Pa. In the application of the contact algorithm, the brass pin is taken as slave and the steel plate as master. For simplicity, we neglect heat losses in the surfaces in contact with air such as may be caused by radiation or convection.

The material parameters used in the calculations are collected in Table 1 and Table 2. The friction coefficient is taken to be $\mu = 0.3$.

6.3.2 Calibration of the model

An upper bound for the steady state temperature in the steel may be obtained by directing all the heat generated by friction into the steel plate, i.e., by setting $h_2 = h = \mu pv$. This upper bound gives a negligible temperature rise of approximately 2°C. The temperature elevation in the steel may therefore be safely neglected, and T_2 may be kept equal to the initial temperature $T_{initial} = 20°C$ to a good approximation. The implication of this estimate is that, under the conditions of the analysis, the contact area moves so fast that the steel does not have sufficient time to heat up appreciably.

At the steady state,

$$h_1 = q \tag{6.3}$$

$$\alpha_1 \mu pv = h_c \left(\frac{p}{H}\right)^{\epsilon} (T_1 - T_2) \tag{6.4}$$

The interfacial parameters h_c and ϵ which determine the heat flux q from the brass to the steel (Equation 6.2) may then be estimated simply by fitting the four transition points, A, B, C, D of Figure 6.2 to Equation 6.4. Lancaster [42, 56] reported the temperature at those points to be 270°C. The pressure, velocity, hardness, and steel temperature T_2 are also known. We obtained $h_c = 0.4 \times 10^5 \mathrm{W/km^2}$ and $\epsilon = 0.68$.

Once h_c and ϵ are known, we may obtain an estimate of the temperature in the brass at the steady state for any velocity. These estimates were used to properly scale the brass hardness coefficient. Table 3 contains the values of the wear coefficient over the brass hardness coefficient for the different chosen velocities. The term K/H is part of Archard's law and thus was tabulated in the code as a function of temperature. However, the function $H(T)$ may be constructed by fixing the wear coefficient K.

6.3.3 Numerical results

Nine calculations at speeds ranging from 0.2 to 20 m/s were carried out. The physical time duration simulated in each calculation is 1 ms. A typical calculated mass-

V [m/s]	T [K]	K/H [Pa^{-1}]
0.2	300	$7.3\ 10^{-13}$
0.5	310	$5.78\ 10^{-13}$
1	327	$5.1\ 10^{-13}$
2.5	378	$6.47\ 10^{-13}$
5	462	$1.\ 10^{-12}$
8	564	$1.19\ 10^{-12}$
9	598	$3.4\ 10^{-14}$
10	632	$1.7\ 10^{-14}$
20	972	$3.4\ 10^{-15}$

Table 3. 60-40 Brass; Wear coefficient over hardness coefficient

loss curve is shown in Figure 6.6(a). The slope of this curve gives the wear rate. Despite the modest net mass loss, a careful examination of Figure 6.6(a) reveals some noteworthy features. Firstly, the oscillations of the curve at the beginning of the simulation may be noted. These oscillations arise from inertial effects due to the instantaneous application of pressure to the brass pin. The wear rate stabilizes and shows a smooth variation as soon as the waves in the brass are damped out. One effect of the initial inertial effects is to increase the wear rate by approximately 20% relative to the subsequent steady wear rate, which is ostensibly constant.

Figure 6.6(b) plots the steady wear rate *vs.* speed for the nine calculations conducted. As may be seen from this figure, the transition from severe wear to mild wear is well captured by the model. However, the calculated wear rates are systematically 10% higher than experiment. The offset comes from three-dimensional effects not accounted for in the calibration of the model. Thus, Figure 6.7 shows contour levels of the wear rate for two different speeds: 1 m/s, leading to severe wear; and 10 m/s, corresponding to mild wear. A marked leading-edge effect is observed in both cases. Thus, the pressure is higher at the leading edge of the brass than the average contact pressure, which results in higher wear rates and mass loss. Indeed, the wear rate on the leading edge may be up to 500 times larger than on the trailing edge. The ability of the full three-dimensional finite-element model to resolve these fine features of the wear process is particularly noteworthy.

It should also be noted that the calibration of the function $H(T)$ can be further refined–and the match between simulation and observation improved–by interaction based on the results of the calculations. However, this avenue will not be pursued here.

6.4 Conclusions

A finite-element model of dry sliding wear in metals has been presented. The model is formulated within a Lagrangian framework capable of accounting for large plastic deformations and history-dependent material behavior. Other features of the numerical model include: surface evolution due to wear; finite-deformation J_2 thermoplasticity; heat generation and diffusion in the bulk; non-equilibrium heat-transfer across the contact interface; and frictional contact.

Particular attention has been devoted to a generalization of Archard's law in which the hardness of the soft material is allowed to be a function of temperature. Lancaster [56] speculated that the transition from severe to mild wear is linked to the level of oxidation of the metals in contact. At high speeds, which imply high temperatures, the oxidation rate increases and the protective oxide layer regenerates faster than it is removed by wear. Mixing of oxides with the primitive materials is also observed in the boundary layer. The proposed dependence of the hardness of temperature indirectly models the oxidation and other chemistry effects as well as the mixing which occurs in the softer material. In particular, the function $H(T)$ reflects the experimentally observed transition temperature T_c which separates the regimes of severe wear at low speeds to mild wear at high speeds.

The model has been validated against the experimental test of Lancaster [56], consisting of a brass pin rubbing against a rotating steel plate. The transition from severe wear to mild wear beyond a critical speed is well captured by the model. The calculations additionally reveal marked leading-edge effects. In particular, the pressure is higher at the leading edge of the brass than the average contact pressure, which results in higher wear rates and mass losses. Indeed, the wear rate on the

leading edge may be up to 500 times larger than on the trailing edge. The ability of the full three-dimensional finite-element model to resolve these fine features of the wear process is particularly noteworthy.

Interestingly, the observed transition sliding velocity falls within the range of tool/stock sliding velocities characteristic of high-speed machining. The existence of a transition velocity in the wear rate may therefore be exploited by the design of high-speed machining operations for minimum tool wear and best surface finish.

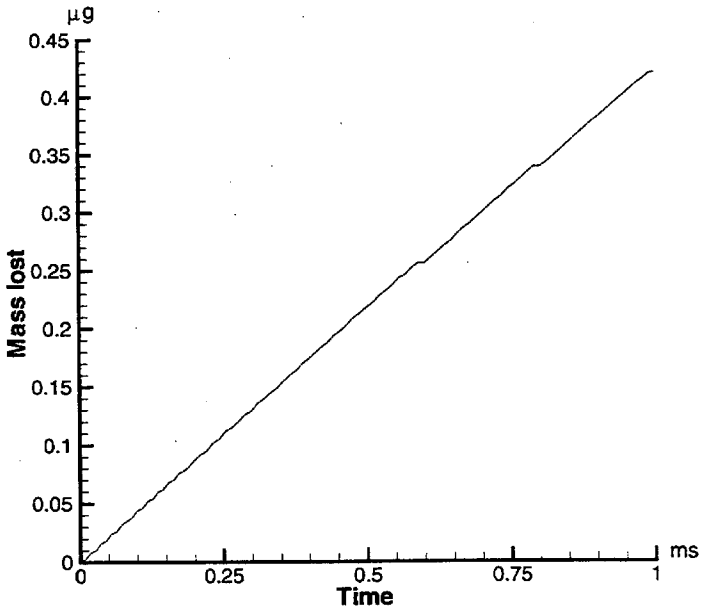

(a) Mass loss of the brass pin *vs.* time

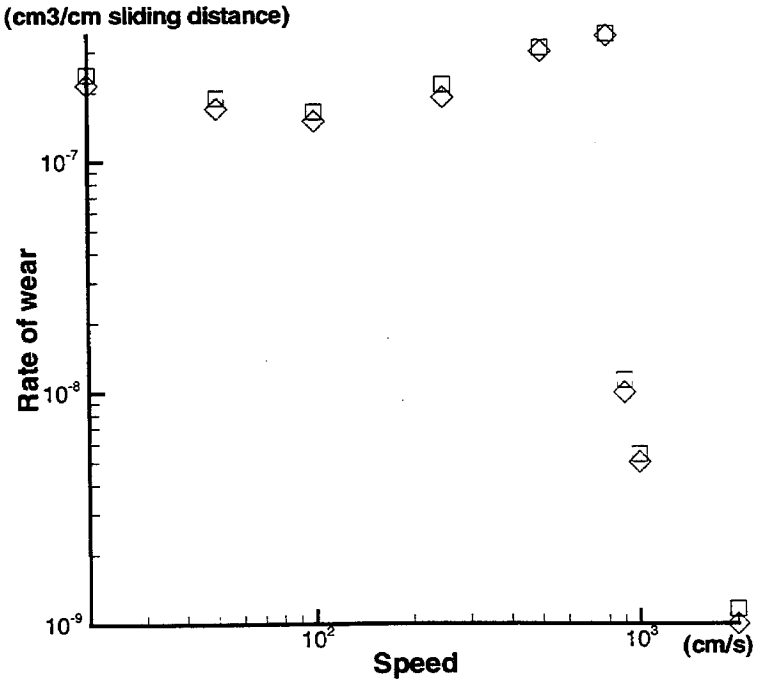

(b) wear rate versus speed: Simulation (square) *vs.* experiment (diamond)

Figure 6.6: Numerical results

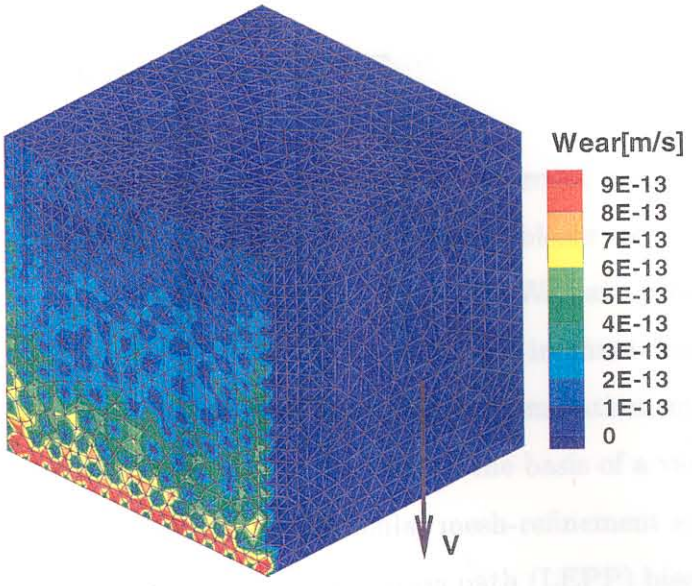

(a) $v = 1$ m/s, severe wear

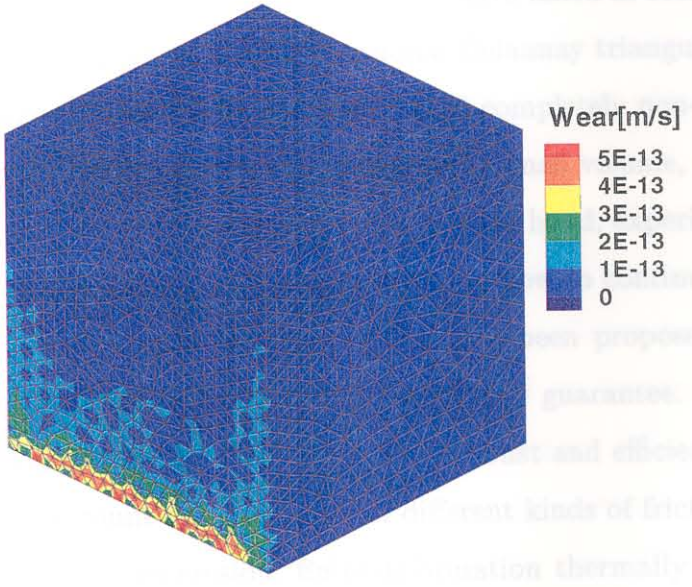

(b) $v = 10$ m/s, mild wear

Figure 6.7: Wear rate contour plot showing increased wear rates at the leading edge of the brass pin

Chapter 7 Conclusions

The intent of this dissertation was to propose a finite-element methodology that enables a finite-element analysis of complex mechanical problems seen in industrial and military applications, i.e., impact and erosion of metals. We have presented a general framework for adaptive mesh refinement and coarsening in three-dimensional finite-deformation dynamic elasto-plastic problems. In our formulation, mesh adaption is driven by *a posteriori* global error bounds derived on the basis of a variational formulation of the incremental problem. The particular mesh-refinement strategy adopted is an extension of Rivara's longest-edge propagation path (LEPP) bisection algorithm [91, 89, 90] to three dimensions. Our innovative strategy for mesh coarsening, or unrefinement, is based on the elimination of elements by edge collapse. The bisection algorithm together with the coarsening method define a robust, elegant, and efficient alternative to other remeshing methods that in fact have failed in some cases to provide a viable mesh. For instance, three-dimensional Delaunay triangulations offer no guarantees regarding the mesh quality and disregard completely non-convex boundaries. They often generate tetrahedra with vanishingly small volume, also referred to as *slivers* [16]. The advancing front method, on the other hand, experiences problems of mesh closure whenever the algorithm cannot decide how to continue the advancement of the front. Many experience-based rules have been proposed to solve this problem, but to our knowledge, none of them offers any guarantee. The remaining components of our computational framework are a robust and efficient contact algorithm that takes into account the possibility of different kinds of friction models and surface evolution, i.e., due to erosion, finite-deformation thermally coupled elasto-plasticity, heat transfer, and error estimation. With each one of these components we are pushing the cutting edge of today's finite-element technology.

The validation of the method is not less relevant than the development itself. The above mentioned finite-element developments have been successfully applied to a

series of applications which are, in order: adiabatic shear banding, impact erosion, and wear. Each one of the applications requires the above described tools to be carried out successfully. While the adiabatic shear banding application provided a unique test to validate the general framework for adaptive meshing in the finite-deformation dynamic-elasto-plastic range, it also demonstrated the ability of the approach to adaptively resolve the increasingly fine structure of the shear band. In that sense, adaptive meshing is a viable tool for multiscale modeling. The second application carried out was an analysis of impact erosion. The numerical results have been validated by Hutchings's experiments of hard-steel spherical projectiles impacting mild-steel plates over a wide range of impact velocities and angles. More than purely a validation of a method, the obtained numerical results shed light on the necessity of paying extra attention to the fidelity of the friction model and the plastic behavior of the projectile. Finally, we concluded the thesis by showing how the contact algorithm can be coupled to a surface evolution problem, in our case an erosion law. For that purpose, we used the Archard law of wear to study the dry sliding wear regimes between a brass/steel metallic pair. All three applications simulated here have shown the success of our method in capturing fine features of the solution. The published experimental data surveyed also constitute a solid validation test of our finite-element numerical solutions.

While the computational framework presented here has withstood a number of stringent tests, several obvious extensions and improvements remain to be pursued. For instance, it would be highly desirable to have fully nonlinear error bounds, e.g., in energy, as opposed to the asymptotic bounds based on linearization presented here. Extensions of the variational framework accounting for full coupling between mechanics and heat conduction would also be a desirable improvement. Another computational development would be to incorporate the use of cohesive elements, which provide a natural framework to study fragmentation, and a contact algorithm able to locally conserve energy, since the numerical generation of energy is known to cause instabilities in high-speed contact problems. Then, we could extend our work to the three-dimensional analysis of brittle target materials, and adaptive meshing

would be primarily responsible for providing a rich enough set of fracture paths to be useful in analysis. It would also contribute to defining some set of multiscale effective models to average behavior over a set of elements, and therefore, relax the artificial friction caused by the "tetrahedral" shape of the fragments. The cohesive-element model should ideally be defined as a function of deformation. Last but not least, it would be of great interest to couple our finite-element methodology with an optimization method to study the best possible arrangement possible of components to minimize impact damage in a composite material.

Appendix A C-language data structures used in the bisection and edge-collapse algorithms

```
/*-----------------------------------------------------------*/

/* nodal data structure (used in the transfer) */
typedef struct nodaldata
{
  double *disp; /* displacements at the nodes */
  double *velo; /* velocities */
  double *acce; /* accelerations */
  int    *boun; /* boundary conditions */
  /* note that the forces are left to the user to determine /*
  /* after the remeshing function */
} NData;

/*-----------------------------------------------------------*/

/* element data, i.e., at the gauss points */
/* (used in the transfer) */
typedef struct elementdata
{
  int     elty; /* element type */
  int     elma; /* element material */
```

```
  double *stre; /* stresses */
  double *stra; /* strains */
  double *inte; /* internal variables */
}EData;

/*-----------------------------------------------------------*/

/* linked list of nodes */
typedef struct lnodes
{
  double x[3]; /* x,y,z coordinates of the node */
  int    num;  /* global number of the node */
               /* goes from 1 to total number of nodes */
  int    *face;/* face[i]=0 for node not on face i */
               /* face[i]=1 for node on face i */
               /* used to preserve the boundary information */
  int    nta;  /* number of adjacent tets to the node */
  struct ltets **adj;
               /* list of the adjacent tetrahedra */
  struct lnodes *LLink,*RLink;
               /* pointers to the right link and left link */
  NData ND;    /* nodal data, see above */
} LNodes;

LNodes *HEADNODE,*TAILNODE;
/* TAILNODE is the first node of the linked list */
/* HEADNODE is the last */

/*-----------------------------------------------------------*/
```

```
/* linked list of the tetrahedra */
/* it is constructed during the LEPP */
/* and destroyed after */
typedef struct listconform
{
  int tetnum;     /* global number of the tet */
 /* goes from 1 to elements */
  int edge;       /* longest edge number, goes from 1 to 6 */
  LNodes *nodea; /* points to 1st node of its longest edge */
  LNodes *nodeb; /* points to 2nd node of its longest edge */
  int sub;        /* 1 for subdivide the tet! */
                  /* 0 for wait to be subdivided! */
  struct listconform *LLink;
  struct listconform *RLink;
  struct ltets *Tet;
} ListConform;

ListConform *LC,*MC;

/*-------------------------------------------------------*/

/* linked list of all the tetrahedra of the mesh */
typedef struct ltets
{
  int tetnum; /* global number of the tetrahedron */
              /* between 1 and total number of elements */
  int sub;    /* when sub = 1, the tet is marked */
              /* by error estimation (will be subdivided) */
  LNodes *ix[10];
              /* points to the 10 nodes of the tetrahedron */
```

```
  int nadd;    /* number of nonconform nodes on the tet */
               /* a non conform node is introduced */
               /* by subdividing an adjacent tet */
               /* a nonconform node becomes conform */
               /* when the current tet is subdivided */
  LNodes **xadd;
               /* temporary storage space for the nadd new */
               /* nodes created by splitting adjacent tets */
  double errortet;
               /* tetrahedron's error (error estimation) */
  struct ltets *LLink;
  struct ltets *RLink;
  EData ED;    /* element data, see above */
} LTets;

LTets *HEADTET,*TAILTET;
/* TAILTET is the first tet of the list */
/* HEADTET is the last */


/*-------------------------------------------------------*/
```

Appendix B Longest edge propagation path function

```
void LongestEdgePath()
{
  while(FIRSTTET->sub!=0)
    /* while the initial tet is not subdivided do:*/
    {
      while (LC->sub==0) Conform();
        /* constructs the longest edge propagation path */
        /* LC points to the ListConform data structure */
        /* stops at one of the ending tetrahedron*/
        /* the end is denoted by LC->sub==1 */

      SplitTetrahedron();
        /* split the last tet in the LC list */

        /* go down one tet in the LC (ListConform) list */
      if (LC->LLink!=NULL)
        {
          MC=LC->LLink;
          free(LC);
          LC=MC;
          LC->RLink=NULL;
        }
    }
}
```

Bibliography

[1] N. Amenta and M. Bern. Surface reconstruction by voronoi filtering. *Discrete and computational geometry*, 22(4):481–504, 1999.

[2] N. Amenta, M. Bern, and D. Eppstein. The crust and the beta-skeleton: Combinatorial curve reconstruction. *Graphical models and image processing*, 60(2):125–135, 1998.

[3] J.F. Archard. Contact and rubbing of flat surfaces. *Journal of Applied Physics*, 24(1):18–28, 1953.

[4] R. J. Asaro and J. R. Rice. Strain localization in ductile single crystals. *Journal of the Mechanics and Physics of Solids*, 25:309–338, 1977.

[5] M. E. Backman. Damage mechanics and terminal ballistics research. Technical report, US Naval Weapons Center, China Lake, California, 1969.

[6] M. E. Backman and S.A. Finnegan. The propagation of adiabatic shear. *Metallurgical Effects of High Strain Rates*, 16:531–543, 1973.

[7] M. E. Backman and W. Goldsmith. The mechanics of penetration of projectiles into targets. *International Journal of Engineering Science*, 16:1–99, 1978.

[8] J. M. Ball and J. E. Marsden. Quasiconvexity at the boundary, positivity of the second variation and elastic stability. *Archive for Rational Mechanics and Analysis*, 86:251–277, 1984.

[9] T. Belytschko. An overview of semidiscretization and time integration procedures. In T. Belytschko and T. J. R. Hughes, editors, *Computational Methods for Transient Analysis*, pages 1–65. North-Holland, 1983.

[10] T. Belytschko and M. Tabbara. H-adaptive finite element methods for dynamic problems, with emphasis on localization. *International Journal for Numerical Methods in Engineering*, 36:4245–4265, 1993.

[11] S.J. Brown. Energy release protection for pressurized systems, part 2. *Applied Mechanics Reviews*, 39:177–201, 1986.

[12] J.H. Brunton, J.E. Field, G.P. Thomas, and M.P.W. Wilson. The deformation of metals by high velocity impact. *Metals For The Space Age, Plansee Proceedings 1964*, pages 137–148, 1965.

[13] G. T. Camacho. *Computational Modelling of Impact Damage and Penetration of Brittle and Ductile Solids.* PhD thesis, Brown University, Providence, Rhode Island, May 1996.

[14] G. T. Camacho and M. Ortiz. Computational modelling of impact damage in brittle materials. *International Journal of Solids and Structures*, 33 (20-22):2899–2938, 1996.

[15] G. T. Camacho and M. Ortiz. Adaptive lagrangian modelling of ballistic penetration of metallic targets. *Computer Methods in Applied Mechanics and Engineering*, 142:269–301, 1997.

[16] J. C. Cavendish, D. A. Field, and W. H. Frey. An approach to automatic three-dimensional finite element mesh generation. *International Journal for Numerical Methods in Engineering*, 21:329–347, 1985.

[17] C. T. Chan and K. Anastasiou. An automatic tetrahedral mesh generation scheme by the advancing-front method. *Communications in Applied Numerical Methods*, 13:33–46, 1997.

[18] K. Cho, S. Lee, S.R. Nutt, and J. Duffy. Adiabatic shear band formation during dynamic torsional deformation of an hy-100 steel. *Acta Metallurgica et Materialia*, 41:923–932, 1993.

[19] P. G. Ciarlet. *Numerical analysis of the finite element method.* Les Presses de L'Universite de Montreal, Quebec, Canada, 1976.

[20] L.S. Costin, E.E. Crisman, R.H. Hawley, and J. Duffy. On the localization of plastic flow in mild steel tubes under dynamic torsional loading. *Proc. 2nd Conference on the Mechanical Poperties of Materials at High Rates of Strain*, pages 90–100, 1979.

[21] A. W. Craig, M. Ainsworth, J. Z. Zhu, and O. C. Zienkiewicz. *h* and *h-p* version error estimation and adaptive procedures from theory to practice. *Engineering with Computers*, 5:221–234, 1989.

[22] J. V. Craig and T. A. Stock. Microstructural damage adjacent to bullet holes in 70-30 brass. *J. Aust. Inst. Metals*, 15:1–5, 1970.

[23] A. M. Cuitiño and M. Ortiz. Computational modelling of single crystals. *Modelling and Simulation in Materials Science and Engineering*, 1:255–263, 1992.

[24] A. M. Cuitiño and M. Ortiz. A material-independent method for extending stress update algorithms from small-strain plasticity to finite plasticity with multiplicative kinematics. *Engineering Computations*, 9:437–451, 1992.

[25] P. Devloo, J. T. Oden, and T. Strouboulis. Implementation of an adaptive refinement technique for the supg algorithm. *Computer Methods in Applied Mechanics and Engineering*, 61(3):339–358, 1987.

[26] A. R. Diaz, N. Kikuchi, and J. E. Taylor. A method of grid optimization for finite element methods. *Computer Methods in Applied Mechanics and Engineering*, 41(1):29–45, 1983.

[27] R. Dormeval. The adiabatic shear phenomenon. *Materials at High Strain Rates*, pages 47–70, 1987.

[28] R.J. Eichelberger and J.W. Gehring. Effects of meteorid impacts on space vehicles. *ARS J.*, pages 1583–1591, 1962.

[29] S. Farestam and R. B. Simpson. A framework for advancing front techniques of finite element mesh generation. *BIT*, 35:210–232, 1995.

[30] J.E. Field and I.M. Hutchings. Impact erosion processes. *Inst. Phys. Conf. Ser.*, 70:349–371, 1984.

[31] M. J. Forrestal and V. K. Luk. Dynamic spherical cavity-expansion in a compressible elastic-plastic solid. *Journal of Applied Mechanics*, 55:275–279, 1988.

[32] C. Fressengeas and A. Molinari. Instability and localization of plastic-flow in shear at high strain rates. *Journal of the Mechanics and Physics of Solids*, 35(2):185–211, 1987.

[33] G. Friesecke and G. Dolzmann. Implicit time discretization and global existence for quasi-linear evolution equation with nonconvex energy. *SIAM Journal on Mathematical Analysis*, 28(2):363–380, 1997.

[34] G. Gioia and M. Ortiz. The morphology and folding patterns of buckling-driven thin-film blisters. *Journal of the Mechanics and Physics of Solids*, 42:531–559, 1994.

[35] J.H. Giovanola. Adiabatic shear loading under pure shear loading, parts 1 and 2. *Mechanics of Materials*, 7:59–87, 1988.

[36] U. Grigull and H. Sandner. *Heat conduction.* Springer-Verlag, Berlin, 1984.

[37] P.R. Guduru, G. Ravichandran, and A.J. Rosakis. Observations of transient high temperature vortical microstructures in solids during adiabatic shear banding. *Nature, submitted*, 2000.

[38] K. A. Hartley, J. Duffy, and R. H. Hawley. *Temperature profile measurement during shear band formation in steels at high strain rates.* PhD thesis, Brown University, 1986.

[39] K. A. Hartley, J. Duffy, and R. H. Hawley. Measurement of the temperature profile during shear band formation in steels deforming at high strain rates. *Journal of the Mechanics and Physics of Solids*, 35:283–301, 1987.

[40] K. S. Havner. On the mechanics of crystalline solids. *Journal of the Mechanics and Physics of Solids*, 21:383–400, 1973.

[41] R. Hill and J. R. Rice. Constitutive analysis of elastic-plastic crystals at arbitary strains. *Journal of the Mechanics and Physics of Solids*, 20:401–413, 1972.

[42] W. Hirst and J.K. Lancaster. The influence of speed on metallic wear. *Proc.Roy.Soc. A*, 259:228–241, 1960.

[43] J. Hodowany, G. Ravichandran, A.J. Rosakis, and P. Rosakis. Partition of plastic work into heat and stored energy in metals. *Experimental Mechanics*, 40:113–123, 2000.

[44] K.G. Hoge and A.K. Mukherjee. The temperature and strain rate dependence of the flow stress of tantalum. *Journal of Materials Science*, 12:1666–1672, 1977.

[45] H. Hoppe. Efficient implementation of progressive meshes. *Computer and Graphics*, 22(1):27–36, 1998.

[46] X.L. Huang. *Deformed shear bands and ductile fracture.* PhD thesis, Institute of Mechanics, Beijing, 1987.

[47] T. J. R. Hughes. Analysis of transient algorithms with particular reference to stability behavior. In T. Belytschko and T. J. R. Hughes, editors, *Computational Methods for Transient Analysis*, pages 67–155. North-Holland, 1983.

[48] T. J. R. Hughes. *The finite element method : linear static and dynamic finite element analysis.* Prentice-Hall, Englewood Cliffs, N.J., 1987.

[49] I.M. Hutchings, R.E. Winter, and J.E. Field. Solid particle erosion of metals: the removal of surface material by spherical projectiles. *Proc. R. Soc. Lond. A.*, 348:379–392, 1976.

[50] J.C. Jaeger. Moving sources of heat and temperature of sliding contacts. *Proc.Roy.Soc.*, 56:378–393, 1942.

[51] G. R. Johnson, J.M. Hoegfeldt, U.S. Lindholm, and A. Naguy. Response of various metals to large torsional strains over a large range of strains rates, parts 1 and 2. *Journal of Engineering Materials and Technology*, 105:42–53, 1983.

[52] W. Johnson, A.K. Sengupta, and S.K. Ghosh. High velocity oblique impact and ricochet mainly of long rod projectiles: an overview. *International Journal of Mechanical Sciences*, 24:425–436, 1981.

[53] R. Jordan, D. Kinderlehrer, and F. Otto. The variational formulation of the fokker-planck equation. *SIAM journal on mathematical analysis*, 29:1–17, 1998.

[54] C. Kane, E. A. Repetto, M. Ortiz, and J. E. Marsden. Finite element analysis of nonsmooth contact. *Computer Methods in Applied Mechanics and Engineering*, 180:1–26, 1999.

[55] L. Kobbelt and P. Schroder. A multiresolution framework for variational subdivision. Technical Report CS-TR-97-05, Computer Graphics Research Group, Computer Science Department, California Institute of Technology, 1997.

[56] J.K. Lancaster. The formation of surface films at the transition between mild and severe metallic wear. *Proc.Roy.Soc. A*, 273:466–483, 1963.

[57] A. Lee, W. Sweldens, P. Schroder, L. Cowsar, and D. Dobkin. Maps: Multiresolution adaptive parameterization of surfaces. In *Proceedings of SIGGRAPH 98*, pages 95–104, 1998.

[58] E. H. Lee. Elastic-plastic deformation at finite strains. *Journal of Applied Mechanics*, 36:1–21, 1969.

[59] N. S. Lee and K. J. Bathe. Error indicators and adaptive remeshing in large deformation finite element analysis. *Finite Elements in Analysis and Design*, 16:99–139, 1993.

[60] P.W. Leech. Observations of adiabatic shear band formation in 7039 aluminum-alloy. *Metallurgical Transactions A*, 10:1900–1903, 1985.

[61] J. Lemonds and A. Needleman. Finite element analysis of shear localization in rate and temperature dependent solids. *Mechanics of Materials*, 5:339–361, 1986.

[62] Y.M. Leroy and A. Molinari. Spatial patterns and size effects in shear zones - a hyperelastic model with higher-order gradients. *Journal of the Mechanics and Physics of Solids*, 41(4):631–663, 1993.

[63] J. Lubliner. On the thermodynamic foundations of non-linear solid mechanics. *International Journal of Non-Linear Mechanics*, 7:237–254, 1972.

[64] J. Lubliner. On the structure of the rate equations of materials with internal variables. *Acta Mechanica*, 17:109–119, 1973.

[65] L.S. Magness Jr. High strain rate deformation behaviors of kinetic energy penetrator materials during ballistic impact. *Mechanics of Materials*, 17:147–154, 1994.

[66] J. Mandel. Plasticité classique et viscoplasticité. Technical report, Lecture Notes, Int. Centre for Mech. Sci., Udine, Berlin:Springer, 1972.

[67] A. Marchand and J. Duffy. An experimental study of the formation process of adiabatic shear bands in a structural steel. *Journal of the Mechanics and Physics of Solids*, 36:261–283, 1988.

[68] J. E. Marsden and T. J. R. Hughes. *Mathematical foundations of elasticity.* Prentice-Hall, Englewood Cliffs, N.J., 1983.

[69] T. D. Marusich and M. Ortiz. Modelling and simulation of high-speed machining. *International Journal for Numerical Methods in Engineering*, 38:3675–3694, 1995.

[70] J. J. Mason, A. J. Rosakis, and G. Ravichandran. On the strain and strain-rate dependence of plastic work converted to heat-an experimental study using high-speed infrared detectors and the kolsky bar. *Mechanics of Materials*, 17:135–145, 1994.

[71] A. Molinari and R.J. Clifton. Analytical characterization of shear localization in thermoviscoplastic solids. *Journal of Applied Mechanics*, 54:806–812, 1987.

[72] A. Molinari and Y.M. Leroy. Structures in shear zones due to thermal effects. *Comptes rendus de l'academie des sciences, Serie II*, 313(1):7–13, 1991.

[73] A. Needleman. Dynamic shear band development in plane strain. *Journal of Applied Mechanics*, 56:1–9, 1989.

[74] S. Nemat-Nasser and J.B. Isaacs. High strain-rate, high-temperature response of tantalum and tantalum alloys. In *The Minerals Metals and Materials Society*, volume Proceedings of the 125th TMS Annual Meeting and Exhibition: Tantalum, pages 135–138, 1996.

[75] V.F. Nesterenko, M.A. Meyers, J.C. LaSalvia, M.P. Bondar, Y.J. Chen, and Y.L. Lukyanov. Shear localization and recrystallization in high-strain, high-strain-rate deformation of tantalum. *Materials Science and Engineering*, A229:23–41, 1997.

[76] M. Ortiz and J. J. Quigley. Adaptive mesh refinement in strain localization problems. *Computer Methods in Applied Mechanics and Engineering*, 90:781–804, 1991.

[77] M. Ortiz, R.A. Radovitzky, and E.A. Repetto. The computation of the exponential and logarithmic mappings and their first and second linearizations. *International Journal for Numerical Methods in Engineering*, 2000. submitted.

[78] M. Ortiz and E. A. Repetto. Nonconvex energy minimization and dislocation structures in ductile single crystals. *Journal of the Mechanics and Physics of Solids*, 47:397–462, 1998.

[79] M. Ortiz and L. Stainier. The variational formulation of viscoplastic constitutive updates. *Computer Methods in Applied Mechanics and Engineering*, 171(3-4):419–444, 1999.

[80] K. C. Park and C. A. Felippa. Partitioned analysis of coupled systems. In T. Belytschko and T. J. R. Hughes, editors, *Computational Methods for Transient Analysis*, pages 157–219. North-Holland, 1983.

[81] R. Radovitzky and M. Ortiz. Lagrangian finite element analysis of newtonian fluid flows. *International Journal for Numerical Methods in Engineering*, 43:607–619, 1998.

[82] R. Radovitzky and M. Ortiz. Error estimation and adaptive meshing in strongly nonlinear dynamic problems. *Computer Methods in Applied Mechanics and Engineering*, 172:203–240, 1999.

[83] R. Radovitzky and M. Ortiz. Tetrahedral mesh generation based on node insertion in crystal lattice arrangements and advancing-front-Delaunay triangulation. *Computer Methods in Applied Mechanics and Engineering*, 187:543–569, 2000.

[84] R. Rannacher and F.T. Suttmeier. An adaptive finite element method for problems in perfect plasticity. *Zeitschrift fur angewandte mathematik und mechanik*, 79:143–146, 1999.

[85] R. Rannacher and F.T. Suttmeier. A posteriori error estimation and mesh adaptation for finite element models in elasto-plasticity. *Computer methods in applied mechanics and engineering*, 176:333–361, 1999.

[86] J. R. Rice. Mathematical analysis in the mechanics of fracture. In H. Liebowitz, editor, *Fracture*, pages 191–311. Academic Press, 1968.

[87] J. R. Rice. Inelastic constitutive relations for solids: an internal-variable theory and its applications to metal plasticity. *Journal of the Mechanics and Physics of Solids*, 19:433–455, 1971.

[88] J. R. Rice. Continuum mechanics and thermodynamics of plasticity in relation to microscale deformation mechanisms. In A.S. Argon, editor, *Constitutive Equations in Plasticity*, pages 23–79, Cambridge, Mass, 1975. MIT Press.

[89] M.C. Rivara. New mathematical tools and techniques for the refinement and/or improvement of unstructured triangulations. In *Proceedings of the 5th. international meshing roundtable*, pages 77–86, Pittsburgh, Pennsylvania, 1996. Sandia National Laboratories.

[90] M.C. Rivara. New longest-edge algorithms for the refinement and/or improvement of unstructured triangulations. *International Journal For Numerical Methods in Engineering*, 40:3313–3324, 1997.

[91] M.C. Rivara and C. Levin. A three-dimensional refinement algorithm suitable for adaptive and multi-grid techniques. *Communications in applied numerical methods*, 8:281–290, 1992.

[92] H. C. Rogers. Adiabatic plastic deformation. *Annual Review of Materials Science*, 9:283–311, 1979.

[93] I.V. Roisman, K. Weber, A.L. Yarin, V. Hohler, and M.B. Rubin. Oblique penetration of a rigid projectile into a thick elastic-plastic target: theory and experiment. *International Journal of Impact Engineering*, 22:707–726, 1999.

[94] P. Rosakis, A.J. Rosakis, G. Ravichandran, and J. Hodowany. A thermodynamic internal variable model for the partition of plastic work into heat and stored energy in metals. *Journal of the Mechanics and Physics of Solids*, 48(3):581–607, 2000.

[95] D.M.Y. Sommerville. *Analytical Geometry of Three Dimensions*. Cambridge University Press, 1951.

[96] O.G. Staadt and M.H. Gross. Avoiding errors in progressive tetrahedralizations. Technical Report TR-287, Computer Graphics Research Group, Institute of Scientific Computing, Computer Science Department, ETH Zurich, 1998.

[97] T.A.C. Stock and K.R.L. Thompson. Penetration of aluminium alloys by projectiles. *Metallurgical Transactions*, 1:219–224, 1970.

[98] G. I. Taylor and H. Quinney. The plastic distortion of metals. *Philosophical Transactions of the Royal Society of London A*, 230:323–362, 1931.

[99] L. Taylor and D. Flanagan. Pronto 2d: A two-dimensional transient solid dynamics program. Technical Report SAND86-0594, Sandia National Laboratories, Albuquerque, NM, 1987.

[100] L. Taylor and D. Flanagan. Pronto 3d: A three-dimensional transient solid dynamics program. Technical Report SAND87-1912, Sandia National Laboratories, Albuquerque, NM, 1989.

[101] C. Teodosiu. A dynamic theory of dislocations and its applications to the theory of the elastic-plastic continuum. In J. A. Simmons, editor, *Conf. Fundamental Aspects of Dislocation Theory*, volume 2, pages 837–876, Washington, 1969. Natl. Bureau of Standards Special Publication.

[102] S.P. Timothy. The structure of adiabatic shear bands in metals: A critical review. *Acta Metallurgica*, 35:301–306, 1987.

[103] L. Van Hove. Sur le signe de la variation seconde des intégrales multiples à plusieurs fonctions inconnues. *Koninkl. Belg. Acad., Klasse der Wetenschappen, Verhandelingen*, 24(5):68, 1949.

[104] K.S. Vecchio. High-strain, high-strain-rate deformation of tantalum tungsten alloys. *Journal de Physique IV*, C8:301–306, 1994.

[105] R. Verfürth. *A Review of A Posteriori Error Estimation and Adaptive Mesh-Refinement Techniques.* John Wiley & Sons and B. G. Teubner Publishers, New York, NY, 1996.

[106] A. T. Winter. The influence of projectile geometry on adiabatic shear and target failure. *Metallurgical Transactions*, 4:1829–1833, 1973.

[107] Wriggers-P and Miehe-C. Contact constraints within coupled thermomechanical analysis - a finite-element model. *Computer Methods in Applied Mechanics and Engineering*, 113(3-4):301–319, 1994.

[108] T.W. Wright and R.C. Batra. Further results on the initiation and growth of adiabatic shear bands at high-strain rates. *Journal de physique-Paris*, 46:323–330, 1985.

[109] Y.B. Xu, Z.G. Wang, X.L. Huang, D. Xing, and Y.L. Bai. Microstructure of shear localization in low carbon ferrite-pearlite steel. *Materials Science and Engineering*, A114:81–87, 1989.

[110] M. Zhou, A.J. Rosakis, and G. Ravichandran. Dynamically propagating shear bands in impact-loaded prenotched plates .1. experimental investigations of temperature signatures and propagation speed. *Journal of mechanics and physics of solids*, 44(6):981–1006, 1996.

[111] M. Zhou, A.J. Rosakis, and G. Ravichandran. Dynamically propagating shear bands in impact-loaded prenotched plates .2. numerical simulations. *Journal of mechanics and physics of solids*, 44(6):1007–1025, 1996.

[112] O.C. Zienkiewicz and J.Z. Zhu. A simple error estimator and adaptive procedure for practical engineering analysis. *International Journal for Numerical Methods in Engineering*, 24(2):337–357, 1987.

[113] J.A. Zukas. *High-Velocity Impact Dynamics.* Wiley, New York, 1990.